INTRODUCTORY INVESTIGATION OF THE RANQUE-HILSCH VORTEX TUBE AS A PARTICLE SEPARATION DEVICE FOR THE PBMR

Anja Burger

Thesis Supervisor: Mr. RT Dobson

Co - supervisor: Prof. G Thiart

Department of Mechanical and Mechatronic Engineering

University of Stellenbosch

March 2010

INTRODUCTORY INVESTIGATION OF THE RANQUE-HILSCH VORTEX TUBE AS A PARTICLE SEPARATION DEVICE FOR THE PBMR

Anja Burger

Status: Final Thesis

Thesis Supervisor: Mr. RT Dobson

Co - supervisor: Prof. G Thiart

Department of Mechanical and Mechatronic Engineering

University of Stellenbosch

March 2010

SUMMARY

The Pebble Bed Modular Reactor (PBMR) is a Generation IV graphite-moderated helium cooled nuclear reactor which is being developed in South Africa. The PBMR design is based on the German Arbeitsgemeinschaft Versuchreaktor (AVR). The AVR was decommissioned in December 1988 due to operational and safety problems. The PBMR project has put a lot of emphasis on safety and therefore all safety issues relating to the AVR have to be addressed before this technology can be implemented. After the decommissioning of the AVR plant, technicians found radioactive isotopes of cesium $_{55}Cs^{137}$, $_{55}Cs^{134}$, silver $_{44}Ag^{110}$ and strontium $_{38}Sr^{90}$ as well as graphite dust in the primary coolant loop of the reactor. These isotopes as well as the graphite dust have to be removed from the helium coolant stream because it can be potentially harmful to equipment, personnel and the general public. The main objective of this thesis is therefore to investigate a separation method for removing the graphite dust (and with it the radioactive isotopes) from the helium coolant stream and also test this method under different operating conditions and geometrical configurations to determine its dust separation efficacy. The device chosen to investigate is the Ranque-Hilsch vortex tube.

The Ranque-Hilsch vortex tube (RHVT) is a simple device having no moving parts that produces a hot and cold air stream simultaneously at its two ends from a compressed air source. The vortex generated by the vortex generator located at the inlet of the RHVT causes strongly rotating flows similar in speed to that of a gas centrifuge. The gas centrifuge is used for isotope separation. The RHVT, in theory, can therefore be implemented to separate the graphite/silver isotopes from the helium coolant with the added benefit of either cooling or heating the coolant and was thus selected as the separation technique to be tested experimentally.

The dust separation efficiency of the RHVT was tested experimentally using different grades of graphite dust, different fluids, various inlet volumetric flow rates and volume fractions and different RHVT geometries. The experimental results showed that the RHVT has a dust separation efficiency of more than 85 %. A regression analysis was also

done with the experimental data to obtain a correlation between the different operating conditions (such as volumetric flow rate) and the dust separation efficiency that can be used to predict the dust efficiency under different operating and geometric conditions (such as the PBMR environment).

An analytical model is also presented to describe the 'temperature separation' phenomenon in the RHVT, using basic thermo-physical principals to gain a better understanding of how the RHVT works. A CFD analysis was also attempted to supplement the analytical analysis but the solution did not converge and therefore only the preliminary results of the analysis are discussed.

OPSOMMING

Die "Pebble Bed Modular Reactor" (PBMR) is `n vierde generasie grafiet gemodereede en helium verkoelde reaktor wat in Suid-Afrika ontwikkel word. Die PBMR ontwerp is gebaseer op the Duitse Arbeitsgemeinschaft Versuchreaktor (AVR) wat buite werking gestel is in Desember 1988 as gevolg van operasionele en veiligheidsprobleme. Die PBMR projek lê baie klem op veiligheid en daarom moet alle veiligheidskwessies van die AVR eers aangespreek word voor die tegnologie geimplementeer kan word. Nadat die AVR buite werking gestel is, het AVR tegnisie radioaktiewe isotope van cesium $_{55}Cs^{137}$, $_{55}Cs^{134}$, silwer $_{44}Ag^{110}$ en strontium $_{38}Sr^{90}$ asook grafiet stof in die primêre stroomkring van die reaktor gevind. Hierdie isotope sowel as die grafiet stof moet uit die helium verkoelingsmiddel in die primere stroomkring van die reaktor verwyder word aangesien dit dalk skadelik kan wees vir toerusting, personeel en die publiek. Die hoofdoelwit van hierdie tesis is dus om `n skeidingstekniek te ondersoek wat die stof (en dus ook die radioaktiewe isotope) uit die helium verkoelingsmiddel kan verwyder. Hierdie tegniek moet dan getoets word onder verskillende operasionele en geometriese toestande om die skeidingsbenuttingsgraad te bepaal. Die toestel wat gekies is om ondersoek te word is die "Ranque-Hilsch Vortex Tube".

Die "Ranque-Hisch Vortex Tube" (RHVT) is a eenvoudige uitvindsel wat geen bewegende parte bevat nie en wat warm en koue lug gelyktydig produseer vanaf `n saamgepersde lugbron. 'n Baie sterk roteerende vloei word gegenereer in die RHVT wat dieselfde snelhede bereik as die lug in `n gas-sentrifugeerder. Die gas- sentrifugeerder word gebruik as `n isotoopskeidingsapparaat. In teorie kan die RHVT dus ook gebruik word om partikels te skei as gevolg van die sterk roteerende vloei, met die voordeel dat dit ook die lug kan verhit en verkoel. As gevolg van hierde redes is die RHVT gekies as die skeidingstegniek om te ondersoek en dus experimenteel te toets.
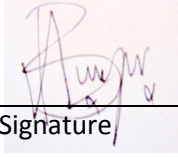
Die benuttingsgraad van die RHVT se vermoë om die grafiet stof van die lug te skei was gevolglik eksperimenteel getoets deur gebruik te maak van verskillende gehaltes grafiet stof, verskillende vloeistowwe (lug of helium), verskillende inlaat volumevloeitempos en volume fraksies en RHVT geometrieë. Die experimentele resultate het getoon dat die

RHVT `n benuttingsgraad van meer as 85 % het. `n Regressie analise was ook gedoen met die eksperimentele data om `n korrelasie tussen die verskillende opersionele toestande (soos volumevloeitempo) en die stof skeiding benuttingsgraad te kry. Hierdie korrelasie kan dan gebruik word om die stofskeidingsbenuttingsgraad onder ander operasionele en geometriese omstandighede, soos die PBMR omgewing, te voorspel.

`n Analitiese model word ook voorgestel om die "temperatuur-skeidings" meganisme in die RHVT te verduidelik, met die hulp van basiese termo-fisiese beginsels, om beter te verstaan hoe dit werk. Daar was ook gepoog om `n CFD analise te doen wat die analitiese model kon aanvul, maar die numeriese oplossing het nie gekonvergeer nie en dus word net die voorlopige resultate van dié analise bespreek.

DECLARATION

I, the undersigned, hereby declare that this report and the work contained therein is my own original work, except where indicated

	15/02/10
Signature	Date

Anja Burger

AKNOWLEDGEMENTS

TABLE OF CONTENTS

LIST OF FIGURES

LIST OF TABLES

NOMENCLATURE

Standard characters

A	Area
a	Constant
a_{air}	Speed of air
b	Constant
C	constant
C_d	Discharge coefficient
c_p	Specific heat constant
d	Diameter
F	Force
f	Friction factor
G	Volumetric flow rate
g	Gravitational acceleration, 9.81 m/s^2
h	Height
ID	Inner diameter
k	Isentropic coefficient
K	Constant
L	Length
l	Width
m	Mass
$\dot{m}$	Mass flow rate
Ma	Mach number
n	Counter
OD	Outer diameter
P	Pressure
ΔP	Pressure difference
$\dot{Q}$	Heat transfer rate
$\mathcal{R}$	Specific gas constant
r	Radius
R	RHVT inner tube diameter

Re	Reynolds number
r_o	Outer cylinder radius
s_{ent}	Entropy
s	Particle position vector
T	Temperature
$\Delta T'_c$	Temperature drop due to adiabatic expansion
t	Time
u	x-direction velocity component
v	Velocity component
V	Velocity
Vol	Volume
$\bar{x}$	Average value
∇^2	Laplacian operator

Greek symbols

α	Adiabatic efficiency
$\propto$	Directly proportional
β	Orifice diameter ratio
η	Dust separation efficiency
θ	Inlet angle
μ	Molecular viscosity
μ_{mc}	Mass fraction
μ_c	Volume fraction
ρ	Density
σ	Standard deviation
τ	Shear stress
φ	Time constant
ω	Vorticity
Ω	Angular velocity

Subscripts/ Superscripts

0	Stagnation conditions
1	First position
2	Second position
*	Critical
A	Sensor A
abs	Absolute
air	
amb	Ambient
atm	Atmosphere
B	
boil	Boiling point
c	Cold
calibration	
clean	Clean air
cond	Conduction
corrected	
ctf	Centrifugal
d	Drag
decrease	
dust	Dust-laden air
eff	Effective
EH	Endress and Hauser sensor
exit	
f	Fluid
gen	Generation
h	Hot
helium	
hist	history
i	Inlet
increase	

large	MS6 flow sensors
loss	Irrecoverable pressure loss
max	Maximum
n	Nozzle
o	Orifice
ofs	Orifice flow sensor
p	Particle
r	Radial direction
reducer	
rel	Relative
RHVT	Centre of RHVT
s	Nozzle slot
small	SFE1 flow sensors
supply	Supply tube
t	Turbulent
tot	Total
uncorrected	
V	Vortex generator
z	Axial direction
θ	Tangential direction
$\rightarrow$	Vector
$-$	Direction vector

1. INTRODUCTION

1.1 Background

Energy is a commodity that all humans are dependent on. Without energy we cannot function and our countries' economies will fall. Our world has a current energy consumption of 512.75 quadrillion kJ as calculated in a survey in the International Energy Annual (U.S Govenment, 2005). This same survey also predicts that the total energy consumption will grow by 50 % by the year 2030. This is cause for alarm because currently 87 % of the energy sources used globally are either natural gas or fossil fuels (such as oil or coal) which are non-renewable energy sources and are rapidly being depleted by the world's ever increasing energy needs. From this data it is evident that alternative energy sources must be exploited.

Nuclear energy is one of a few available alternative energy sources together with renewable energy that can help our world in overcoming the energy crisis. Nuclear energy has the advantage over fossil fuels in that it generates no uncontrollable pollution (such as CO_2 emissions) and that huge amounts of energy can be produced from small amounts of fuel. Nuclear energy is also very reliable but a relatively large portion of the total cost has to be spent on safety, because if an accident does occur it can be disastrous (World Nuclear Assocaition, 2008). An important focus area is therefore reactor safety and many design projects have been launched to design new generation (Generation IV) reactors that are inherently safe (World Nuclear Association, 2009).

One such new generation project is the Pebble Bed Modular Reactor (PBMR) project which is being developed in South Africa. The PBMR is a Generation IV graphite-moderated helium cooled nuclear reactor and its design is based on the German Arbeitsgemeinschaft Versuchreaktor (AVR). The AVR was decommissioned in December 1988 due to operational and safety problems, and therefore PBMR firstly has to address all the safety issues the AVR had to ensure that the reactor is safe for equipment, personnel and the general public before its technology can be used in the PBMR design.

A specific safety issue found by AVR plant technicians, after the AVR was decommissioned, was radioactive isotopes of cesium $_{55}Cs^{137}$, $_{55}Cs^{134}$, silver $_{44}Ag^{110}$ and strontium $_{38}Sr^{90}$ as well as graphite dust deposited in the primary helium coolant loop of the reactor (Bäumer, 1990).

These radioactive isotopes are fission products formed during the nuclear fission process by radioactive decay of precursors and activation of mother products. Since these fission products are radioactive they constitute a potential radioactive contamination hazard for operating personnel and the general public if not contained properly. Usually the fission products are contained within the 150000 special triple coated TRISO particles embedded within a 50 mm spherical graphite matrix in the 60 mm diameter graphite fuel pebbles. The TRISO particles are approximately 0.92 mm in diameter and contain the 0.5 mm diameter uranium dioxide UO_2 fuel kernel that fuels the nuclear reaction. The three coatings of the TRISO particle prevent the fission products from escaping (Gee, 2002). These coatings are pyrolytic carbon, silicon carbide and again pyrolytic carbon as can be seen in Figure 1. A porous carbon buffer layer is also placed around the fuel kernel to maintain its shape as the kernel is deformed by the production of fission products.

Section A-A

60 mm fuel pebble

Individual TRISO particles
0.9 mm diameter

Pyrolytic carbon coating

Silicon carbide barrier

Porous carbon buffer

0.5 mm UO_2 fuel kernel
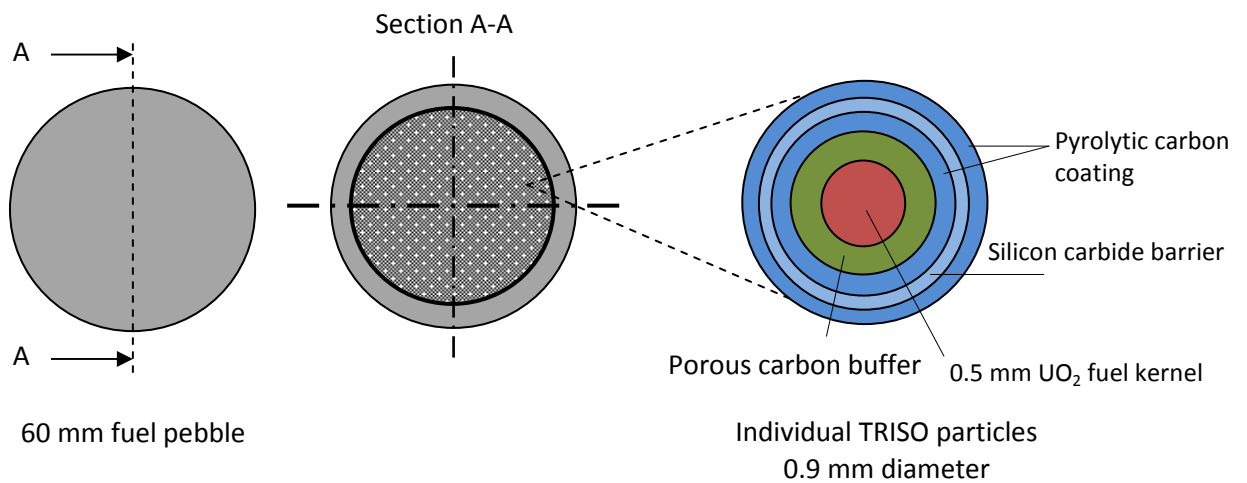
Figure 1: PBMR fuel pebbles construction (not drawn to scale)

Even though the TRISO particles keep most of the fission products intact, the isotopes of cesium $_{55}Cs^{137}$, $_{55}Cs^{134}$, silver $_{44}Ag^{110}$ and strontium $_{38}Sr^{90}$ escape through the silicon carbide and pyrolytic carbon layers and deposit in the primary coolant loop of the

reactor (MacLean and Ballinger, 2004). Of these isotopes silver $_{44}Ag^{110}$ is the isotope of most concern. This is because the fractional release of $_{44}Ag^{110}$ does not depend on the failure fraction of the fuel and has been observed in apparently intact fuel (MacLean and Ballinger, 2004), suggesting that the silver is somehow transported through an intact silicon carbide layer. Silver $_{44}Ag^{110}$ also has a gamma-ray dose rate five times that of the other isotopes and a half-life of 249.9 days which means that if it is deposited in the primary coolant loop it can only be safely removed after 10 half-lives have elapsed which is 2499 days, nearly 7 years (MacLean and Ballinger, 2004). Experimental measurements have shown that the silver release is temperature dependent (Matzner, 2004) although in some cases the release fraction varied from 0 – 100 % which leaves uncertainties about individual particle performance. Since the mode of release of the $_{44}Ag^{110}$ is uncertain this radioactive isotope is of major concern because it cannot be contained and it potentially hinders the accessibility and maintainability of heat exchangers, circulators and inspection chambers in the primary circuit of the reactor.

Another product released from the reactor which is of concern is graphite dust. The dust is formed when the graphite fuel pebbles rub against each other and it was calculated by Bäumer (1990) that approximately 3 kg of dust was produced annually in the AVR. Although the amount of graphite dust produced is minimal, the concern for the dust particles is their ability to be contaminated with fission products and their mobility around the primary coolant loop.

1.2 Objectives

To address the aforementioned AVR safety issue this thesis focused on testing a method to separate and extract the graphite, and by that the silver isotope $_{44}Ag^{110}$ also, from the helium in the primary coolant loop of the PBMR and accumulate (or plate) the particles onto one centrally located surface so that it can be more easily disposed of and does not plate out in the reactor. The device chosen to be investigated for this purpose is the RHVT. The objectives of this thesis therefore are:

- Investigate other separation methods and compare to the RHVT
- Design an experiment to test and measure the RHVT's dust separation capabilities

- → Evaluate the RHVT's graphite dust separation capabilities for different operating and geometrical conditions
- → Do a regression analysis to determine a correlation between the dust separation efficiency and the operating and geometrical conditions to be able to predict the efficiency under different conditions (such as in the PBMR)
- → Do a theoretical analysis on the RHVT to gain a better understanding of how it works

1.3 Overview

The different separation techniques investigated will be discussed in Chapter 2. Both the investigated techniques' advantages and disadvantages are evaluated and compared to the RHVT in section 2.6. The Ranque-Hilsch vortex tube (RHVT) is then discussed in detail in Chapter 3, including the working of the RHVT and a literature study on the experimental and numerical work done on the RHVT up to date.

In Chapter 4 the design of the experimental apparatus used to test the dust separation efficiency of the RHVT is discussed. A schematic drawing of the apparatus is illustrated, and the different components used in the apparatus are discussed. The CAD drawings of the components that were manufactured for a specific application in the apparatus are given in Addendum I. The objective of this thesis is to determine the RHVT's dust separation efficiency under different operating and geometric conditions, and these conditions are determined in section 4.1. The calibration of the different sensors used in the experimental work was calibrated and this process is shown in Appendix B.

The results of the experimental work are given in section 4.4 and the full data set of all experimental data is given in Appendix E.1. A regression analysis was done using the data shown in Appendix E.2 and is also shown in section 4.4.

The theoretical analysis, given in Chapter 5, consisted of an analytical analysis and a numerical (CFD) analysis. The analytical analysis proposed a model as to how the "temperature separation" and the mass separation in the RHVT occur. This model uses the conservation equations and basic thermo-physical principals to macroscopically

model the flow in the RHVT. A numerical model using CFD was attempted to obtain a numerical model which could be compared to the analytical model. The process of performing a CFD simulation consists of different stages and these stages are discussed in Appendix C. The CFD simulation, however, did not converge and therefore only the preliminary numerical results are compared to the analytical model in Appendix C.4.1.

In Chapter 6 the results of this thesis' objectives are discussed and a conclusion is drawn as to whether the RHVT is a viable option to be used in the PBMR. Recommendations for future work are also given.

2. SEPARATION TECHNIQUES

In this section a number of techniques, other than the RHVT, that can be used to separate the graphite dust particles, and thus the radioactive silver isotope $_{44}Ag^{110}$, from the helium coolant in the primary loop of the PBMR reactor will be considered. Most of these separation methods are currently used for uranium isotope enrichment but can also be applied to different isotopes or particles. In the final sub-section of the section the different separation techniques will be evaluated against each other and the RHVT.

2.1 Electromagnetic Isotope Separation

Electromagnetic Isotope Separation (EMIS) is one of the earliest used isotope separation techniques. This method uses large electromagnets to separate the ions of two isotopes. The physical principle employed in this method is that a charged particle will follow a circular trajectory when passing through a uniform magnetic field. Charged particles are generated by bombarding a compound containing the isotopes with electrons and since the two isotopes have different masses they will have different trajectories. The isotopes can thus be collected separately in two different collector "pockets". This principle is graphically illustrated in Figure 2, and can also be used to separate particles with different masses.
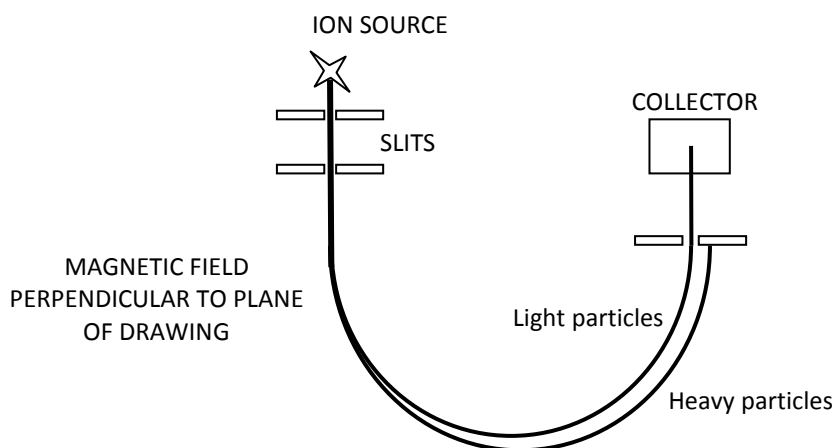
Figure 2: Trajectory of charged particle in static magnetic field (De Wolf Smyth, 1945)

2.2 Laser Isotope Separation

Laser isotope separation (LIS) is an isotope separation process that uses lasers to selectively excite atoms or molecules of the isotope to be extracted. There are two major LIS processes: atomic vapour isotope separation (AVLIS) where the process medium is atomic vapour and molecular laser isotope separation (MLIS) where the process medium is a compound gas.

The AVLIS process consists of a laser system and a separation system. The laser system consists of a dye master oscillator laser that is optically pumped by another laser (Pike, 2005). Dye oscillator lasers produce light at a precise laser frequency that is used to ionize the desired isotope in the separation process. In uranium enrichment a total of three colours are used in the dye laser to ionize the $_{92}U^{235}$ isotope. The ionized $_{92}U^{235}$ atoms are then deflected by an electrostatic or electromagnetic field to a product collector, while the neutral $_{92}U^{238}$ atoms pass through the electrostatic field unaffected and are deposited at a different location. The AVLIS method is illustrated in Figure 3.
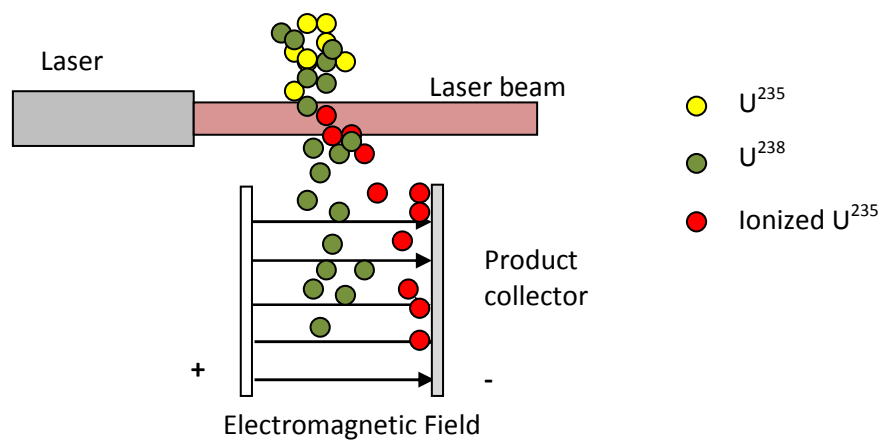
Figure 3: AVLIS process (Hargrove, n.d.)

The MLIS uses a compound gas as its process gas. In uranium enrichment UF_6 (uranium-hexafluoride) gas is mixed with a carrier gas (such as hydrogen or a noble gas) and this mixture is used as the process gas. The MLIS process consists of two basic steps: the first step is to selectively excite the $_{92}U^{235}$ in the UF_6 compounds; in the second step the excited $^{235}UF_6$ is bombarded with photons from an infrared or XeCl ultraviolet laser

system which dissociates the excited $^{235}UF_6$ to form $^{235}UF_5$. The newly formed $^{235}UF_5$ precipitates from the gas as a powder that can be collected by filtration from the process gas stream. Thus the MLIS is a stage-wise process whereby the precipitated $^{235}UF_5$ must be converted back to UF_6 for further enrichment.

2.3 Gas Centrifuge

The gas centrifuge process uses a large number of fast rotating cylinders to separate isotopes or particles (Pike, 2005). The rotation of the rotor of the centrifuge creates a strong centrifugal force that forces the heavier isotopes/particles inside the centrifuge cylinder towards the cylinder wall and leaves the lighter isotopes/particles behind at the centre. In uranium enrichment the centrifuge is supplied with a compound gas of UF_6 that forms a counter-current flow along the rotational axis of the cylinder. This counter-current transforms the radial isotopic flow gradient into an axial flow gradient. The upward flowing stream is thereby gradually enriched by the UF_6 supply while the downward current is depleted. This process is illustrated in Figure 4 for a uranium enrichment application.
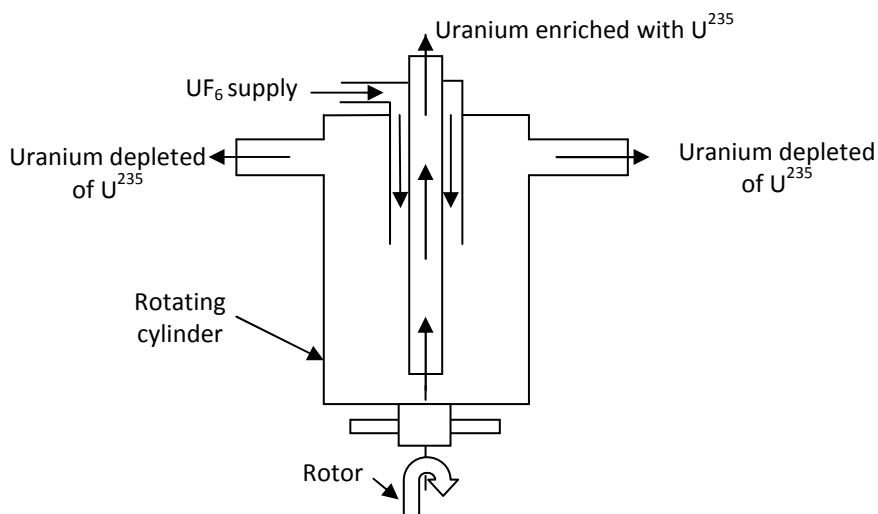
Figure 4: Gas centrifuge (Anon., 2008)

The gas centrifuge's rotational speed determines its separation efficiency and is only limited by the strength-to-weight ratio of the rotor material and the lifetime of the rotor

bearings. At present the most popular rotor material is maraging steel, which allows a maximum rotor wall speed of 500 m/s.

2.4 Centrifugal Dust Collectors

Centrifugal dust collectors use centrifugal force to separate dust particles from dust laden air streams and are mostly used for air filtration in factories, mines and locomotives. The working of a centrifugal dust collector can be explained by examining a typical commercially available Cyclone dust collector (Figure 5a). The dust laden air stream enters the Cyclone at an angle which causes it to spin rapidly and form a vortex. The resulting centrifugal force, due to the generated vortex, pushes the dust particles towards the wall of the Cyclone and after striking the wall the dust particles fall into a hopper located underneath the Cyclone.

The Flosep (NESCA, 2009) which was developed by NECSA and the VORSEP (Figure 5b) are two more examples of commercially available dust collectors. The VORSEP has lower pressure losses and is more resistant to wear than the typical Cyclone and it was therefore decided to investigate it further.
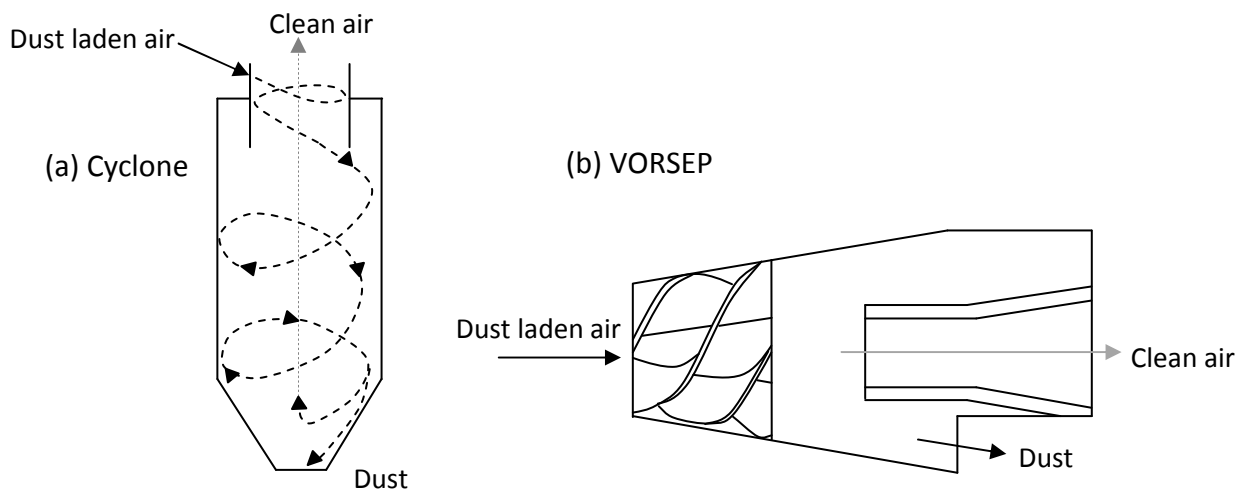
Figure 5: Centrifugal dust collectors

The VORSEP is an axial centrifugal separator which forces the inlet air to rotate (form a vortex) by helical vanes located at the inlet. The centrifugal force generated from the vortex pushes the dust outwards past the centrally located outlet, where it falls out

through a scavenge opening due to its momentum and gravity. Since the primary direction of the air stays unchanged along the axis of the VORSEP the pressure loss is minimized.

2.5 Ranque-Hilsch Vortex Tube

The Ranque-Hilsch vortex tube (RHVT) is a simple device having no moving parts that produces a hot and cold air stream simultaneously at its two ends from a compressed air source (Singh et al., 2004). RHVT's are commercially used for tool-cooling or cryogenic applications. There are generally two main types of RHVT's, the counter-flow (often referred to as the standard) type and the uni-flow type. The basic layout of the counter-flow vortex tube is shown in Figure 6(a) and the uni-flow vortex tube shown in Figure 6(b).
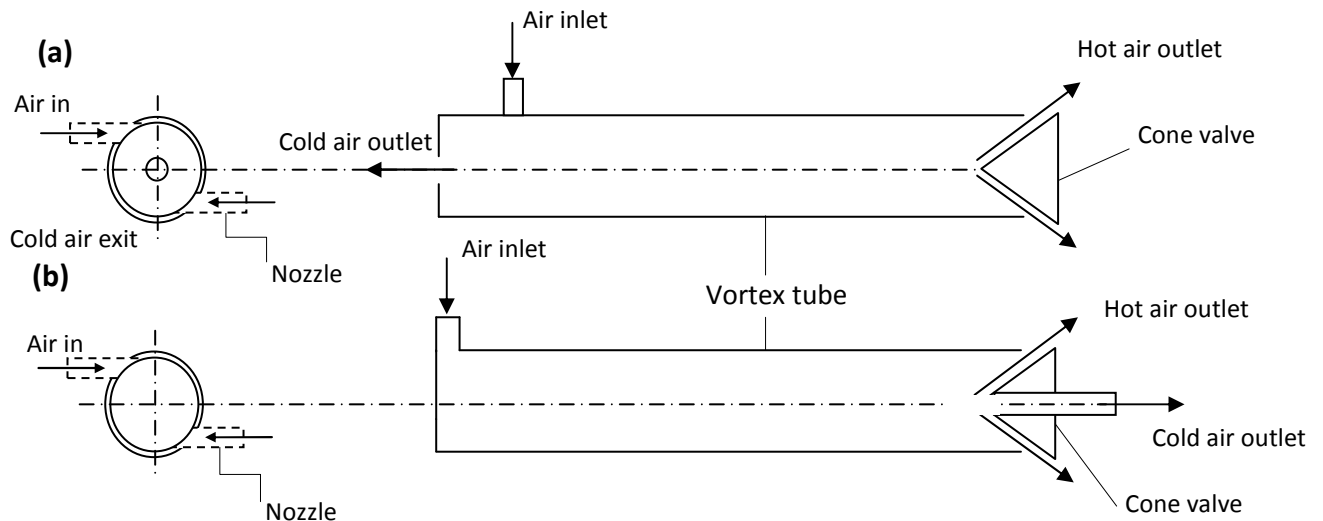
Figure 6: (a) Counter-flow and (b) Uni-flow vortex tube (Promvonge and Eiamsa-ard, 2008)

The counter-flow RHVT consists of air inlet nozzles, a vortex tube, a cold air outlet and a hot air outlet. Compressed air enters the counter-flow RHVT through two tangential nozzles or through a single supply tube and a vortex generator (an aerodynamic surface consisting of a small vane or inlet nozzles that creates a vortex) and develops vortex flow (strongly rotating flow). The air flows through the tube rather than passing through the cold outlet located next to the inlet nozzles, because the orifice is of a much smaller diameter than the vortex tube. The amount of air that escapes at the furthest end of the

tube, called the hot outlet, is controlled by the cone-shaped valve. The remainder of the air returns through the centre of the tube to the cold orifice, called the cold outlet, as a counter-flowing stream, hence the name counter-flow RHVT.

The uni-flow RHVT also consists of an inlet nozzle or nozzles and a vortex tube but instead of having a cold-orifice and cone-shaped valve at opposite ends of the tube, as shown in Figure 6(b), it has a cone-shaped valve with a centrally located cold orifice. The operation of the uni-flow RHVT is similar to the counter-flow RHVT except that the cold outlet is located concentrically with the hot outlet.

2.6 Evaluation of the Considered Separation Techniques

In this section the advantages and disadvantages of the considered separation techniques are discussed to determine which techniques the RHVT has to contend with.

The disadvantage of the EMIS process is that less than half the isotope compound is converted into ions and less than the desired ions are actually separated and collected which makes it very inefficient. Other drawbacks of this process include that it requires intensive labour to remove the unused deposited material for reuse, and its high energy consumption (Pike, 2005). Mainly due to its high energy consumption the EMIS process would not be an effective particle separator in the PBMR, because it would require too much of the reactor's generated energy to function, which would decrease the total reactor output.

The AVLIS process has many advantages such as a high separation factor, low energy consumption and also generates a small volume of waste. The MLIS process has the advantage over the AVLIS process in that it has an even lower energy consumption and its use of UF_6 as a process gas. However, both processes require sophisticated hardware, made from specialized materials, and are therefore very difficult and expensive to implement.

The gas centrifuge is very effective (enrichment factor of 1.3) and is implemented in many countries around the world for the purpose of uranium enrichment for nuclear fuel, but it has a relatively high energy consumption in comparison with other methods such as the AVLIS. Another disadvantage of the gas centrifuge is that it is also used for nuclear proliferation and is therefore not readily commercially available.

The VORSEP shows a very high efficiency of particle separation of 90 % and higher for particles between 1 – 10 μm in diameter (WetAir, 2005). Unfortunately the efficiency drops rapidly to between 0 % and 70 % for particles under 1 μm and since the graphite particles found in the AVR has a nominal diameter of 0.76 μm the VORSEP will not be an effective separation device for use in the PBMR.

The vortex flow within the RHVT is similar to the rotational flow created within the gas centrifuge and centrifugal dust separators and can reach speeds of up to 1,000,000 rpm (104 720 rad/s) according to a RHVT manufacturing company Etest (2008). Although the RHVT is not generally used for particle separation, it can be reasoned that it can be used to separate particles of any size, due to the high rotational flow inside it, and the consequent large centrifugal forces acting upon the particles. An added advantage of the RHVT is the air cooling and heating that occurs due to the temperature separation effect inside the RHVT. This heating and cooling effect can also be implemented elsewhere in the helium loop of the PBMR. The helium coolant leaves the reactor at a pressure of 9 MPa and temperature of 900°C; thereafter it enters the turbines which are connected to the generators. The helium coolant then leaves the turbines at 500°C and 2.6 MPa after which it has to be cooled, recompressed, reheated and returned to the reactor inlet. Since the helium coolant is already compressed in the primary loop, it could be possible to utilize the RHVT air cooling and heating to aid in either heating or cooling the helium before it re-enters the reactor. The RHVT therefore has all the advantages of a gas centrifuge and a centrifugal dust collector but is more readily available, has the potential to separate dust particles with a particle diameter of less than 1 μm and also provides the extra bonus of aiding as a gas cooler or heater. Also since it requires no energy input (except compressed air/helium, which is already available in the coolant loop) and is inexpensive to manufacture, it is more economical

to use than the LIS or EMIS processes. The RHVT will be discussed in more detail in

Chapter 3.

3. RANQUE-HILSCH VORTEX TUBE

The concept of the vortex tube was first conceived by the nineteenth century physicist, James Clerk Maxwell. In 1867 Maxwell imagined that someday we might be able to get hot and cold air from the same device with the help of a "friendly little demon" who would separate the hot and cold air molecules (Cockreill, 1995). This "friendly little demon" became known as Maxwell's demon. The first vortex tube was actually invented by accident by a French metallurgist and physicist, George Ranque in 1928. While experimenting with a vortex pipe he discovered that warm air is exhausted from one side of the tube and cold air from the other (Ranque, 1933). His findings were however received with disbelief and apathy by the scientific community, and since the vortex tube was very thermodynamically inefficient, it was abandoned as a useful source of refrigeration. The first experimental test results of a vortex tube were published by German engineer Rudolph Hilsch in 1945. He reported an account of his own experimental studies aimed at improving the thermodynamic efficiency of the vortex tube (Hilsch, 1947). Hilsch examined the effect of the geometrical parameters of the tube on its performance and also proposed an explanation for the temperature separation. After World War II Hilsch's documents and vortex tubes were found and this was the starting point for further studies and experiments on the vortex tube. In memory of the two founding scientists that discovered and first studied the vortex tube, it is known today as the Ranque-Hilsch vortex tube.

Since the publication of Hilsch's studies, the Ranque-Hilsch vortex tube has been the subject of much interest and many studies have been conducted in an attempt to explain, using physical principles, the mechanism whereby the temperature difference between the two outlet streams, the one hotter and the other colder than the inlet temperature, is indeed achieved. This temperature difference is commonly called "temperature separation". Research studies attempting to explain this physical phenomenon fall into two groups: experimental work and numerical work. The first group focuses on the geometric and thermo-physical parameters of the vortex tube and the second group focuses on qualitative, analytical and numerical analyses. These two groups will be discussed separately in the following two subsections.

3.1 Experimental Studies

Many experimental studies have been done since 1947 attempting to explain the temperature separation mechanism in the RHVT. There are many theories as to how the temperature separation takes place, but no theory has yet been developed to explain the complete phenomenon of the RHVT. Mostly, the geometric parameters and operating conditions of the RHVT leading to the temperature separation effect have been experimentally examined. In this section the temperature separation phenomenon theories based on experimental work will be discussed as well as the experimental work done on using the RHVT as a mass separation device.

3.1.1 Temperature Separation

While there may and indeed are many different theories as to how the temperature separation in the RHVT takes place, only the following three will be considered: i) the viscous-shear theory, ii) the secondary flow theory and iii) the refrigeration cycle theory. Following these theories, further experimental work done on the RHVT with regards to geometric parameters and operating conditions will be discussed.

i) Viscous-Shear Theory

The viscous-shear theory suggests, in essence, that the swirling gas in the RHVT consists of concentric layers which have different angular velocities. The angular velocity of the different gas layers increase towards the centre of the vortex (conservation of angular momentum).The result of this is a shearing effect between these gas layers which leads to energy being transferred from the inner to the outer layers.

A structure for visualizing large-scale structures in an aerodynamic flow was developed by Arbuzov et al. (1997), and by using the Hilbert colour method visualized the swirling flows within the RHVT. Arbuzov et al. concluded that there are four possible mechanisms that could be responsible for the temperature separation in the RHVT: i) Small-scale localized vortices are formed within the large-scale vortex, and these vortices are responsible for the convective heat transfer between the fluid particles. ii) Barothermal effects, heat transfer due to a pressure gradient, iii) Heat exchange between the fluid and the walls of the RHVT and iv) Heating of the fluid due to viscous

dissipation of kinetic energy. They concluded, however, that the most likely mechanism responsible for the temperature separation is the viscous heating of the fluid in a thin boundary layer at the walls of the RHVT and the cooling of the fluid at the centre of the RHVT due to the formation of a vortex braid, which lowers the pressure along the RHVT axis and thus cools the fluid.

This theory was supported by Wu et al. (2006) who also concluded that the temperature separation is due to the energy transfer caused by fluid viscosity at different radii. Lewins and Benjan (1999) suggested that angular velocity gradients in the radial direction of the flow give rise to frictional couplings between different layers which results in shear work between these layers and hence the transfer of energy from the inner to the outer layers. Trofimov (2000) verified that the internal angular momentum of the RHVT leads to the effect suggested by Lewins and Benjan (1999).

ii) Secondary Flow Theory

Another popular theory is that there exists a secondary flow within the RHVT which is responsible for the temperature separation as postulated by Ahlborn and Groves (1997). Ahlborn and Groves used a novel pitot tube to measure the axial and tangential velocities in a vortex tube and found a secondary circulation within the RHVT in the axial direction. They concluded that this secondary circulation has the potential to convect energy from the inner cold air stream to the outer hot air stream. A sketch of the secondary flow pattern can be seen in Figure 7.

Visual and numerical simulations were conducted by Sohn et al. (2002) to investigate the temperature separation in a counter-flow RHVT using surface-tracing methods and found that four secondary flows existed near the cold exit and that these flows induced compression and expansion in the vortex tube similar to that of a refrigeration cycle. Evidence of this secondary circulation was also found by Gao et al. (2005)
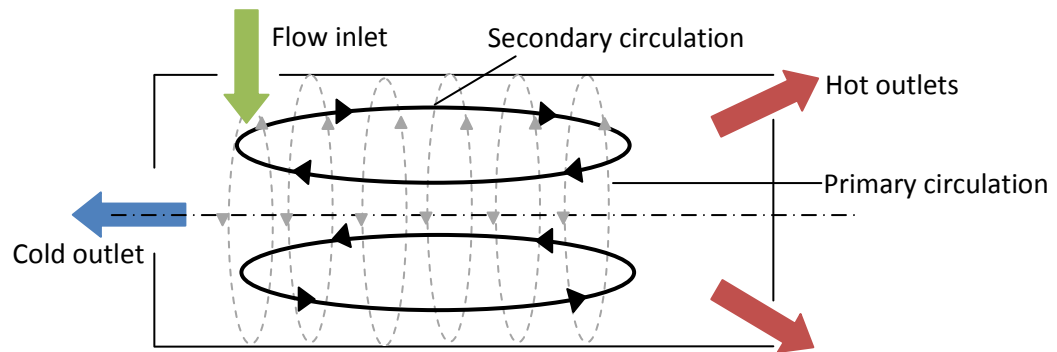
Figure 7: Secondary flow in a RHVT (Ahlborn and Groves, 1997)

iii) Refrigeration Cycle Theory

Another theory postulated by Ahlborn and Gordon (2000) is that the secondary flow in the RHVT acts as a classic refrigeration cycle complete with refrigerant and coolant loops, expansion and compression, heat exchangers and significant temperature splitting (see Figure 8). Referring to Figure 8, the four different branches of the refrigeration loop (that can be compared to the four branches of conventional mechanical coolers) can be explained as follows:

(a) Heat rejection (4 → 1): Near the flow inlet the hotter gas in the secondary circulation rejects heat into the cooler gas in the primary circulation (see Figure 7)

(b) Adiabatic expansion (1 → 2 → 3): The fluid moves from the heat exchange region (1) towards the hot outlet of the RHVT (2) and then turns inwards to the central flow core (3). The pressure at point 2 must therefore be higher than at point 3, and the gas in the secondary loop expands adiabatically.

(c) Energy absorption (3 → c): This is the refrigeration branch of the flow in which the fluid cools by transferring heat from the primary circulation to the secondary circulation.

(d) Adiabatic compression (c → 4): The axial acceleration caused by the primary circulation provides enough mechanical energy to push the secondary circulation radially outwards, where it is recompressed as it moves to point 4.
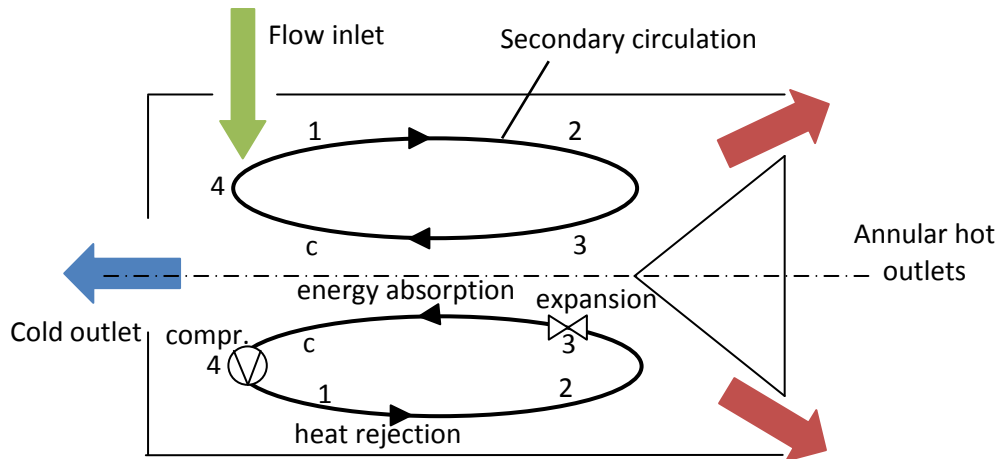
Figure 8: The RHVT as a classic refrigeration cycle: $4 \rightarrow 1$ Heat rejection, $1 \rightarrow 2 \rightarrow 3$ Adiabatic expansion, $3 \rightarrow c$ Energy absorption, $c \rightarrow 4$ Adiabatic compression.

iv) Further experimental studies

As stated, much experimental work has also been done to examine the influence of geometric parameters and operating conditions on the temperature separation effect of the RHVT rather than postulate a theory as to how the temperature separation manifests itself. A few of these studies will now be discussed.

Ting-Quan et al. (2002) tested the performance of the RHVT temperature separation under different operating conditions. It was found that the inlet pressure greatly influences the temperature separation performance while the effect of the inlet temperature was negligible. It was found that with an increased inlet pressure the greater the difference in temperature between the hot and cold outlets. Furthermore the results showed that the optimum temperature separation effect can be achieved by varying the cold volume fraction, defined as $\mu_c = \frac{G_c}{G_i}$, between $70 - 80$ %.

In 2004 Shannak (2004) measured the hot and cold exit temperatures as well as the friction factors within the RHVT experimentally. His results show that the hot outlet air temperature increases with an increase in cold mass fraction $\mu_{mc} = \frac{\dot{m}_c}{\dot{m}_i}$ up to 0.82, and that the cold outlet air stream temperature decreases with a decrease in the cold air mass fraction up to 0.3. For cold air mass fractions greater than 0.82 and less than 0.3

the effects are reversed and the hot air stream tends to decrease in temperature, while the cold air stream increases in temperature.

In 2005 Promvonge and Eiamsa-ard (2005) studied the effect of the number of inlet nozzles and cold outlet diameter on the temperature separation phenomenon. Their results showed that a higher temperature separation was achieved with an increase in the number of inlet nozzles. They also found that a small cold outlet diameter resulted in high back pressures whereas a large cold outlet resulted in lower temperature separation.

Singh et al. (2004) carried out experiments in order to understand the heat transfer characteristics in a RHVT with respect to parameters such as the inlet nozzle area, cold and hot outlet areas and length to diameter ratios. They investigated the effect of these parameters on two different RHVT designs: a maximum temperature drop RHVT and a maximum cooling effect (which was designed for producing large quantities of air at moderate temperatures). The results showed that the cold mass fraction and adiabatic efficiency ($\alpha = \mu_c \frac{\Delta T_c}{\Delta T_c'}$) are more influenced by the size of the cold outlet than the size of the inlet nozzle. Singh also found that the length of the tube has no effect on the performance when it is increased beyond 45 times the diameter of the tube.

3.1.2 Mass Separation

The possibility of using the RHVT as a mass separation device has intrigued many scientists and since the objective of this thesis is to use the RHVT as a particle separator, past experiments in this regard were investigated. Baker and Rathkamp (1954) first investigated the possibility of the RHVT being used as a particle separator, with specific application to isotope separation. They tested the separation of air, oxygen and nitrogen, isotopes of nitrogen and oxygen and a helium and argon mixture and found that the separation factor is so small that the deviance in their data could more likely be contributed to analytical errors rather than to actual separation. Although they did not entirely deny that the RHVT can be used as a mass separator, they claimed that it's highly unlikely on the basis of their findings.

After World War II Linderstrom-Lang (1964) disproved the Baker and Rathkamp (1954) theory when he showed that the RHVT can indeed be used as a gas mixture separation device. He put forth that centrifugation was the primary reason for gas separation in the vortex tube. He conducted experiments using oxygen and nitrogen (air), oxygen and carbon dioxide, and oxygen and helium. It was found that the RHVT, acting like a centrifuge, transports the heavier particles to the outside of the tube making it possible to separate the heavier and the lighter gas particles.

Marshall (1977) also used several different gas mixtures in a variety of vortex tubes and confirmed that gas separation does take place as reported by Linderstrom-Lang (1964).

Kap-Jong et al. (2004) studied the dust separation characteristics of a counter-flow vortex tube using lime (CaO) powders with mean particle diameters of 5 µm and 14 µm. Using a small RHVT of inner diameter 16 mm they found that more than 90 % of the lime powder was separated from the air stream when the cold volume fraction of the air was 0.9. They also investigated the effects of varying cold volume fraction, inlet pressure and velocity and particle size on the separation efficiency, $\eta = \frac{m_{dust}}{m_{dust} + m_{clean}}$. They found that the volume mass fraction did not change the separation efficiency significantly until the volume fraction reached 0.5, and then the decrease in efficiency was only about 5 % at the most. Their results also showed that with an increase in inlet pressure and inlet velocity the separation efficiency decreased for the larger particle powder but increased for the smaller particle powder. Therefore to obtain an efficient performance in dust separation for both particle sizes, they found that a separation efficiency of 93 % can be obtained with an inlet velocity of 14.52 m/s.

Kulkarni and Sardesai (2002) did experiments to separate methane and nitrogen gasses using a vortex tube to enrich methane for mining industry applications. Their data showed that gas separation did occur, but only in small quantities which had to be measured with a gas chromatograph. They also determined that the gas separation is dependent on two parameters, the inlet pressure and the cold mass fraction. They

found that the degree of dust separation has a linear dependence on the inlet pressure; the higher the inlet pressure the higher the dust separation capability of the RHVT.

3.2 Analytical and Numerical Studies

In this section the analytical and numerical studies done on the RHVT are reported and will be discussed separately. The analytical and numerical studies that have been done on the RHVT up to date are only on the temperature separation mechanism in the RHVT and therefore only this mechanism will be discussed in this section

3.2.1 Analytical Studies

Following Hilsch's initial analytical model, Kassner and Knoernschild (1948) applied their "laws of shear stress in circular flows" theory. Their law states that the shear stress is a function of the shear velocity

$$\tau = \mu \left(\frac{du}{r} - \frac{u}{r} \right)$$

1

where τ is shear stress, μ is the fluid viscosity and $\left(\frac{du}{r} - \frac{u}{r} \right)$ is the "shear velocity" as defined in the text. They hypothesized that the initial flow in the RHVT is a free vortex due to the law of constant angular momentum (Ωr^2 = constant). A free vortex occurs when the velocity varies inversely as the distance from the centre of the tube increases so that the angular momentum stays constant. This free vortex leads to a pressure distribution which causes an adiabatic expansion leading to a low temperature in the region of lower pressure, which is at the centre of the vortex. Due to shear stresses, the flow down the tube, towards the hot exit valve, changes from a free to a forced vortex. The difference between a free and forced vortex are described using Figure 9. In Figure 9 it can be seen that within a forced vortex the tangential velocity v_θ is directly proportional to the radial location r, and in free vortex the tangential velocity is inversely proportional to the square of the radial location.

This change in flow from a free to a forced vortex causes kinetic energy to flow radially outward. This forms a radial pressure gradient which in turn causes a temperature gradient. The kinetic energy is transported along this temperature gradient which leads

to even lower temperatures at the centre of the RHVT. According to Reynolds (1961) this is the most widely favoured explanation of the RHVT temperature separation effect.
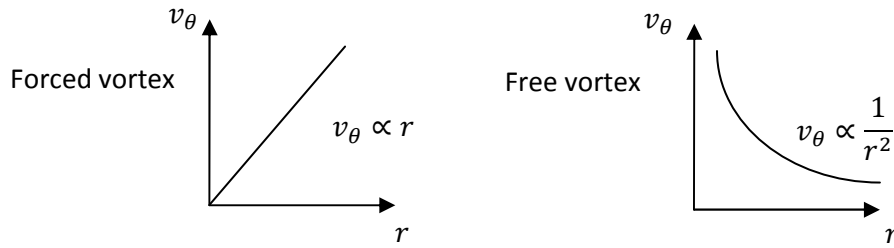
Figure 9: Forced and free vortices

Kap-Jong et al. (2004) proposed a similar model. Their model predicts that the vortex flows are generated as illustrated in Figure 10.
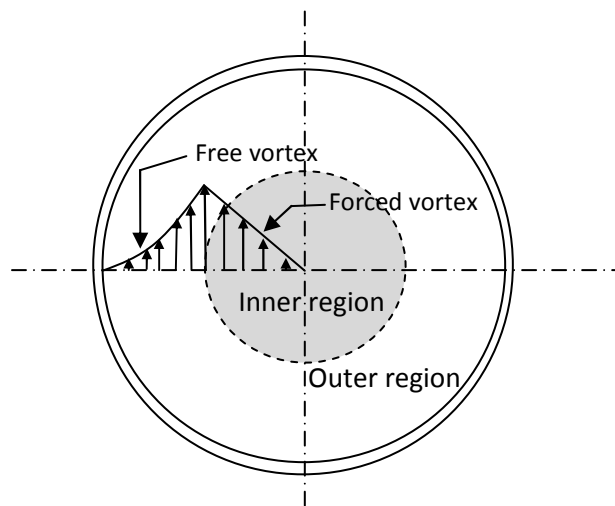
Figure 10: Cross-section of vortex tube showing free and forced vortex flows (Kap-Jong et al., 2004)

Due to the friction between the gas and the inner surface of the vortex tube, the angular velocity is lower in the outer flow region than in the inner flow region, which leads to the formation of the free vortex in the outer flow region. As the flow moves to the hot outlet it is throttled by the cone valve (as illustrated in Figure 5a) and changes to a forced vortex in the central core.

Deissler and Perlmutter (1960) considered an axisymmetrical model in which they divided the vortex into a core and an annular region, each with different but uniform

axial mass velocities. They concluded from their analytical studies that the turbulent energy transfer to a fluid element is the most important factor affecting the element's total temperature. This prediction was in close agreement to the experimental results of Hilsch (1947).

Linderstrom-Lang (1971) examined analytically the thermal and velocity fields in the RHVT. Using the momentum equation developed by Lewellen (1962) he calculated the axial and radial gradients of the tangential velocity profile. These results correlated qualitatively with his experimental measurements.

Stephan, et al. (1984) derived a mathematical model for the temperature separation process but could not solve the equation because the system of equations was too complex. These equations, however, did lead to a similarity relation for the prediction of the cold gas temperature that agreed with their dimensional analysis results.

3.2.2 Numerical Studies

Many numerical studies have been done on the RHVT but few have given results regarding the temperature separation mechanism. During the investigation it was also found that almost none of the findings are in agreement with each other, unlike the analytical and experimental studies in which there was some agreement. Those numerical studies that were in agreement with other experimental or analytical studies and that postulated a theory as to how the temperature separation mechanism works are now discussed.

Numerical studies were conducted by Behera et al. (2008) who developed a three-dimensional numerical model of the RHVT using Computational Fluid Dynamics (CFD), together with the Renormalization Group (RNG) turbulence model to analyse flow parameters and the temperature separation mechanism. The flow parameters (velocity, temperature and pressure) were determined by tracking different particles moving through the flow from the inlet to the hot and cold outlets. By investigating the flow field and taking fluid property variation into account they found that the angular velocity decreases radially outwards. They proposed that this velocity gradient leads to the

transfer of work from the fast moving inner layers to the slower moving outer layers. This theory also supports Hilsch's original temperature separation theory from 1947 as well as the "viscous shear theory" discussed in section 3.1.1 (i).

Eiamsa-ard and Promvonge (2007) applied a numerical mathematical model for the simulation of the temperature separation. Their work was carried out in order to better understand the physical behaviours of the flow, pressure and temperature in a RHVT. A staggered finite volume approach with both the standard k-ε and the Algebraic Stress Model (ASM) was used to perform all computations. They compared their numerical results to the experimental data of Eckert and Hartnett (1957) and found that both turbulence models are in good agreement with the experimental measurements but the ASM provides better agreement between the numerical and the experimental results. In regards to the temperature separation, their computations showed that mean kinetic energy diffusion is the main influence on the cooling of the air in the centre of the RHVT while expansion effects (pressure work) and stress generation are responsible for the heating of the air near the wall of the RHVT.

Oliver (2008) also employed CFD to predict the primary and secondary flows in a RHVT, by using the k-ε model, SST model and Reynolds stress model. Using these models he could confirm the presence of a secondary flow, although he claims it is superfluous to the source of temperature separation as claimed by Ahlborn and Groves (1997). In addition, he also captured other flow-field characteristics which could not be calculated analytically, namely the tangential and axial velocity distribution at the entrance region. These calculated flow-field characteristics showed that recirculation occurs at the entrance region and Oliver claims that this is how the temperature of the air is reduced. By calculating the rotary work due to friction he also concluded that friction is the main source of heating the air.

As can be seen by this literature study on the experimental, analytical and numerical work, there are many theories as to how the temperature separation in the RHVT works. Although there are some theories that are in agreement, it is clear that there are too many different theories to discern a complete model of the exact working of the RHVT,

which is why it was decided to analytically model the RHVT in section 5 of this thesis and try to postulate a simple model which explains the temperature separation in its entirety.

From the experimental literature it is also shown that the RHVT has previously been used for particle separation as in the case of Kap-Jong et al. 2004. Their results showed a very good particle separation efficiency for the RHVT of 90 %, which validates the assumption that the RHVT can be used as a particle separator.

4. EXPERIMENTAL WORK

The purpose of the experimental work is to measure the graphite dust/silver $_{44}Ag^{110}$ isotope separation capabilities of a RHVT and therefore to determine its effectiveness as a mass separation device. Given that the use of radioactive $_{44}Ag^{110}$ in a normal laboratory environment is impractical, it was decided to test the separation efficiency of the RHVT with graphite dust only. Since the silver $_{44}Ag^{110}$ attaches to the graphite dust and the graphite dust is actually the cause for the silver $_{44}Ag^{110}$ transportation through the primary loop of the PBMR reactor (Bäumer, 1990), it is reasonable to assume that the measurement of the RHVT's ability to separate graphite dust would be a good indication of its ability to separate the silver $_{44}Ag^{110}$ isotope as well.

Other than determining the dust separation efficiency of the RHVT, the influence of other external variables on its mass separation capabilities also have to be investigated. According to Kap-Jong et al. (2004) the dimensions of the RHVT, such as tube length, cold volume fraction μ_c, inlet pressure and dust particle size have a considerable influence on the mass separation efficiency. The influence of these parameters was also reported by Yilmaz et al. (2009) as well as the importance of the inlet flow rate. Kulkarni and Sardesai (2002) also reported the strong influence of the inlet pressure of the mass separation efficiency. Another parameter that can have a significant influence on the dust separation efficiency is the working fluid (air or helium). The commercially available RHVTs used in this experiment (two RHVTs from the manufacturer Exair® were used in the experimental work: a small and a medium sized RHVT, see section 4.1.2) are generally used in air whereas the primary coolant in the PBMR is helium. The effect of both these fluids on the dust separation efficiency will therefore have to be tested. Based on the above mentioned literature and the specified coolant used in the PBMR, the effect of the following variables on the dust separation efficiency η was determined and quantified in the experimental work. These variables are volumetric flow rate G, cold volume fraction μ_c (see Appendix D), working fluid, dust particle size and geometry of the RHVT.

4.1 Experiment Design

To test the mass separation capabilities of the RHVT as well as determine the influence of the variables discussed in the previous paragraph on the RHVT dust separation efficiency, an experimental test apparatus was designed which had to be able to do the following:

- ⤳ Inject graphite dust upstream of the RHVT
- ⤳ Measure the dust concentration at the RHVT outlets to determine its mass separation efficiency
- ⤳ Vary, control and measure the specified variables that can have an influence on the RHVT's mass separation efficiency
- ⤳ Measure the temperatures at the inlet and outlets of the RHVT
- ⤳ Work with both compressed air and helium

4.1.1 Experimental Test Apparatus

Figure 11 shows a flow circuit diagram of the experimental test apparatus where the bold numbers refer to the major components and the smaller numbers refer to the pipe diameters in millimetres. Each major component will be discussed, in turn, as follows:

1. Compressed Air Supply/ Helium Cylinder

Compressed air is supplied at 10 bar (absolute) from a compressor and eight 1.51 kg helium cylinders supplied high purity, 99.995 % helium, at 200 bar (absolute) (AFROX, 2000). Both the compressed air and helium may contain traces of oil and other impurities. These impurities have to be filtered out (see item 3) so as not to influence the dust concentration measurement.

2. Pressure Regulator

Since the operating pressure of the experiment is between 3 - 10 bar (absolute), the air/helium pressure has to be reduced. This is done with a pressure regulator. The pressure regulator can manually control the pressure from the compressed air/helium supply by turning the regulator valve to the desired

pressure. The air and helium supplies used different pressure regulators due to their difference in density. A FESTO LR series pressure regulator was used for air while a special regulator (Saffire OGM-5) had to be used to for helium to prevent leakage due to its low density.
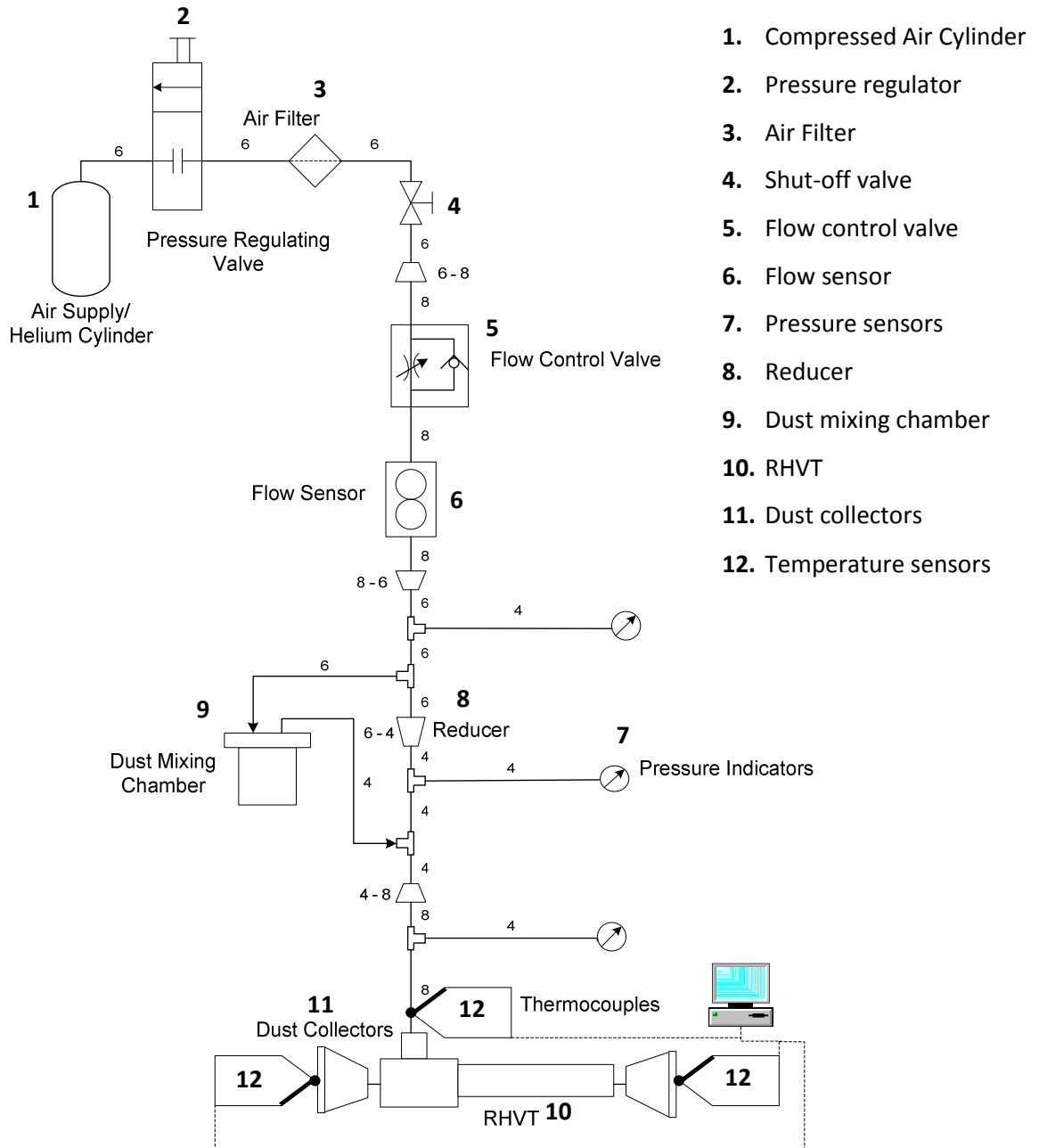
Figure 11: Flow circuit and major components of the experimental setup

3. Air Filter

The air filter used is a FESTO Micro & Fine MS Series filter which has a filtering grade of 1 μm. This filter is used to filter out all the oil traces and impurities with particle sizes larger than 1 μm, from the compressed air/helium supply.

4. Shut-off valve

This valve is a one-way shut off valve which is used to start or stop the flow to the RHVT. It is controlled manually with a control handle.

5. Flow Control Valve

A FESTO QS inline valve controls the flow rate through the experiment. This valve has a control knob that is turned manually to constrict or increase the flow in the tube.

6. Flow Sensor

The flow rate will be varied in the experiments to determine the flow rate at which the maximum dust separation in the RHVT occurs, and thus has to be monitored carefully. A FESTO SFE1 - LF series flow sensor was used that has a range of 10 – 200 L/min and will measure the low air flow rates through the experimental apparatus for the small Exair® RHVT. A larger flow sensor, FESTO MS6-SFE series, with a range of 200 – 5000 L/min was used to measure the higher air flow rates for the medium Exair® RHVT. Both flow sensors require an input voltage of 24 V and this will be supplied by an external power supply. The SFE1 - LF series and the MS6-SFE series has an onboard LCD display that indicates the volumetric flow rate in real-time and therefore no data-logger is required for these flow measurements.

The FESTO sensors were tested in helium and were found to be non-compatible because they gave no rational flow rate values for the helium flow. It was therefore decided to design an orifice flow sensor to be used to measure the

flow rate in helium. The design calculations and the CAD drawings of the orifice flow sensor are given in Appendix A and Addendum I. The FESTO sensors and orifice flow sensors were all calibrated using a Type 55D41/42 calibration unit as shown in Appendix B.

7. Pressure Sensors

FESTO SDE3 pressure sensors will measure the absolute gauge pressure before and after the reducer as well as the pressure at the inlet of the RHVT. The pressure drop across the reducer (item 8 in Figure 11) is the driving force for the injection of the graphite dust into the air/helium stream from the dust mixing chamber (item 9 in Figure 11) and is thus monitored. The pressure sensors have a range of 0 – 10 bar (absolute) and their output is also displayed on an onboard LCD and therefore no data-logger is needed. The SDE3 sensor requires a 24 V input voltage which will be supplied by the same external power supply used to power the FESTO flow sensors.

The pressure drop across the orifice flow meter (used to measure the flow rate in helium) was measured with an Endress and Hauser differential PMD75 pressure sensor. The PMD75 has a range of -3 – 3 kPa. The calibration of this sensor as well as the SDE3 sensors is shown in Appendix B.

8. Reducer

The reducer is a FESTO QS reducer connection that reduces the tube diameter from 6 mm OD to 4 mm OD (4 mm and 2.4 mm ID respectively). The change in tube diameter causes the pressure at the outlet of the reducer to be lower than at the inlet and which in turn causes the dust to be injected into the air/helium stream from the dust mixing chamber.

The pressure difference across the reducer was measured experimentally for different volumetric flow rates as shown in Figure 12. The dashed line is a second order polynomial trendline with a coefficient of determination of 0.967

and was used to show the relation between the volumetric flow rate and the pressure difference across the reducer.
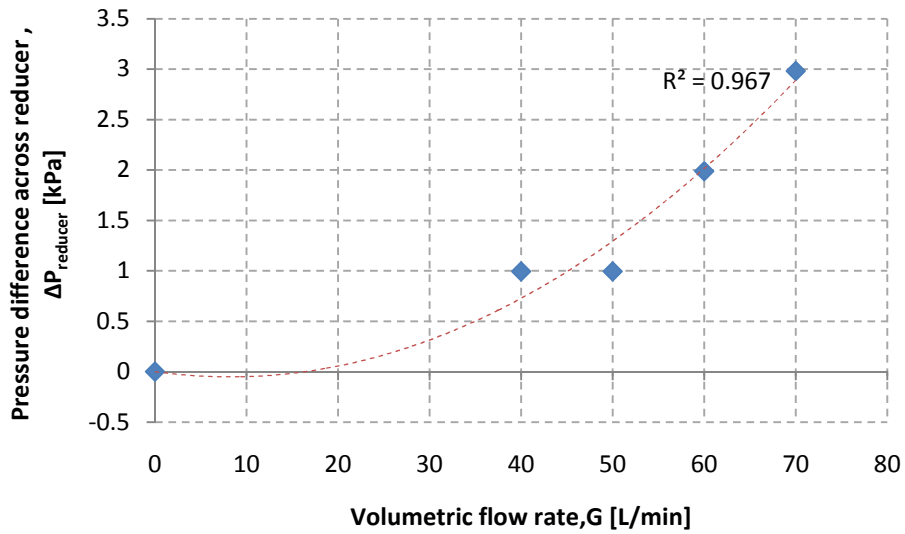
Figure 12: Pressure drop across reducer (item 8 Figure 11) for different volumetric flow rates

9. Dust Mixing Chamber

In the dust mixing chamber (Figure 13) the graphite dust is injected into the air/helium stream. The chamber is essentially a pressure vessel with an inlet and an outlet and contains a predetermined amount of graphite dust. The exact amount of graphite dust held in the chamber is determined by measuring the weight of the chamber without dust and again with dust on a Precisa 405M-200A scale and determining the difference between the two values.
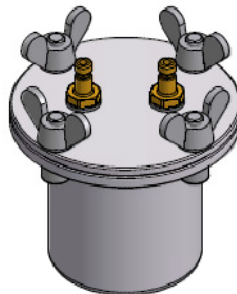
Figure 13: Dust mixing chamber

Air/Helium at a high pressure enters the dust mixing chamber from the main fluid stream, as illustrated in Figure 14 and causes a turbulent flow within the chamber. The chamber outlet is at a lower pressure than the inlet due to the drop in pressure caused by the reducer (item 8). The turbulent flow inside the chamber mixes the air/helium and graphite dust before it is ejected through the outlet into the main fluid stream. This method of dust injection was chosen due to its simplicity and its small resistance to the flow.
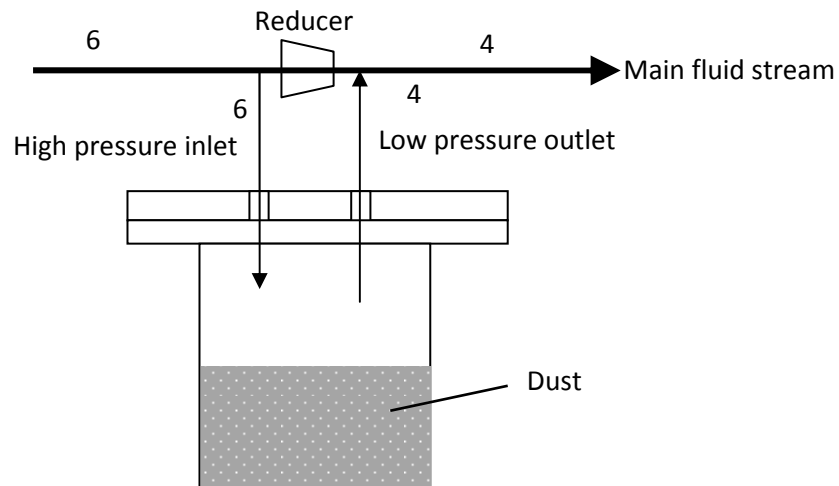
Figure 14: Fluid flow in dust mixing chamber

The chamber is made of aluminium because of its light weight while maintaining its structural strength. The chamber has to be light since the maximum rating of the scale being used to measure the amount of dust ejected from the chamber is 200 g. Therefore the chamber and the dust have to weigh less than 200 g to be measured accurately. The structural integrity of the dust mixing chamber was determined by hydrostatically testing it up to a pressure of 11 bar (absolute). It was experimentally determined that the chamber will operate at a maximum pressure of ± 9 bar (absolute), therefore the chamber has a structural safety factor of at least 1.22. Detailed CAD drawings of the mixing chamber are given in Addendum I.

10. RHVT

The RHVT will be discussed in section 4.1.2.

11. Dust Collectors

The purpose of the dust collectors is to collect the dust particles coming out of the RHVT. A dust collector will be attached to the hot and another to the cold outlet of the RHVT. The dust collectors were also made from aluminium because they were also designed to weigh no more than 200 g so that they could be weighed using the Precisa 405M-200A scale, with a maximum weight allowance of 200 g.

The dust collector consists of a perforated base and a cone distributor, as shown in Figure 15. A fine metal mesh and a collection filter paper are also fitted securely between the cone distributor and the base. The base is perforated to allow air to pass through as well as provide a stable base for the filter paper to rest against, while the cone distributor ensures an even distribution of dust onto the filter paper. The metal mesh is added for extra stability of the filter paper on the base and the filter paper is used to collect the graphite dust particles.

Graphite dust with nominal particle diameters of 1.5 μm (fine dust) and 6.0 μm (coarse dust) were used in the experimental work (see section 4.1.3). The filter paper had to therefore have the proper filtration grade to effectively collect the dust from the RHVT. Ordinary laboratory filter paper (Munktell Filter AB) with a filtration grade of 1 – 2 μm was used with the coarse dust but membrane filters (Sartorius Stedim Biotech, cellulose nitrate filters) with a filtration grade of 0.65 μm had to be used with the fine dust to be able to collect the particles that are smaller than 1 μm in diameter (at least 10 % of the fine dust has particles with diameters smaller than 1 μm, see section 4.1.3).
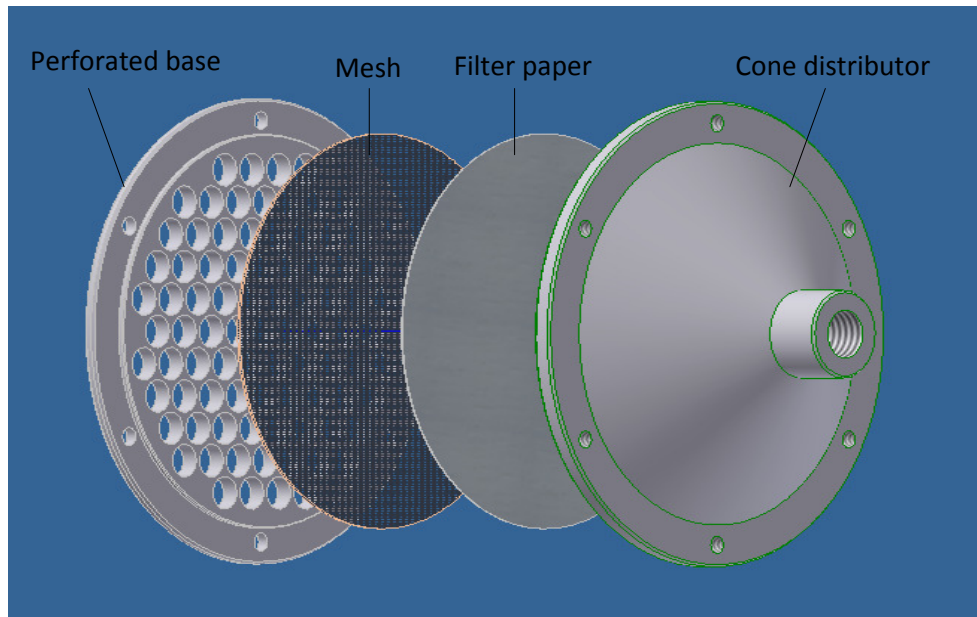
Figure 15: Dust collector

It was found that for high volumetric flow rates, as used with the medium sized Exair® RHVT, the dust collectors did not seal properly. A rubber gasket was therefore added between the cone distributor and the base. The rubber gasket added a weight of approximately 20 g to the collectors but both were still within the Precisa scale's range. A full set of CAD drawings of the dust collector can be seen in Addendum I

The amount of dust captured by the dust collectors can be determined in two ways:

1. Visually, the filter paper can be removed from the collectors and the amount of dust deposited on each filter paper can be compared visually to determine from which outlet of the RHVT the most dust was collected. This method gives only a qualitative result since the exact amount of dust collected on both collectors cannot be determined visually.
2. Experimentally, the amount of dust deposited on the filter paper at both the hot outlet and the cold outlet can be calculated by subtracting the

weight of the collectors before the experiment from the weight of the collectors and the dust after the experiment.

12. Temperature sensors

T-type thermocouples were used to measure the inlet air temperature to the RHVT as well as the outlet temperatures at the hot and cold outlets. T-type thermocouples have a positive copper wire and a negative Constantan wire and are most commonly used in corrosive and sub-zero environments due to its corrosion resistance and wire homogeneity (Veriteq Instruments, 2008). Type T thermocouples have a range of -250 °C to 850 °C (Figliola and Beasley, 2006) which is within the range of the RHVT's temperature capabilities (see Appendix D) . The expected systematic error for a T-type thermocouple is 0.75 % (Figliola and Beasley, 2006) ,which over the temperature range of the RHVT gives an error of less than 1 °C, which is deemed accurate enough to measure the temperature difference between the inlet and both outlets of the RHVT. The thermocouple data was logged by the use of a Schlümberger (SI 35951C IMP) data acquisition card . The thermocouples were calibrated as shown in Appendix B and the measured temperatures for different inlet variables are given in Appendix D.

13. Tubing and connectors

FESTO tubing and connectors are used since they are easy to assemble and disassemble, can withstand high pressures (up to 14 bar (absolute)) and the connectors seal very well. FESTO equipment is generally used for compressed air applications, but it was found after tests with helium that they seal just as effectively when helium is used. Polyurethane tubing was chosen for the 8 mm OD because of its flexibility and polyethylene tubing was chosen for the 4 mm and 6 mm OD tubing due to it is rigidity and high pressure tolerance (max 14 bar (absolute)). The FESTO QS push-in fittings were chosen because they make assembly and disassembly of the experimental setup quick and easy, as well as the fact that reducer and expansion connections were readily available.

4.1.2 RHVT

A small and a medium sized commercially available vortex tubes were used to test the effect of RHVT geometry on the dust separation efficiency. Both sizes RHVT models used are from the Exair® Corporation with the basic layout being that shown in Figure 16. The main components of the Exair® RHVT, as seen in Figure 16, are the vortex generator (which consists out of the inlet nozzles), the tube, hot valve and cold orifice (hexagonal screw).
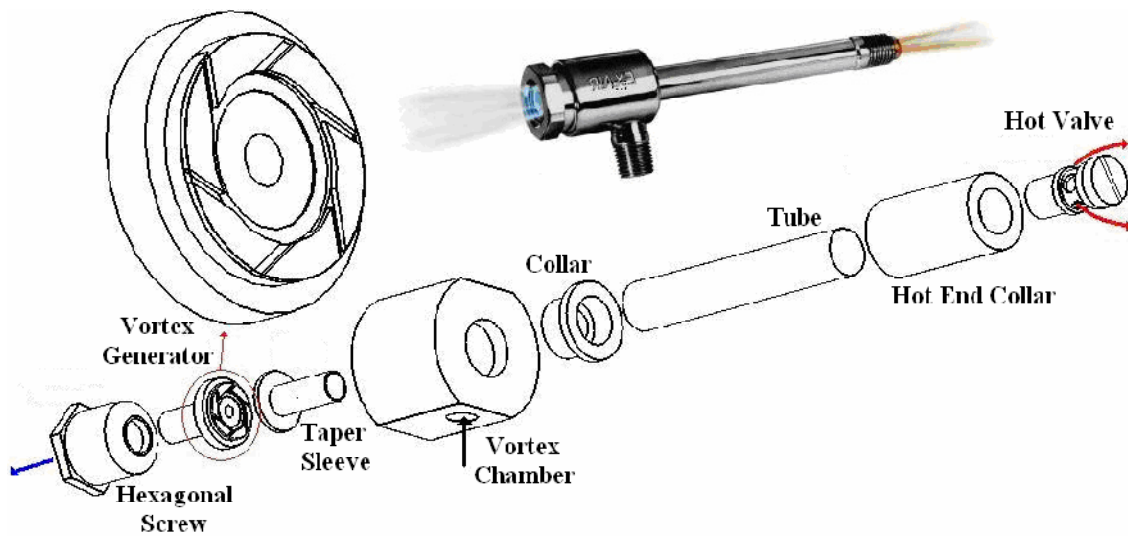
Figure 16: Exair® RHVT components (Etest, 2008)

The RHVT models used in the experiment are the 3202 and 3210 Exair® models with dimensions as shown in Figure 17. These models were chosen for their difference in size and inlet flow rate requirements.
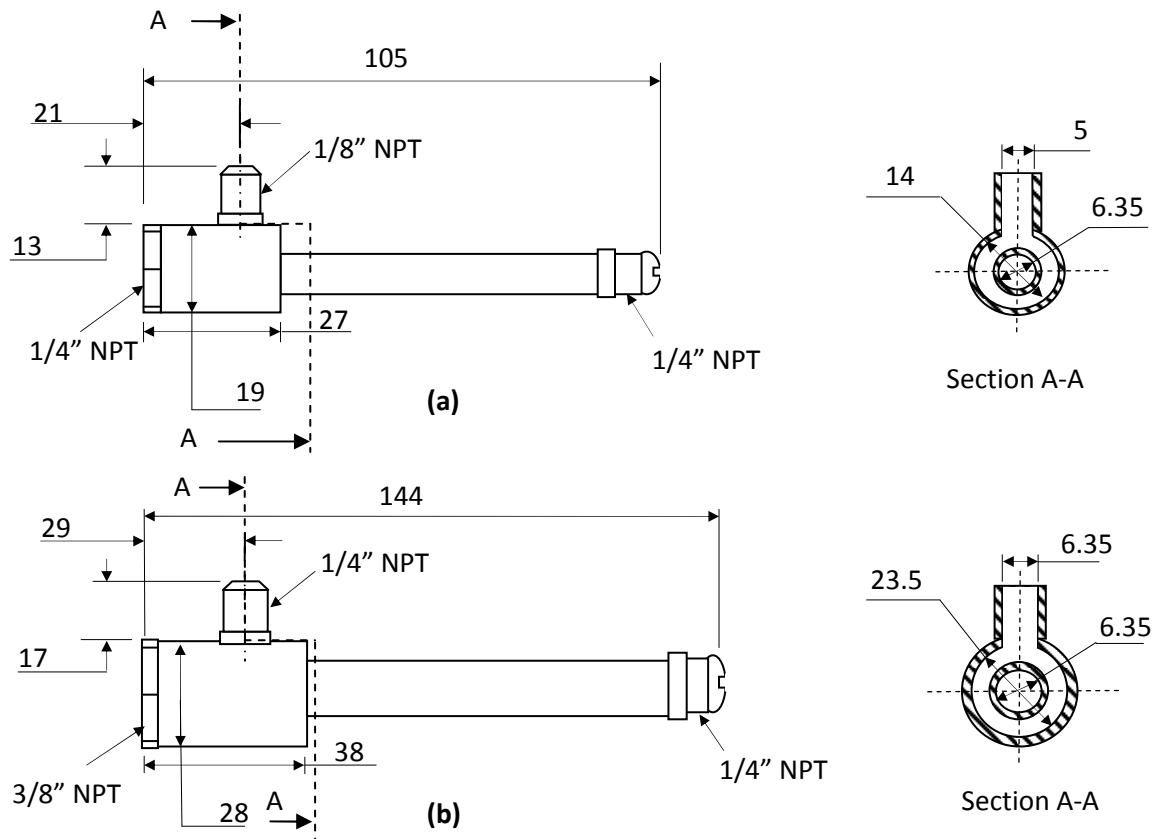
Figure 17: RHVT Dimensions (in mm) (Etest, 2008) of the small size model 3202 (a) and
the medium sized model 3210 (b) RHVTs

Each RHVT model has a rated inlet volumetric flow rate (at an inlet pressure of 6.9 bar)
and maximum cooling power and exhausts to atmosphere. The specifications for each
model are summarized in Table 1.

Table 1: Exair® RHVT model specifications (at 6.9 bar supply pressure)(Etest, 2008)

Model	Size	Maximum cooling power [kJ/hr]	Rated volumetric flow rate [L/min]
3202	Small	142.4	57
3210	Medium	686.6	283

4.1.3 Graphite Dust

The graphite dust used in this experiment is a carbon/ash mixture with a carbon content of 96 – 97 % and is used, for example, in powder metallurgy for sintering automobile parts. The graphite dust grade used for this experiment was Ultra Fine Grinding 4 (UF4 96/97) and Very Fine Grinding (VF) grade graphite dust from Graphit Krofpmühl AG (2008), which is a German based company. The particle size distribution of both dust grades is given by their physical/chemical data sheet as shown in Table 2 (obtained through laser diffraction). The left column in Table 2 denotes the statistical percentile of the dust particles with the specified particle diameter, for example d_{10} means that 10 % of the particles, within a representative sample of the VF dust, have a particle diameter of 0.7 μm. From this table the nominal particle sizes are indicated by d_{50} which means that the UF4 96/97 dust has a nominal particle diameter of 6 μm and the VF dust has a nominal particle diameter of 1.5 μm.

Table 2: Graphite dust particle size distribution (Graphit Krofpmühl AG, 2008)

	UF4 96/97	VF
d_{10}	2.6 μm	0.7 μm
d_{50}	6 μm	1.5 μm
d_{90}	11 μm	2.9 μm

According to Bäumer (1990) the nominal diameter of the graphite particles found in the AVR was 0.76 μm. Unfortunately, graphite dust that fine is not commercially available. It was attempted to grind the dust bought from Graphit Kropfmühl finer with a roller grinder and a pulveriser (which was the equipment available in the laboratory).

Firstly the roller grinder was attempted. The Graphit Kropfmühl dust was put into a ceramic container together with ceramic balls with diameters ranging from 10 mm – 30 mm. The ratio of the ceramic balls to the dust was 60:40. Then the ceramic container was put onto the roller grinder for 3 hours. A particle size analysis (PSA) was then done, using a Saturn DigiSizer 5200 from Micromeritics Instrument Corporation, to determine the resulting particle diameters. The results showed that after 3 hours, on the roller grinder, only 0.1 % of the volume of the graphite dust had a particle diameter of less

than 1 µm. Due to this poor result after a 3 hour grinding period, it was decided to rather attempt to grind the dust finer with a pulveriser. The graphite dust was thus pulverized for intervals of 5 min and for a total time of 30 min. Another PSA was then done to determine the resulting particle diameters. The PSA showed rather peculiar results in that the mean diameter of the particles increased with the duration of the pulverisation which could possibly be attributed to agglomeration. The results did show, however, that the percentage of particles with a diameter less than 1 µm increased from 0.1 % to 3 %. Although this was an improvement compared with the roller grinder it was still not enough to warrant any further pulverisation and the attempt to grind the Graphit Kropfmühl dust finer was discarded.

4.2 Operational and Safety Procedures

The operational procedures used for the experimental work as well as the safety procedures followed during each experiment are discussed in this section.

4.2.1 Operational Procedure

First the experimental setup has to be built up as follows:

- ⇢ Connect tubing, connectors, sensors, RHVT etc. according to the experimental setup diagram (Figure 11)
- ⇢ Connect sensors to power supply
- ⇢ Ensure that all tubing, connectors and sensors are connected securely

The experimental procedure requires that the following steps be followed:

1. Make sure the shut-off valve is closed, and that the dust mixing chamber and dust collectors are not connected
2. Set pressure regulator to high pressure, 8 bar for small RHVT air tests, 10 bar for medium RHVT air tests, 6 bar for helium tests
3. Open shut-off valve and set desired flow rate by setting the control valve, also check that the pressure regulator value remains at the value set in step 2
4. Leave shut-off valve open for 5 min to ensure that there is no water in the system, and that all excess graphite dust in the pipes and RHVT is exhausted
5. Close shut-off valve

6. Insert graphite dust into dust mixing chamber

7. Weigh dust mixing chamber

8. Insert filter papers into dust collectors

9. Weigh dust collectors

10. Connect dust mixing chamber to experimental setup, and dust collectors to the RHVT

11. Open shut-off valve and start timer, 45 minutes for small RHVT air tests, 20 minutes for medium RHVT air tests, 30 minutes for helium tests

12. Log sensor data, i.e. flow rate and pressure every 10 minutes

13. Turn off flow after timer stops by closing the shut-off valve

14. Disconnect dust mixing chamber and dust collectors

15. Leave dust collectors in secure place to reach ambient temperature and moisture conditions. Wait 3 hours for small RHVT air tests, 12 hours for medium RHVT air tests and 3 hours for helium tests

16. Weigh dust mixing chamber and dust collectors

17. Photograph filter papers and catalogue

18. Check and/or change variables (volumetric flow rate, volume fraction, RHVT geometry, working fluid or dust particle size)

19. Repeat steps 1 – 18

4.2.1 Safety Procedures

A hazard can be defined as a possible source of danger which might jeopardize the safety of personnel and equipment. In this section the potential hazards inherent to the experimental setup are discussed as well as their impact on the laboratory environment and also what preventative measures can be taken to minimize the hazards if they should occur. The possible hazards are categorized according to their impact as prescribed by the Stellenbosch Mechanical and Mechatronic Department (Mechanical and Mechatronic Department, 2009).

Catastrophic hazard

→ Inside the encasement of the voltage supply, needed to power the Festo sensors, are capacitors that store energy. This energy is only released when

a short circuit is created between the two electrodes and this would cause an electric shock.

Critical hazard

⇢ The connectors or piping can fail or disconnect during testing which could lead to serious injury and damage to the equipment/operator. The piping and connectors are checked before each test, and safety glasses are worn at all times.

⇢ If the connectors or piping should fail during a dust experiment graphite dust will be blown into the environment and could be inhaled by the operator. This can be prevented by wearing a dust mask during the running of the experiment.

⇢ The RHVT makes an ear-piercing high pitched sound when it is running which could cause hearing problems after long term exposure. Therefore ear-plugs must be worn at all times.

Marginal hazard

⇢ The helium supply cylinder can fall over and cause damage to the equipment. This is prevented by securing the helium cylinder to the wall of the laboratory with a chain.

Negligible hazard

⇢ There could be a loss of helium due to connections being incorrectly connected, which can be prevented by ensuring that the piping is connected properly.

4.3 Experimental Errors

There are a number of possible experimental errors that can influence the accuracy of the experimentally measured results. Some of these experimental errors are inherent to the measurement equipment such as its accuracy and reproducibility, while some errors for example are due to incorrect calibration of this equipment. The measuring

equipment accuracy and reproducibility as specified by the manufacturer (FESTO, 2008) are as follows:

Pressure measurement

(FESTO SDE3 pressure sensors)

Accuracy: ± 2 % full scale

Reproducibility: ± 0. 3 % full scale

(Endress and Hauser PMD75 pressure sensor)

Maximum linearity error: ± 0.15 %

Flow measurement

(FESTO SFE1 - LF and MS6-SFE flow sensors)

Accuracy: ± 3 % o.m.v. (on machine verification) + 0.3 % full scale

Reproducibility: ± 0.8 % o.m.v. + 0.2 % full scale

As can be seen from the information above, the sensors are not 100 % accurate. To prevent further inaccuracies the sensors therefore have to be calibrated carefully. Calibration errors can occur through two sources: Firstly the manner in which the calibration standard is applied to the measuring device and secondly systematic and random errors inherent to the calibration standard (Figliola and Beasley, 2006). The first source of calibration errors can be prevented in this experiment by making sure the rules of applying the standard (British Standards Institution, 1981) to the measuring equipment is adhered to. The second error source is the inherent uncertainty within the standard and can therefore not be prevented, which is why there will always be a slight difference between the value supplied by the standard and the calibration value sensed by the measuring device.

Another source of error is systematic and random errors. A systematic error is also known as a bias error and remains constant in repeated measurements (Figliola and Beasley, 2006). A systematic error can be estimated by comparing the measurement to a standard, i.e. calibration. Although calibration can reduce systematic errors it cannot

eliminate them all. Random errors vary randomly in repeated measurements (Figliola and Beasley, 2006). Random errors, which are also called precision errors, are affected by the resolution and repeatability of the measurement devices (see paragraphs above). These errors result in scattered measured results for repeated tests with fixed operating conditions. Because of the randomness of these errors, exact values cannot be obtained from measurement sensors but probable estimates can be made through statistical analyses. During the experimental work the random and systematic errors were restricted by firstly doing a set of at least 5 repeated tests with fixed operating conditions and secondly by doing a statistical analysis to determine the outliers caused by random errors.

Data-acquisition errors can also occur during the measuring process. These errors include all errors that arise during the actual measuring of the data. These errors include measurement system operating conditions and sensor installation effects.
The measurement system operating conditions must remain constant throughout the measurement to avoid errors. This was achieved by monitoring the environmental and test apparatus conditions throughout the duration of each experiment. Errors can also arise if the pressure and flow sensors are not installed properly. The instruction/ operation manual was thus consulted before each sensor was installed and the guidelines were followed accurately.

4.4 Experimental Results

The dust collectors were used to determine the dust separation efficiency of the RHVT by collecting the graphite dust from the respective outlets. As stated in section 4.1 item 11, the amount of dust collected by the dust collectors can be determined in two ways: visually and experimentally. The visual method only gives a qualitative indication of the dust separation efficiency but the difference in dust collected on the hot outlet and cold outlet filter papers is clearly visible, as seen in Figure 18.
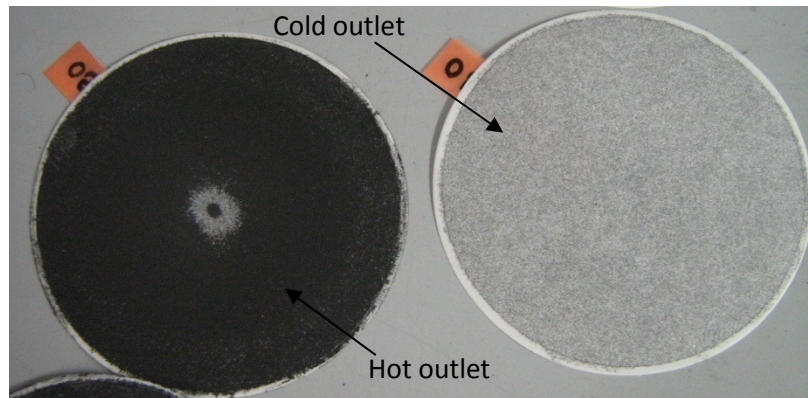
Figure 18: Dust collector filterpapers showing the difference in graphite dust collected on the hot outlet and cold outlet sides

In the experimental method the mass of the dust collectors were weighed before and after an experiment and these measured masses were then subtracted from each other to determine the amount of dust collected by each dust collector. From these measurements the dust separation efficiency quantity was determined as the ratio of the mass of dust collected by the hot outlet dust collector m_h to the total mass of dust collected by both dust collectors $m_h + m_c$, as seen in equation 2.

$$\eta = \frac{m_h}{m_c + m_h} \qquad\qquad 2$$

Table 3 summarises the experimental results of the measured dust separation efficiency for different values of the measured variables. To prevent systematic errors, a minimum of 5 tests were done for each variable configuration shown in the table. The table shows the average dust separation efficiency results calculated after a statistical analysis was done on the raw data (see Appendix E). The statistical analysis included calculating the standard deviation of all the measured efficiency values for each set of tests and then excluding the values which had a large standard deviation from the average value calculation.

Table 3: Experimental results

η [%]	G [L/min]	μ_c	Working fluid	Geometry	Dust particle size [μm]
94.4	77	0.732	Air	Small	6
92.4	77	0.36	Air	Small	6
89.5	77	0.159	Air	Small	6
86.4	64	0.732	Air	Small	6
93	90	0.732	Air	Small	6
89	280	0.777	Air	Medium	6
93	280	0.54	Air	Medium	6
96	280	0.92	Air	Medium	6
92	290	0.777	Air	Medium	6
94	250	0.777	Air	Medium	6
91.5	40	0.732	Helium	Small	6
92.3	40	0.36	Helium	Small	6
85.1	40	0.732	Helium	Small	1.5
88.9	77	0.732	Air	Small	1.5
96	280	0.777	Air	Medium	1.5

To find a correlation between the independent variables (measured variables) and the dust separation efficiency, the dependant variable, a data regression analysis was done. To be able to do the regression all independent variables had to be quantified. The two variables not quantified are working fluid and geometry. The geometry was then quantified as the ratio of the outer vortex generator diameter d_v to the length of the RHVT L, which is 0.133 for the small Exair® RHVT and 0.163 for the medium Exair® RHVT. The working fluid was quantified as the dimensionless quantity $\mathcal{R}/c_p$, where $\mathcal{R}$ is the specific gas constant and c_p is the specific heat capacity taken at constant pressure. At the operating pressure and temperature of the experiments these values were taken as follows (Çengel and Boles, 2001):

Table 4: Working fluid variable quantities

Material	$\mathcal{R}$ [J/kgK]	c_p [J/kgK]	$\mathcal{R}/c_p$
Air	287	1005	0.2855
Helium	2079	5165	0.4025

The first step in regression is to choose a curve fit that best suits the data. It was decided to test a linear, polynomial, power and exponential regression curve fit. The equations of these curves are:

Linear
$$y = a + b_1 x_1 + b_2 x_2 + b_3 x_3 + b_4 x_4 + b_5 x_5$$
3

Polynomial
$$y = a + b_1 x_1{}^5 + b_2 x_2{}^1 + b_3 x_3{}^3 + b_4 x_4{}^4 + b_5 x_5{}^2$$
4

Power
$$y = a x_1{}^{b_1} x_2{}^{b_2} x_3{}^{b_3} x_4{}^{b_4} x_5{}^{b_5}$$
5

Exponential
$$y = e^{(a + b_1 x_1 + b_2 x_2 + b_3 x_3 + b_4 x_4 + b_5 x_5)}$$
6

The variables were assigned as shown in Table 5:

Table 5: Regression variable assignment

Variable	Symbol	Assignment	Weight
Dust separation efficiency	η	y	
Volume flow rate	G	x_1	1
Volume fraction	μ_c	x_2	5
Working fluid	$\mathcal{R}/c_p$	x_3	3
Geometry	d_v/L	x_4	2
Dust particle diameter	d_p	x_5	4

The polynomial equation was determined after calculating the weight of each independent variable's influence on the dust separation efficiency and then assigning

the variables with the most weight to the higher order polynomial values. The weights of the independent variables were determined by doing a regression analysis on each variable and then comparing their coefficient of determination (R^2-value). The variable with the highest R^2-value was assigned the most weight. In Table 5 the different variables are assigned a number from 1 – 5 with 1 being the variable with the most weight and 5 being the least.

The regression analysis was done with 58 different data points which were taken from the processed experimental results (see Appendix E). The processed experimental results exclude all values that were determined to be outliers after the statistical analysis was done. The regression analysis calculated the values of the unknown constants for each curve fit, as well as the curve fits' coefficient of determination and the percentage error between the dust separation efficiency value predicted by the curve fit and the actual efficiency as shown in Table 6.

Table 6: Regression results

	Linear	Polynomial	Power	Exponential
Constant	Value	Value	Value	Value
a_1	98.600	88.4	4.06775	0.000304
b_1	0.029	497.5×10^{-15}	0.06232	-0.013519
b_2	-1.259	-0.8094	-0.00469	0.034798
b_3	3.510	-18.9	0.09728	-0.985233
b_4	-95.008	4744.281	-0.24066	4524.315749
b_5	421407	59.1×10^9	0.01619	4.588935
R^2-value	0.254	0.219	0.290	0.250
% error	2.811	2.877	2.770	2.817

The R^2-values for all of the curve fits are very poor with an approximate value of 0.2 but gave a reasonably good percentage error between the predicted and actual values of the dust separation efficiency of approximately 2.8 %. All the curve fits showed very similar results but from Table 6 it is seen that the power curve fit gave the best results with an R^2 - value of 0.290.

5. THEORETICAL MODELLING

The theoretical analysis done in this chapter was done to gain a better understanding as to how the temperature and mass separation happens inside the RHVT. An analytical analysis was done using the conservation equations and basic thermo - physical principles to macroscopically model the flow. A numerical analysis using computational fluid dynamics (CFD) was also done to gain insight into the flow, particle movement and other physical parameters such as temperature and pressure.

5.1 Analytical Analysis

In this section an analysis is done to try and explain the temperature separation mechanism and particle separation in a RHVT in terms of well-known thermo-physical principals.

5.1.1 Temperature Separation

Referring to Figure 19 the flow within a RHVT can be described thus: The compressed fluid enters the cylindrical tube from the supply tube through one or more narrow inclined nozzles and then tends to flow in a rotational θ-direction about the longitudinal z-axis. This rotational flow is termed a vortex. At the other end of the cylindrical tube, the flow control device diverts the flow into two streams, an outer stream $\dot{m}_h$, through the annular area between the cylindrical tube inner wall and the flow control device and an inner central stream $\dot{m}_c$, which exits at the opposite end of the tube through a centrally located orifice. Under favourable geometric and operating conditions the outer stream, created by the flow control device, and exhausting from the outer peripheral opening is hotter than the inlet stream, whilst the centrally exiting stream is colder than the inlet stream. This change in temperature is loosely termed "temperature separation" and is characterized by the cold volume fraction μ_c (defined as $\mu_c = \frac{G_c}{G_i}$). With a decrease in volume fraction the cold stream air temperature decreases and the hot stream temperature also decreases. Similarly when the volume fraction increases, the hot stream temperature increases and the cold stream temperature also increase. This temperature dependence on volume fraction is shown in Appendix D.
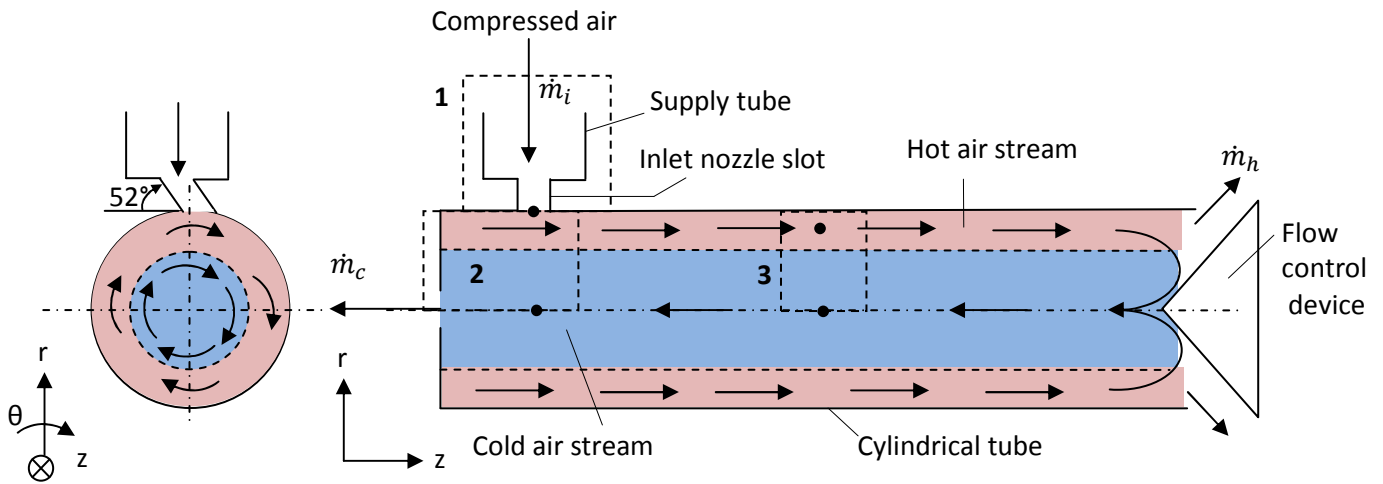
Figure 19: Flow in a RHVT

To explain the rotational flow in the RHVT, the r-θ plane of Figure 19 may be considered as a result of two coaxial rotating cylinders, with the area between the outer cylinder and the wall of the inner cylinder representing the hot air stream and the area inside the inner cylinder representing the cold air stream, as illustrated in Figure 20. The wall of the inner cylinder may be considered porous so that the flow can pass through unhindered. Both cylinders are rotating in the same direction with an angular velocity Ω and an outer cylinder radius of R.

The following assumptions are then made:

- Steady state
- Turbulent flow
- Compressible flow
- Fluid moves in circular pattern (with v_z and v_r zero)
- No pressure gradient in the θ - direction
- Gravity is negligible
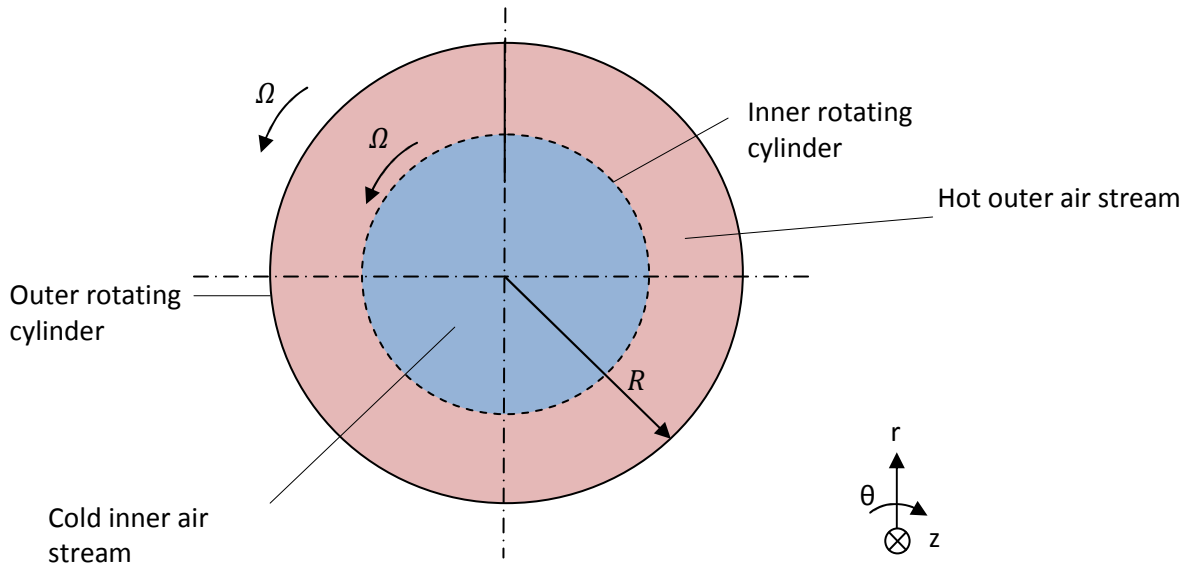
Figure 20: The r-θ plane of the RHVT (Figure 19) as two rotating coaxial cylinders

The velocity distribution is determined by solving the conservation equations of continuity and momentum (Bird et al., 2002). Applying the aforementioned assumptions to the equation of continuity in cylindrical coordinates

$$\frac{\partial \rho}{\partial t} + \frac{1}{r}\frac{\partial}{\partial r}(\rho r v_r) + \frac{1}{r}\frac{\partial}{\partial \theta}(\rho v_\theta) + \frac{\partial}{\partial z}(\rho v_z) = 0 \qquad 7$$

gives

$$\frac{\partial \rho}{\partial t} + \frac{1}{r}\frac{\partial}{\partial r}(\rho r v_r) = 0 \qquad 8$$

For equation 8 to be valid both terms of the equation must equal 0. Therefore $\frac{\partial \rho}{\partial t} = 0$ and $\frac{1}{r}\frac{\partial}{\partial r}(\rho r v_r) = 0$.

The equations of momentum in cylindrical coordinates in the r, z and θ direction are:

$$\left(\frac{\partial(\rho v_r)}{t} + v_r \frac{\partial(\rho v_r)}{\partial r} + \frac{v_\theta}{r}\frac{\partial(\rho v_r)}{\partial \theta} - \frac{\rho v_\theta{}^2}{r} + v_z \frac{\partial(\rho v_r)}{\partial z}\right)$$

$$= -\frac{\partial P}{\partial r} + \left[\frac{\partial}{\partial r}\left(\frac{\mu}{r}\frac{\partial}{\partial r}(rv_r)\right) + \frac{\mu}{r^2}\frac{\partial^2 v_r}{\partial \theta^2} - \frac{2\mu}{r^2}\frac{\partial v_\theta}{\partial \theta} + \frac{\partial^2 \mu v_r}{\partial z^2}\right] \qquad 9$$

$$+ \rho g_r$$

$$\left(\frac{\partial(\rho v_\theta)}{t} + v_r \frac{\partial(\rho v_\theta)}{\partial r} + \frac{v_\theta}{r}\frac{\partial(\rho v_\theta)}{\partial \theta} + \frac{\rho v_r v_\theta}{r} + v_z \frac{\partial(\rho v_\theta)}{\partial z}\right)$$

$$= -\frac{1}{r}\frac{\partial P}{\partial \theta} + \left[\frac{\partial}{\partial r}\left(\frac{\mu}{r}\frac{\partial}{\partial r}(rv_\theta)\right) + \frac{\mu}{r^2}\frac{\partial^2 v_\theta}{\partial \theta^2} + \frac{2\mu}{r^2}\frac{\partial v_r}{\partial \theta} + \frac{\partial^2 \mu v_\theta}{\partial z^2}\right] \qquad 10$$

$$+ \rho g_\theta$$

$$\rho\left(\frac{\partial(\rho v_z)}{t} + v_r \frac{\partial(\rho v_z)}{\partial r} + \frac{v_\theta}{r}\frac{\partial(\rho v_z)}{\partial \theta} + v_z \frac{\partial(\rho v_z)}{\partial z}\right)$$

$$= -\frac{\partial P}{\partial z} + \left[\frac{\mu}{r}\frac{\partial}{\partial r}\left(r\frac{\partial v_z}{\partial r}\right) + \frac{\mu}{r^2}\frac{\partial^2 v_z}{\partial \theta^2} + \frac{\partial^2 \mu v_z}{\partial z^2}\right] + \rho g_z$$

$$\qquad 11$$

Taking all assumptions and the zero terms of the continuity equation into account, the equations of momentum reduce to:

r - component
$$-\rho\frac{v_\theta{}^2}{r} = -\frac{\partial P}{\partial r} \qquad\qquad 12$$

θ - component
$$0 = \frac{d}{dr}\left(\frac{\mu}{r}\frac{d}{dr}(rv_\theta)\right) \qquad\qquad 13$$

z - component
$$0 = -\frac{\partial P}{\partial z} \qquad\qquad 14$$

These equations do not include the source terms for turbulence. It is assumed that the flow within the RHVT is turbulent; therefore turbulence must be accounted for. Turbulent flow is characterized by complex eddying motion which causes fluctuations in the velocity components, pressure and temperature of the flow. It was decided to account for turbulence by using an effective viscosity term. In turbulent flow the effective viscosity is defined as $\mu_{eff} = \mu + \mu_t$, where μ is the molecular viscosity and μ_t is the turbulent viscosity (Mills, 1999). The turbulent viscosity term accounts for the

fluctuations in the velocity components due to momentum transport by the eddies (Mills, 1999). A simple model for the effective viscosity distribution in the r-θ plane of the RHVT flow was assumed to be

$$\mu_{eff} = \mu + \mu_t = ar^b \qquad\qquad 15$$

where a and b are arbitrary constants and $b < 1$. This model assumes that the viscosity increases from the centre of the flow to the outer cylinder wall as illustrated in Figure 21.
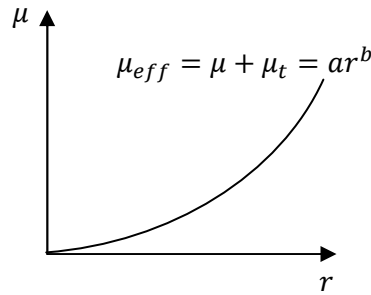
Figure 21: Turbulent viscosity model

Taking this turbulent viscosity model (equation 15) into consideration and integrating equation 13 with respect to r with boundary conditions, $r = 0$, $v_\theta = 0$ and $r = R$, $v_\theta = R\Omega$ results in

$$v_\theta = \frac{\Omega}{R^{-b}} r^{(1-b)} \qquad\qquad 16$$

The radial pressure distribution in the r-θ plane of the RHVT flow can be calculated by substituting the calculated rotational velocity distribution (equation 16) into equation 12 and integrating with respect to r. The pressure within the RHVT is not known, therefore the boundary condition was assumed to be $r = 0$, $P = P_{atm}$ (to be motivated later) with the result being

$$P_r = \frac{\rho\Omega^2}{R^{-2b}(3-2b)} r^{3-2b} + P_{atm} \qquad\qquad 17$$

The rotational velocity distribution (equation 16) and radial pressure distribution (equation 17) was plotted as shown in Figure 22 using the input values shown in Table 7

for different values of b. a is seen to have no influence on the velocity and pressure distributions due to cancellation. The values of the variables shown in Table 7 were obtained from the small Exair® RHVT geometric and experimental data.

Table 7: Analytical example input variables

Variable	Symbol	Value
Constant	a	1
Exponent	b	0, 0.5, 0.7, 0.9
Radius [mm]	R	3.175
Angular velocity [rad/s]	Ω	55338
Density [kg/m^3]	ρ	7

From Figure 22 it is seen that the viscosity model constant b has a significant influence on the rotational velocity. For $b = 0$ the flow is laminar because the turbulent viscosity term in the effective viscosity becomes zero. As shown in Figure 22 the velocity of the rotating fluid increases from the centre towards the wall of the outer rotating cylinder; also with an increase in b the velocity increases more quickly in the central region of the flow. As b increases the effective viscosity increases which in turn increases the resistance to flow near the wall of the outer rotating cylinder which is why the velocity increase near the outer wall is less than in the central flow region as seen in the case of $b = 0.9$. The maximum rotational velocity occurs at the outer cylinder wall and the magnitude is calculated to be approximately 180 m/s for all values of b.

Figure 23 shows that the radial pressure increases from the centre of the flow towards the outer cylinder wall. The pressure difference between the outer cylinder wall and the centre of the flow also increases with an increase in the value of b.
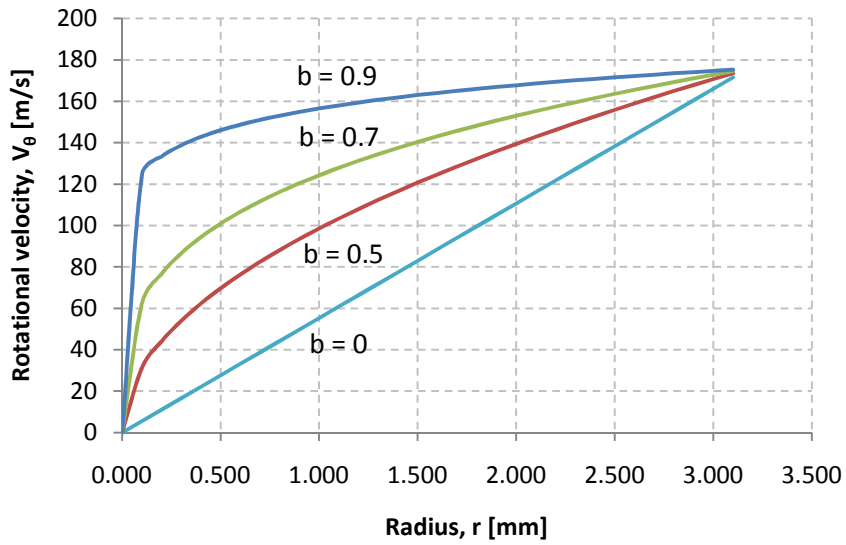
Figure 22: Rotational velocity distribution for different values of b in the effective viscosity model $\mu_{eff} = ar^b$
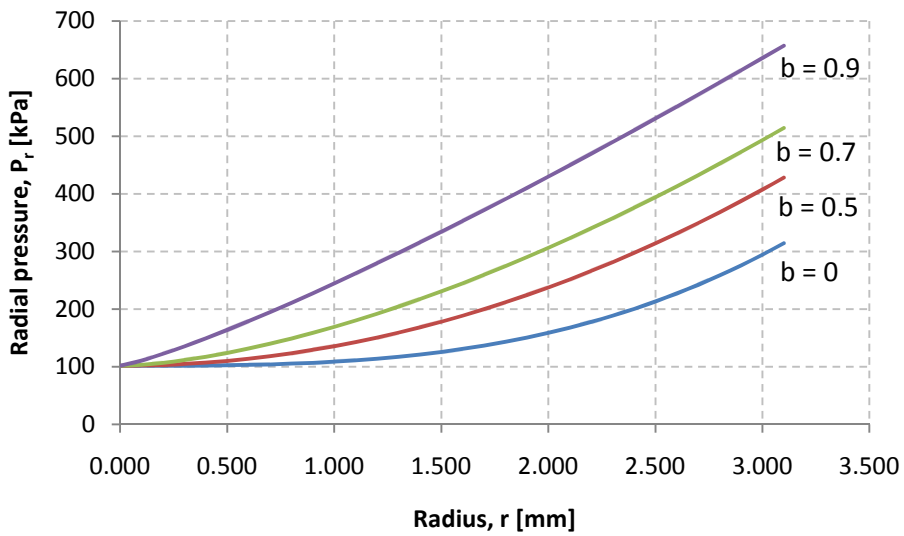
Figure 23: Radial pressure distribution for different values of b in the effective viscosity model $\mu_{eff} = ar^b$

Now that the rotational flow within the RHVT has been modelled with the aid of the calculated rotational velocity and radial pressure profiles, the temperature separation effect can be modelled in light of this flow regime and basic thermo-physical principles.

Considering Figure 19, it is seen that the RHVT is further divided into three control volumes: control volume 1 at the entrance of the RHVT where the compressed air enters the inlet nozzles from the supply tube, control volume 2 at the flow region where the flow enters the cylindrical tube from the inlet nozzles and exits through the cold orifice and control volume 3 further down the length of the cylindrical tube. To explain the temperature separation in the RHVT, it has to be explained how the inlet air is both cooled and heated in the tube, causing the temperature of the air exhausting from the RHVT outlets to be either much hotter or much colder than the inlet air. The cooling of the inlet air will be investigated first.

Considering the first control volume (Figure 24), in which compressed air enters the RHVT through a supply tube and then flows through 6 inlet nozzles to the cylindrical tube (see Figure 16). The first control volume models the six inlet nozzles as a single nozzle for simplicity, as seen in Figure 24.
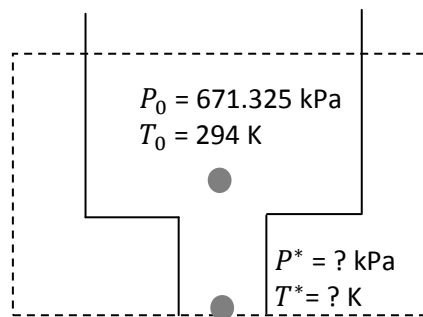
Figure 24: RHVT control volume 1 in Figure 19

The total flow area and entrance angle of all 6 inlet nozzles was shown in Appendix C to be 0.924 x 10^{-6} m^2 and 52˚ respectively. The stagnation pressure and temperature conditions at the nozzle inlet, assuming negligible velocity in the supply tube, were measured experimentally to be $P_0 = 570$ kPa (gauge) $= 671.325$ kPa (abs) and $T_0 = 294$ K in air with an isentropic coefficient $k = 1.4$ and specific gas constant $\mathcal{R} = 287$ J/kg·K.

If control volume 1 is considered to be an isentropic duct, from White (2003) it is then determined that sonic or critical flow occurs at the minimum area A^* within the duct if there are no shockwaves. The exit area of the inlet nozzles is the minimum area within

55

control volume 1, and hence the flow through the nozzles are at sonic point (or critical).
The corresponding critical pressure, temperature and velocity of the air at the outlet of
the inlet nozzles at sonic point can be calculated as (White, 2003)

$$P^* = P_0 \left(\frac{2}{k+1}\right)^{k/(k-1)} = 671325 \times 0.5283 = 351.103 \text{ kPa (abs)} \qquad 18$$

$$T^* = T_0 \frac{2}{k+1} = 294 \times 0.8333 = 245 \text{ K} \qquad 19$$

$$V^* = \sqrt{k\mathcal{R}T^*} = \sqrt{1.4 \times 287 \times 245} = 313.38 \text{ m/s} \qquad 20$$

By comparing the inlet and outlet conditions of the inlet nozzles it is shown that the air
temperature greatly decreases by 49°C (294 K to 245 K) as it enters the cylindrical tube
of the RHVT. Similarly the temperature drop across the inlet nozzles will be 73°C (294 K
to 221 K) for helium with $k = 1.66$ and $\mathcal{R} = 2.0769$.

To verify the validity of these calculations, the assumption made regarding stagnation
conditions in the supply tube has to be verified. In order to do this the speed of the air
a_{air} and the Mach number Ma in the supply tube have to be calculated. The supply
tube has an inner diameter of 5 mm; therefore its cross-sectional area A_{supply} is
19.6 mm². The density of the air is calculated using the ideal gas law:

$$\rho = \frac{P_0}{\mathcal{R}T_0} = \frac{671325}{287 \times 294} = 7.95 \text{ kg/m}^3 \qquad 21$$

The speed of the air, corresponding to the value of $\dot{m}_{max}$ (calculated in Appendix C), is
therefore:

$$V_{max} = \frac{\dot{m}_{max}}{pA_{supply}} = \frac{0.00146}{7.95 \times 19.6 \times 10^{-6}} = 9.369 \text{ m/s} \qquad 22$$

The speed of air is approximated as

$$a_{air} = \sqrt{kRT_0} = \sqrt{1.4 \times 287 \times 294} = 343.7 \text{ m/s} \sim 344 \text{ m/s} \qquad 23$$

hence the Mach number is

$$Ma = \frac{V_{max}}{344} = \frac{9.369}{344} = 0.027 \qquad\qquad 24$$

This Mach number is too low to give any appreciable increase in both the stagnation pressure and temperature over the corresponding measured inlet values. The assumption is therefore valid.

Control volume 2 (Figure 25) shows the entrance region of the RHVT, where the flow from the inlet nozzles enter the cylindrical tube of the RHVT and exhaust through the cold outlet.
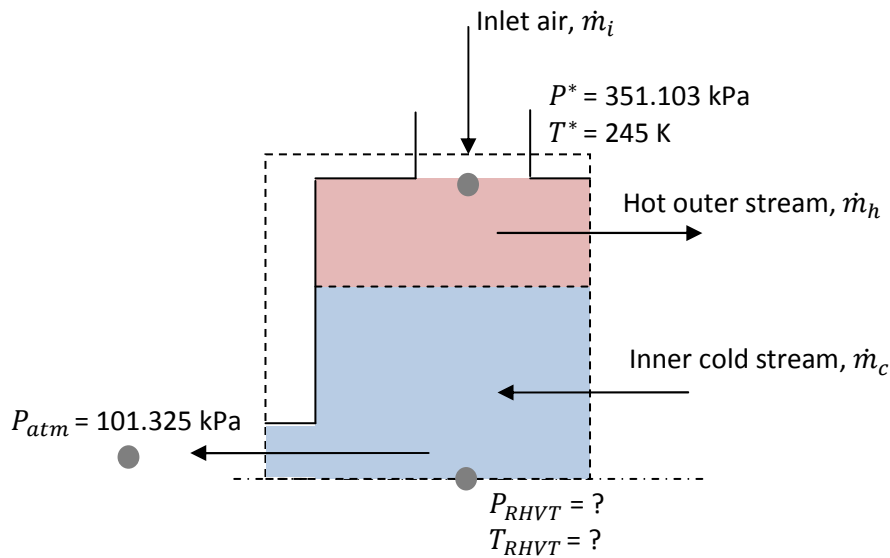
Figure 25: RHVT control volume 2 in Figure 19

The radial pressure distribution was calculated with the assumption that the pressure at the centre of the RHVT is at atmospheric pressure. In this control volume this assumption can be validated by the fact that P_{RHVT} is very close to the cold outlet which exhausts to atmospheric pressure. If it is then assumed that $P_{RHVT} = P_{atm}$, the pressure at the nozzle outlet is at a higher pressure than at the centre of the RHVT and this will cause the air to expand isentropically at the centre of control volume 2. Isentropic expansion can be illustrated as follows: consider a frictionless piston-cylinder device as shown in Figure 26; the air, an ideal gas, inside the cylinder is compressed due to the

force (pressure) exerted on it by the piston, and when the force (pressure) is released the volume of the air is allowed to expand and the piston moves upwards.
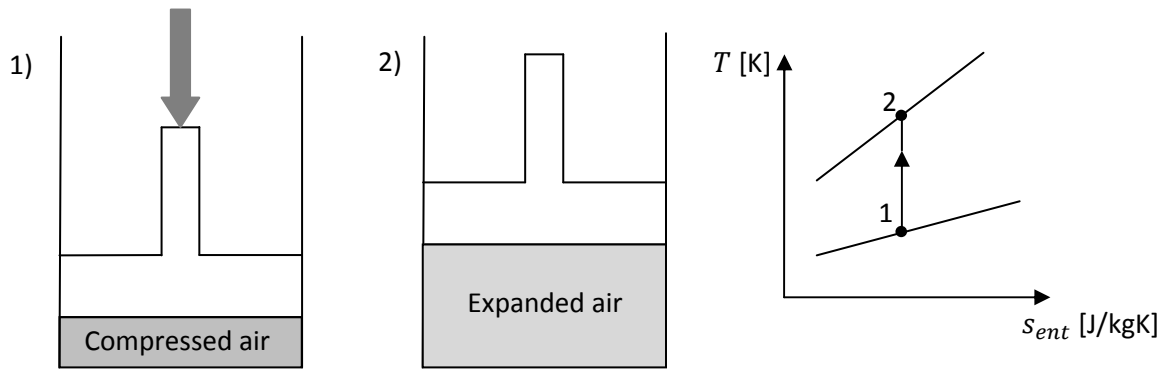
Figure 26: Isentropic expansion

The relation between the pressure and temperature during isentropic expansion is given by equation 25 (Çengel and Boles, 2001):

$$\frac{T_2}{T_1} = \left(\frac{P_2}{P_1}\right)^{(k-1)/k}$$

25

where k = 1.4 for air and 1.66 for helium. The temperature T_{RHVT} can now be calculated using equation 25 as

$$T_{RHVT} = T^* \left(\frac{P_{RHVT}}{P^*}\right)^{(k-1)/k} = 245 \times \left(\frac{101325}{351103}\right)^{(1.4-1)/1.4} = 171.78 \text{ K}$$

26

According to Etest (2008) the maximum temperature drop achievable with an inlet pressure of 7 bar (absolute) is 68.6 ˚C when the volume fraction μ_c is set to 0.2 (see Appendix D). The total temperature drop from the supply tube to the centre of the RHVT inner tube was calculated to be 122 ˚C by equations 19 and 26. This shows that the low temperature of the air in the central exiting orifice of the RHVT inner tube can easily be explained due to the cooling effect accompanying isentropic expansion.

Having accounted for the cooling of the inlet air, the heating of the inlet air is considered next. Consider the flow in the RHVT when the cold orifice is blocked, as illustrated in Figure 27. By blocking the cold orifice the inlet air $\dot{m}_i$ will then exhaust only through the

58

annular hot outlet and the flow within the cylindrical tube can be considered as one
control volume.
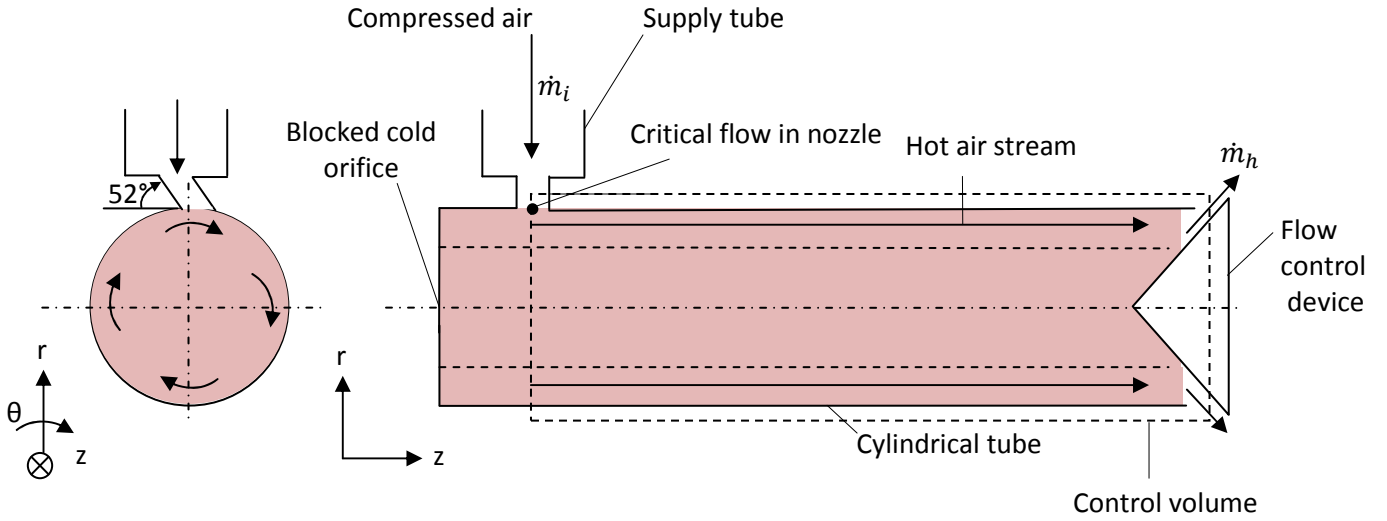
Figure 27: Flow in RHVT when cold outlet is blocked

Considering a steady state macroscopic energy balance for this control volume

$$\frac{dE_{tot}}{dt} = \dot{m}_i \left(h_i + \frac{V_i^2}{2} \right) - \dot{Q} - \dot{m}_h \left(h_h + \frac{V_h^2}{2} \right)$$

27

Assuming that $\dot{m}_i = \dot{m}_h$, $h = c_p T$ (c_p = constant), $V_h = \frac{\dot{m}_h}{\rho_h A_h}$, $\rho_h = \frac{P_h}{RT_h}$ and ignoring the
heat transfer $\dot{Q}$, equation 27 reduces to

$$0 = \dot{m}_i \left(c_p T_i + \frac{V_i^2}{2} \right) - \dot{m}_i \left[c_p T_h + \frac{1}{2} \left(\frac{\dot{m}_i}{A_h} \frac{\mathcal{R} T_h}{P_h} \right)^2 \right]$$

28

The temperature at the hot outlet T_h can be calculated by rearranging equation 28 to
form a standard quadratic equation

$$0 = \underbrace{\left[0.5 \left(\frac{\dot{m}_i}{A_h} \frac{\mathcal{R}}{P_h} \right)^2 \right]}_{a} T_h^2 + \underbrace{(c_p)}_{b} T_h - \underbrace{\left(\frac{V_i^2}{2} + c_p T_i \right)}_{c}$$

29

with a, b and c denoting the quadratic equation constants. For a choked inlet, as in the case of the inlet nozzles of the RHVT, the critical inlet values (calculated in control volume 1 of Figure 19) can be substituted into the inlet variables in equation 29 together with the assumption that $P_h = P_{atm}$ to obtain the following formulas for the quadratic equation constants a, b and c.

$$a = 0.5 \left(\frac{\dot{m}_{max}}{A_h} \frac{R}{P_{atm}} \right)^2 \qquad\qquad 30$$

$$b = c_p \qquad\qquad 31$$

$$c = -\left(\frac{V_i^2}{2} + c_p T^* \right) \qquad\qquad 32$$

The value of T_h can now be solved by calculating the roots of equation 29 with the quadratic formula

$$T_h = \frac{-b \pm \sqrt{b^2 - 4ac}}{2a}$$

The values shown in Table 8 were used to calculate the value of T_h for various hot outlet areas A_h over a range of inlet velocities V_i (from zero to sonic point (V^*)). These calculated values were plotted as shown in Figure 28.

Table 8: Critical inlet, geometric and boundary conditions for calculating the hot outlet temperature of the control volume of Figure 27

Variable	Symbol	Value
Inlet mass flow rate [kg/s]	$\dot{m}_{max}$	0.00146
Specific gas constant [J/kgK]	R	0.287
Hot outlet area [m^2]	A_h	4.23 x 10^{-6}, 4.33 x 10^{-6}, 4.42 x 10^{-6}
Hot outlet pressure [kPa]	P_{atm}	101.325
Inlet velocity [m/s]	V_i	$0 - 310$
Inlet temperature [K]	T^*	245
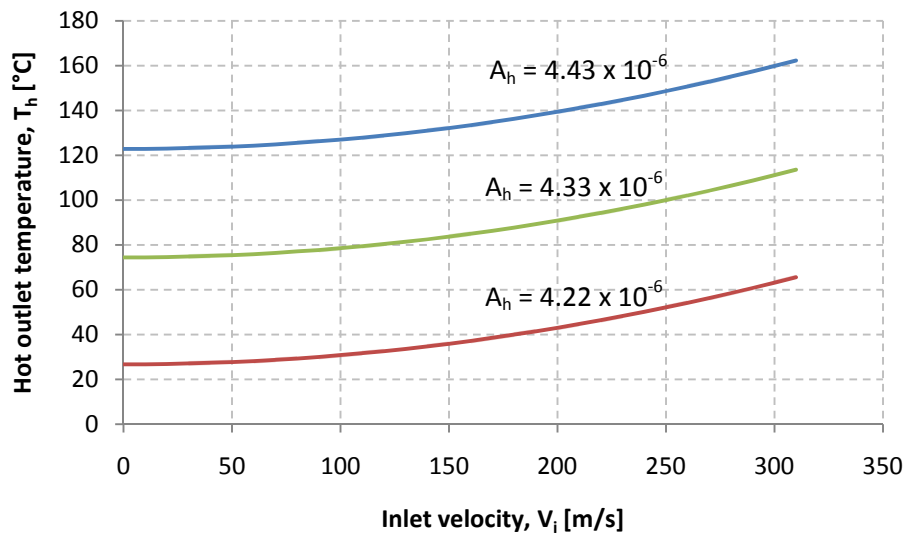
Figure 28: Hot outlet temperatures of the control volume in Figure 27 over a range of inlet velocities and for various hot outlet areas

From Figure 28 it is shown that very high temperatures are possible within the RHVT if the cold outlet is closed. It also shows that the hot outlet temperature T_h increases with an increase in the inlet velocity V_i and also with an increase in the hot outlet area A_h. If the cold outlet is opened, the flow within the RHVT will change as shown in Figure 29. When the cold outlet is unblocked, the flow from the inlet $\dot{m}_i$ will exhaust out of both the hot outlet and the cold outlet. There will also be flow from the inner cold stream to the hot outer stream $\dot{m}_{ch}$ due to expansion caused by the radial pressure gradient and there will also be flow from the hot stream to the cold stream $\dot{m}_{hc}$.

This mixing of the cold and hot air streams will further lower the hot stream temperature as well as raise the cold stream temperature by heat transfer which is why the temperature measured at the hot outlet is not as extremely hot as given in Figure 28 and why the cold outlet temperature is not as low as calculated using equation 26.
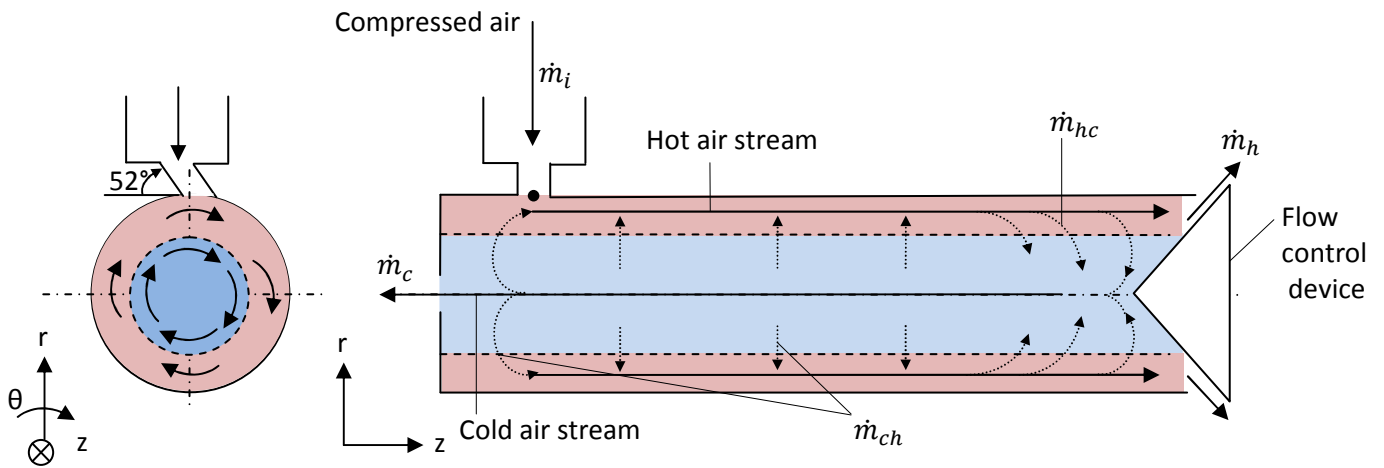
Figure 29: Mixing of the vortex streams in the RHVT when the cold outlet is unblocked

Now that it has been established by using a steady state macroscopic energy balance that very high temperatures can be achieved within the RHVT, further examination was done to determine the physical mechanism responsible for the heating of the inlet air. Control volume 3 (Figure 30) in Figure 19 represents the central flow region of the RHVT flow further down the length of the cylindrical tube and contains the two vortex streams; the hot outer stream and the cold inner stream.
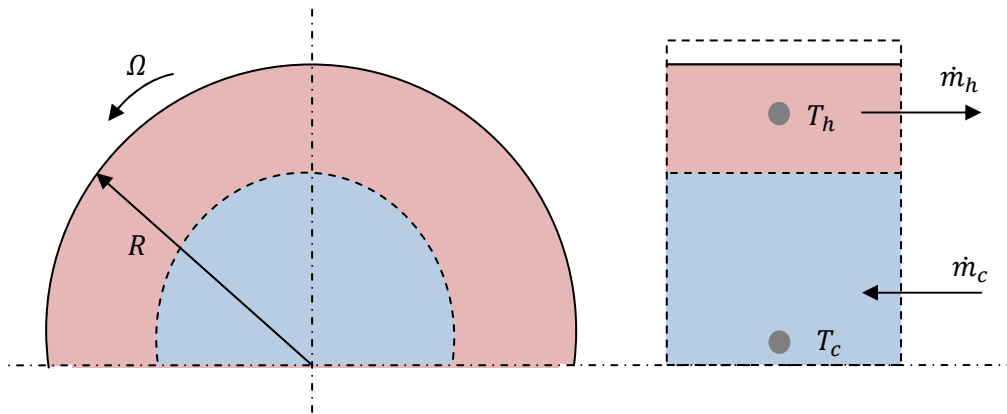
Figure 30: RHVT control volume 3 in Figure 19

The following assumptions about the control volume are then made:

⋯→ Steady state

⋯→ Turbulent flow

- ⇢ Compressible flow

- ⇢ v_z is zero

- ⇢ No pressure and temperature gradient in the θ - direction

- ⇢ Gravity is negligible

- ⇢ Viscous terms are significant and therefore can't be ignored

Applying the above made assumptions in Figure 30 to the conservation of energy equation in polar coordinates (Bird et al., 2002)

$$
\begin{aligned}
c_p \left(\frac{\partial(\rho T)}{\partial t} + v_r \frac{\partial(\rho T)}{\partial r} + \frac{v_\theta}{r} \frac{\partial(\rho T)}{\partial \theta} + v_z \frac{\partial(\rho T)}{\partial z} \right) \\
= k \left[\frac{1}{r} \frac{\partial}{\partial r} \left(r \frac{\partial T}{\partial r} \right) + \frac{1}{r^2} \frac{\partial^2 T}{\partial \theta^2} + \frac{\partial^2 T}{\partial z^2} \right] \\
+ 2 \left\{ \left(\frac{\partial \mu v_r}{\partial r} \right)^2 + \left[\frac{\mu}{r} \left(\frac{\partial v_\theta}{\partial \theta} + v_r \right) \right]^2 + \left(\frac{\partial \mu v_z}{\partial z} \right)^2 \right\} \\
+ \left\{ \left(\frac{\partial \mu v_\theta}{\partial z} + \frac{\mu}{r} \frac{\partial v_z}{\partial \theta} \right)^2 + \left(\frac{\partial \mu v_z}{\partial r} + \frac{\partial \mu v_r}{\partial z} \right)^2 \right. \\
\left. + \left[\frac{\mu}{r} \frac{\partial v_r}{\partial \theta} + r\mu \frac{\partial}{\partial r} \left(\frac{v_\theta}{r} \right) \right]^2 \right\}
\end{aligned}
$$

33

results in

$$
c_p v_r \frac{\partial(\rho T)}{\partial r} = \underbrace{k \frac{1}{r} \frac{d}{dr} \left(r \frac{dT}{dr} \right)}_{\text{Conduction } \dot{Q}_{cond}} + \underbrace{2 \left[\left(\frac{\partial \mu v_r}{\partial r} \right)^2 + \left(\frac{\mu}{r} v_r \right)^2 \right] + \left[\mu r \frac{d}{dr} \left(\frac{v_\theta}{r} \right) \right]^2}_{\text{Viscous heat generation } \dot{Q}_{gen}}
$$

34

The first term on the right-hand side of equation 34 is the conduction of heat in the radial direction of the flow. The second and third terms are viscous heat generation due to friction within the rotational flow caused by the change in radial velocity and the increase in effective viscosity (see Figure 21) towards the inner wall of the RHVT cylindrical tube. The effective viscosity is highest at the wall and therefore the viscous heat generation is also highest at the wall, which is why the air temperature is higher near the inner wall of the cylindrical tube. From these energy equation terms it is reasonable to propose that the heating of the outer vortex air stream is due to viscous

heating and that the viscosity of the fluid plays an integral role of ensuring that the heat generation through viscous heating in the outer vortex stream is larger than the heat transfer due to conduction.

Another physical mechanism that could also contribute to the heating of the outer stream is isentropic compression. Considering the pressure distribution within the RHVT flow (Figure 23), it is shown that the radial pressure increases from the centre of the flow towards the wall of the RHVT. This increase in pressure compresses the air in the outer stream, which in turn then heats the air (see equation 25).

In conclusion it is proposed that the "temperature separation" in the RHVT is due to the following. The inlet air is initially cooled due to isentropic expansion through the inlet nozzles, and further cooling occurs within the cylindrical tube of the RHVT due to isentropic expansion caused by the pressure gradient created by the generated rotational flow within the RHVT. It was established through a macroscopic energy balance that immense heating of the inlet air will occur if the cold outlet is blocked and that the temperatures will decrease when the cold outlet in unblocked due to mixing of the two air streams. It was further determined that the best explanation of this heating of the inlet air is due to viscous heating at the wall of the RHVT and possibly to isentropic compression. These proposed cooling and heating mechanisms of the inlet air will further be investigated in the numerical simulation (see Appendix C).

5.1.2 Mass Separation

The experimental work showed that the RHVT has a dust separation efficiency of greater than 85 %. This shows that more than 85 % of the graphite dust particles injected into the RHVT exit through the outer annular opening of the hot outlet and that the graphite particles tend to move towards the wall of the RHVT. It was decided to analytically model the paths of the graphite particles to see how the particles move within the rotational flow of the RHVT.

The following equation of motion (momentum) was used by Maxey and Riley (1983) to model the motion of a small inertial particle in a steady, axisymmetric rotational Couette flow (similar to Figure 20):

$$
\begin{aligned}
m_p \frac{d\bar{V}_p}{dt} = & \, m_f \frac{D\bar{V}_f}{Dt} - \frac{1}{2}m_f \left\{ \frac{d\bar{V}_p}{dt} - \frac{D}{Dt}\left(\bar{V}_f + \frac{1}{10}r_p{}^2 \nabla^2 \bar{V}_f\right) \right\} + (m_p - m_f)g \\
& - 6\pi r_p \mu_f \int_0^t K(t-\tau,\tau)\frac{d}{d\tau}\left(\bar{V}_p - \bar{V}_f - \frac{1}{6}r_p{}^2 \nabla^2 \bar{V}_f\right)d\tau \\
& - 6\pi r_p \mu_f \left(\bar{V}_p - \bar{V}_f - \frac{1}{6}r_p{}^2 \nabla^2 \bar{V}_f\right) \\
& + 6.46 r_p{}^2 \rho_f \sqrt{\frac{\nu_f}{|\omega_f|}}\,(\bar{V}_p - \bar{V}_f) \times \omega_f = F
\end{aligned}
$$

35

The term on the left hand side of the equation represents the inertia of the particles. The terms on the right hand side are, from left to right, the pressure gradient force (of the flow field), the added mass force (related to the necessity of moving a mass of fluid when a particle displaces it), buoyancy force, Basset history force (determines the initial motion of a particle starting from rest), Stokes drag force and finally the Saffman shear induced lift force. The terms involving $\nabla^2 \bar{V}_f$ are termed the Faxén corrections (Henderson et al., 2007) and these terms take the curvature in the velocity field of the fluid into account. In computing the Basset history force, the kernel $K(t-\tau)$ as proposed by Mei and Adrian (1992) was used and is calculated as

$$
K(t-\varphi) = \left\{ \left[\frac{\pi(t-\varphi)\mu_f}{r_p{}^2}\right]^{1/4} + \left[\frac{\pi}{2}\frac{|\bar{V}_f - \bar{V}_p|^3}{r_p \mu_f f_h(Re_p)}(t-\varphi)^2\right]^{1/2} \right\}^{-2}
$$

36

with

$$
f_{hist} = 0.75 + 0.105 Re_p(\varphi)
$$

37

To determine the path of the graphite particles, using equation 35, in the rotational flow of the RHVT, as calculated using equation 16, the following assumptions are made:

⇢ Particles do not affect the flow field
⇢ Particles do not interact with each other

- Particles are modelled as spheres
- Particle movement is only in the r- and θ-direction (due to the direction of the calculated rotational flow field)
- Wall effects are ignored
- Gravity is negligible
- Particle starts moving at a given/specified velocity

Equation 35 can now be simplified by taking the aforementioned assumptions into account. Firstly the added mass force can be neglected due to the assumption that the particles do not affect the flow field. Secondly the buoyancy force is ignored due to the negligible gravity assumption. Thirdly both the Saffman shear force and the Faxén correction factors are neglected since they are only significant when the particle moves close to a wall, and for this problem wall effects are ignored. Lastly the Basset history force is also ignored because it determines the immediate position of a particle when it starts from rest and in this problem it is assumed that the particle starts with an initial velocity and position. Since the flow field is in the tangential θ-direction, there will be a centrifugal force acting upon the particle due to the angular velocity generated by this flow field. This force, however, was embedded in the neglected forces and it was therefore added, in its most simple form (equation 38) to equation 35.

$$F_{ctf} = m_p r \Omega_o{}^2 \qquad\qquad 38$$

After cancelling out the neglected terms in equation 35 and adding the centrifugal force F_{ctf}, the forces acting upon the particle are found to be the pressure gradient force $m_f \frac{D\bar{V}_f}{Dt}$ due to the flow field velocity $\bar{V}_f$, the drag force F_d acting in the opposite direction to the relative velocity ($\bar{V}_{rel} = \bar{V}_f - \bar{V}_p$) and the centrifugal force as shown in Figure 31.
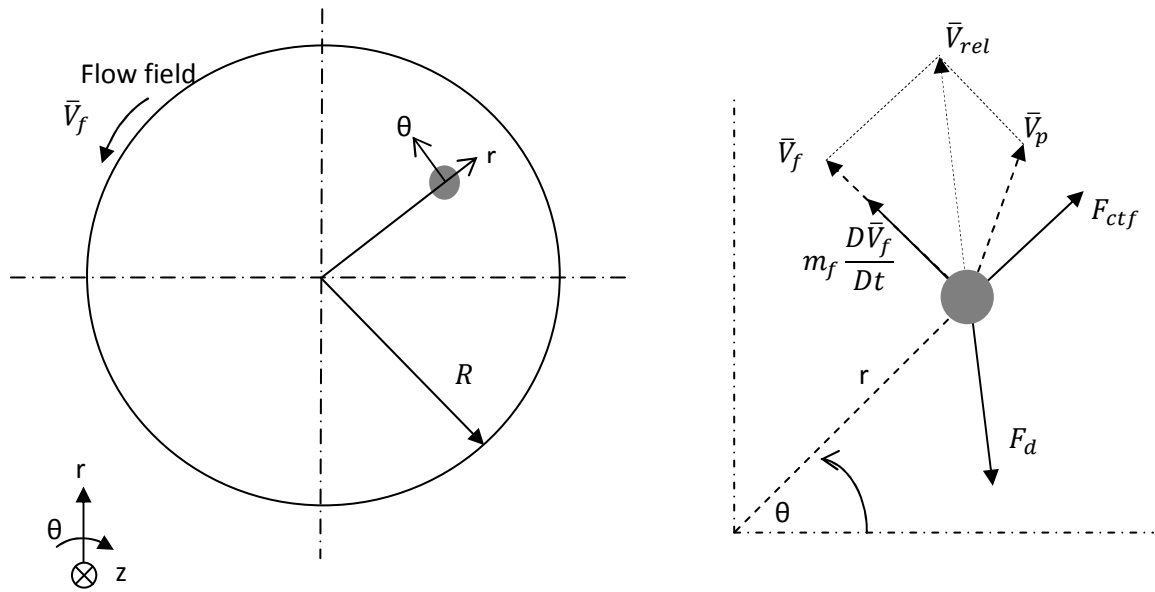
Figure 31: Particle motion in a simplified RHVT control volume

The motion of the graphite particle can therefore be described by equation 39:

$$m_p \frac{d\bar{V}_p}{dt} = m_f \frac{D\bar{V}_f}{Dt} - 6\pi r_p \mu_f \left(\bar{V}_p - \bar{V}_f \right) + m_p r \Omega^2 \qquad\qquad 39$$

Dividing equation 39 by m_p and considering only the r- and θ-components of the particle velocity $\bar{V}_p = \left(V_{p,r}, V_{p,\theta} \right)$ and the flow field $\bar{V}_f = \left(0, V_{f,\theta} \right)$, the velocity components of the graphite particle are:

$$\frac{dV_{p,r}}{dt} = - \frac{6\pi r_p \mu_f}{m_p} \left(V_{p,r} \right) + r\Omega^2 \qquad\qquad 40$$

$$\frac{dV_{p,\theta}}{dt} = \frac{m_f}{m_p} \frac{d}{dt} V_{f,\theta} - \frac{6\pi r_p \mu_f}{m_p} \left(V_{p,\theta} - V_{f,\theta} \right) + r\Omega^2 \qquad\qquad 41$$

The variable m_f represents the mass of the fluid displaced by the particle. If it is assumed that the particle displaces its own volume as it moves through the fluid, the volume of the displaced fluid is equal to the volume of the particle, $Vol_f = Vol_p$. Therefore, since $m = \rho Vol$, the first term on the right hand side of equation 41 reduces to

$$\frac{m_f}{m_p}\frac{d}{dt}V_{f,\theta} = \frac{\rho_f Vol_f}{\rho_p Vol_p}\frac{d}{dt}V_{f,\theta} = \frac{\rho_f Vol_p}{\rho_p Vol_p}\frac{d}{dt}V_{f,\theta} = \frac{\rho_f}{\rho_p}\frac{d}{dt}V_{f,\theta} \qquad 42$$

The velocity components are then calculated using an explicit numerical method with time steps dt of 0.1 µs as

$$V_{p,r}{}^{(n+1)} = -\left(\frac{6\pi s_r{}^n \mu_f}{m_p}\left(V_{p,r}{}^n\right) + s_r{}^n \Omega^2\right)dt \qquad 43$$

$$V_{p,\theta}{}^{(n+1)} = \frac{\rho_f}{\rho_p}V_{f,\theta}{}^n - \left(\frac{6\pi s_r{}^n \mu_f}{m_p}\left(V_{p,\theta}{}^n - V_{f,\theta}{}^n\right) + s_r{}^n \Omega^2\right)dt \qquad 44$$

where the superscript n denotes the initial velocity components (or the velocity components calculated at the previous time step) and $(n + 1)$ denotes the velocity components to be calculated at the next time step, s_r is the r-component of the particle position (see equation 46) and the flow field velocity $V_{f,\theta}$ is calculated using equation 16.

The position of the graphite particle can be calculated for each time step by using the equation:

$$s = Vt \qquad 45$$

The explicit numerical equations to determine the particle position in r- and θ-coordinates are thus:

$$s_r{}^{(n+1)} = s_r{}^n + V_{p,r}{}^{(n+1)}dt \qquad 46$$

$$s_\theta{}^{(n+1)} = s_\theta{}^n + V_{p,\theta}{}^{(n+1)}dt \qquad 47$$

In the above calculations the assumption was made that the particles do not affect the background flow and do not interact with each other. This assumption in only valid if the particle Reynolds number (equation 48) is smaller than 1

$$Re_p = \frac{2r_p|\bar{V}_p - \bar{V}_f|}{\rho_f \mu_f} \ll 1 \qquad 48$$

The particle Reynolds number is dependent on the particle radius r_p, and was thus calculated for different particle diameters. Inserting the appropriate values for fluid density ρ_f, fluid viscosity μ_f and relative velocity $|\bar{V}_p - \bar{V}_f|$ into equation 48 and calculating for particle radii r_p of 0.25 µm, 0.35 µm and 0.5 µm, the following results were obtained at the maximum relative velocity $|\bar{V}_p - \bar{V}_f|$ for each particle radius.

Table 9: Particle Reynolds numbers for different particle radii

Particle radius, r_p [µm]	Particle Reynolds number in air, Re_{p_air}	Particle Reynolds number in helium, Re_{p_helium}
0.25	0.095	0.061
0.35	0.342	0.231
0.5	1.505	1.110

These calculated particle Reynolds numbers show that, according to equation 48, equation 35 is really only valid for particles with diameters less van 1 µm in both air and helium as the fluid. The particles used in the experimental work are bigger than 1 µm but the graphite particles found in the AVR (Bäumer, 1990) are approximately 0.76 µm in diameter, therefore this equation would be an adequate representation of the AVR graphite particle paths in the RHVT.

A graphite particle may now be tracked (using equations 46 and 47) from a number of initial positions and initial velocities in both air and helium. The tracked particle paths are shown in Figure 32 and Figure 33 with the values for the fluid and graphite properties and initial conditions as shown in Table 10.

Table 10: Graphite particle parameters and initial conditions

Variable	Symbol	Value
Flow domain constant	a	1
Flow domain constant	b	0.5
Fluid density air [kg/m^3]	ρ_{f_air}	7.95
Fluid density helium [kg/m^3]	ρ_{f_helium}	1.098
Particle density [kg/m^3]	ρ_p	2238

Particle diameter [μm]	r_p	0.2, 0.35, 0.5
Fluid viscosity [kg/ms]	μ_f	15.1 x 10^{-6}
Angular velocity [rad/s]	Ω	55338
Initial particle velocity vector [m/s]	$\bar{V}_p = \left(V_{p,r}, V_{p,\theta}\right)$	$(0, V_{f,\theta})$
Initial particle position vector [m, rad]	$\bar{s} = (s_r, s_\theta)$	(0.000635 , 0)
Time step [s]	t	0.1 x 10^{-6}
Total time [s]	t_{tot}	78 x 10^{-6}

From Figure 32 and Figure 33 it is shown that the particles tend to move towards the wall of the flow domain. These particles were tracked over a total time of 78 μs and in this time it can be seen from Figure 32 and Figure 33 that the heavier particles (those with larger particle diameters) have moved closer to the wall than the lighter particles. This shows that the heavier particles will move outwards towards the wall of the flow domain in less time than the lighter particles. This particle movement is attributed to the increased centrifugal force acting upon the larger graphite dust particles; reminiscent of the well-known milk/cream separator. From these results it is confirmed that the particles will tend to move outwards toward the wall of the flow domain which is why the graphite particles tend to exhaust from the outer annular opening of the hot outlet of the RHVT.
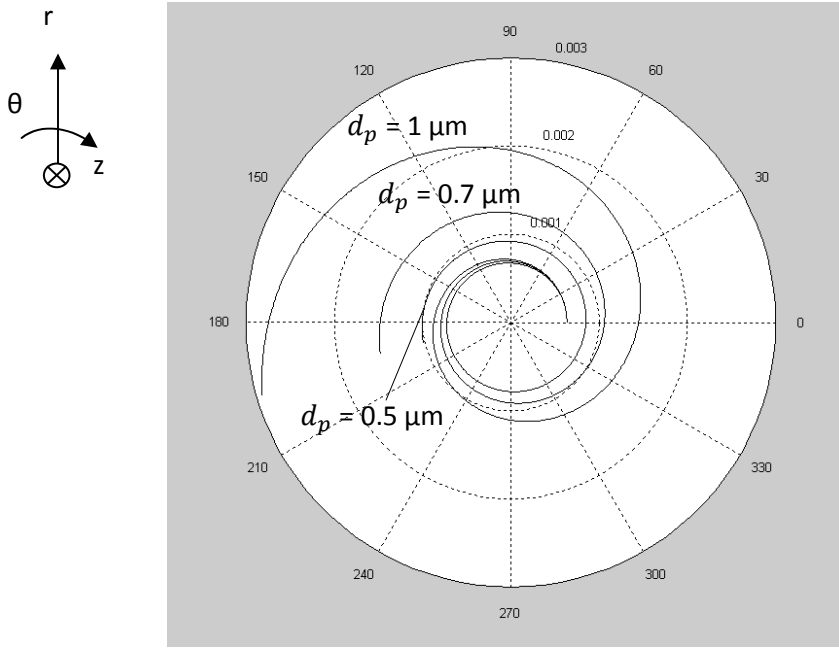
Figure 32: Graphite particle paths for different particle diameters, in a r-θ plane for air given the initial velocity of [0,78.57] and position of [0.000635,0] over 78 μs
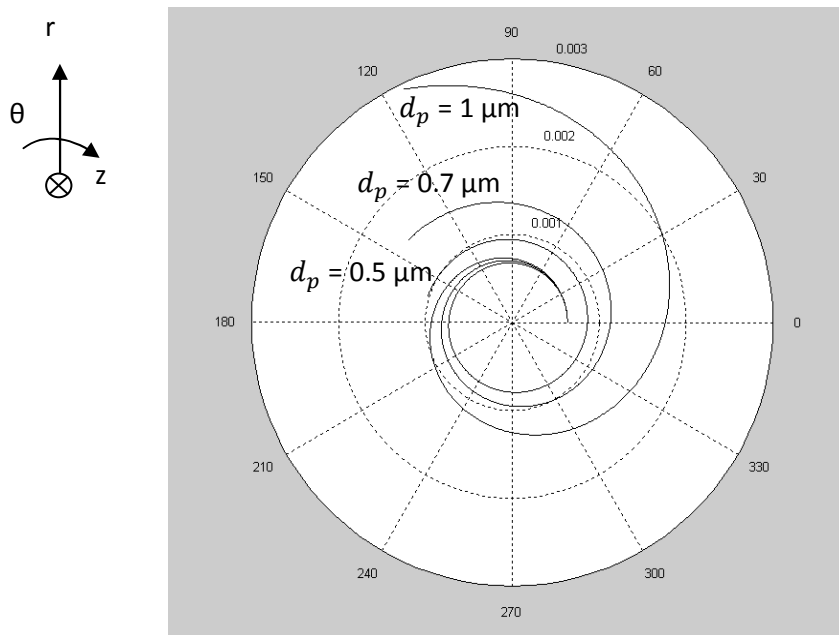
Figure 33: Graphite particle paths for different particle diameters, in a r-θ plane for helium given the initial velocity of [0,78.57] and position of [0.000635,0] over 78 μs

5.2 Numerical Analysis

An analytical model as to how the temperature and mass separation mechanism inside the RHVT works was proposed in section 5.1. To further understand the flow within the RHVT on a microscopic scale, a Computational Fluid Dynamics (CFD) simulation was done to see how well the numerical results correlate with the analytical and experimental results. Many difficulties arose during the numerical simulation, however, and the solution did not converge. The obtained results therefore cannot be accurately compared to the analytical results.

Each stage of the CFD simulation process is discussed in Appendix C and a brief comparison is given between the analytical model results and the preliminary CFD results.

6. DISCUSSION, CONCLUSIONS AND RECOMMENDATIONS

One of the main focus points of the PBMR project is safety and therefore all safety issues inherent to the AVR have to be addressed before its technology can be used in the PBMR. It has been found in the AVR that the radioactive silver $_{44}Ag^{110}$ isotope diffuses through apparently intact TRISO fuel particles and that these isotopes bond to graphite dust, generated by friction between the fuel spheres (MacLean and Ballinger, 2004). The silver $_{44}Ag^{110}$ is then transported by the graphite dust through the primary helium coolant loop of the reactor (Bäumer, 1990). A way therefore has to be found to separate the graphite dust, and thus the radioactive silver $_{44}Ag^{110}$ isotopes, from the helium coolant stream. The RHVT was chosen to be investigated for this purpose and an evaluation of other particle separation techniques showed that the RHVT has the potential to be used for this application next to the gas centrifuge and the centrifugal dust collector. The gas centrifuge has a higher energy consumption than the RHVT and it is next to impossible to procure one for testing because they are not available commercially to non-corporate companies for fear of nuclear proliferation. The RHVT also has the possible advantage over the centrifugal dust collector in that it has the potential to separate particles smaller than 1 μm in diameter whereas the dust collector's efficiency to separate these small size particles are low. The RHVT also has the added bonus of being able to heat and cool helium/air.

The next objective of this project was to investigate dust separation capabilities of the RHVT. Firstly an experimental apparatus was designed that was capable of supplying compressed air to the RHVT, injecting graphite dust upstream of the RHVT, collecting the graphite dust from the RHVT outlets and measure the different operating conditions. This experimental apparatus contains two items which had to be specifically designed for this application. These items are the dust mixing chamber and the dust collectors. The dust mixing chamber was designed to inject graphite dust in small quantities into the main fluid stream. The injection of the dust is due to a pressure gradient across the inlet and outlet of the chamber. This method proved to be very effective and gave minimal resistance to the flow. Its only drawback was that the amount of dust injected into the system could not be controlled, which resulted in

different amounts of dust being injected into the RHVT for the same operating and geometric conditions. Although the exact amount of dust injected into the air/helium stream could not be controlled, it could still be measured accurately and thus did not create any problems with the experimental results. The dust collectors were designed to collect the dust exhausting from the RHVT outlets. These collectors worked very effectively except at very high flow rates when it started leaking dust. It was therefore decided to add a rubber gasket between the perforated base and the cone distributor to act as a seal at high volumetric flow rates, which solved the problem. Another problem that arose was that the cellulose nitrate membrane filters (with filtration grade 0.65 μm) that were used to collect the VF grade graphite dust are only available in 47 mm diameter filters. Since the dust collectors are 90 mm in diameter, it was decided to arrange the membrane filters in a clover shape over a normal paper filter (Munktell AB) to capture the smaller graphite particles that pass through the normal paper filter. This filter paper arrangement captured all the dust particles successfully and caused no extra pressure loss across the dust collectors.

 The dust separation efficiency of the RHVT was therefore tested using the experimental apparatus for various operating and geometric conditions. The RHVT was tested in both air and helium, for various inlet volumetric flow rates, different volume fractions, RHVT geometries and different graphite dust particle sizes. These conditions were monitored throughout each experiment with calibrated sensors. The experimental results showed a dust separation efficiency of more than 85 % and a maximum of 96 % which makes the RHVT a relatively good mass separator in comparison with other well known mass separators such as the gas centrifuge and the centrifugal dust collector. The experimental results also showed that the inlet volumetric flow rate and RHVT geometry had the largest influence on the dust separation efficiency. It was also shown that the efficiency decreased when the smaller dust particles were used, but not significantly. The results also showed that there was not a significant change in the efficiency between the air and helium tests. The temperature measurements made during the experimental tests confirmed the RHVT outlet temperature's dependence on the volume fraction and that a higher temperature difference between the inlet and outlet temperatures is obtained for higher inlet volumetric flow rates.

A regression analysis was done on the experimental data points to find a correlation between the various parameters and the dust separation efficiency. This objective was achieved by testing different curve fits to determine which curve best fitted the data. It was shown from the results that a power curve fit best predicted the efficiency with a percentage error of only 2.77 %. It was shown, however, that all the curve fits had very poor R^2 - values and that their percentage error was all in the range of 2.8 %. It was also confirmed that inlet volumetric flow rate and the RHVT geometry have the greatest influence on the dust separation efficiency. The power curve (equation 5) obtained with the regression analysis can now be used to determine the dust separation efficiency of the RHVT under different operating or geometric conditions such as in the PBMR environment.

An analytical analysis was done to determine a simple explanation as to how the temperature separation and mass separation occurs within the RHVT. The proposed analytical model gives a basic understanding of what thermo-physical mechanisms are responsible for the cooling and heating of the inlet air. The model, however, does fall short in calculating or predicting the exact velocity, pressure and outlet temperatures due to the simplification of the flow in the RHVT, lack of experimental data on the flow inside the RHVT and the lack of an appropriate analytical turbulence model.

Due to the simplification of the analytical model it was decided to also do a CFD model to see how well the simplified model compares to an accurate numerical model that incorporates turbulence and wall effects. The CFD simulation, however, posed a lot of difficulties. Firstly difficulties were experienced in measuring the geometry of the RHVT. It was found that the geometry of the inlet nozzles in the vortex generator is a key geometric feature that had to be modelled accurately in the computation mesh. Due to its small size the nozzles could not be measured with a conventional Vernier calliper and other methods had to be investigated. This problem was solved by taking photographs of the vortex generator and then importing it into CAD where the dimensions of the nozzles could be determined more accurately. Another difficulty was faced in that the size of the hot outlet could not be measured. This was also due to its small size and the

fact that it is obstructed by the flow control device. The area of the hot outlet determines the volume fraction of the RHVT and because the hot outlet area could not be modelled accurately in the computational mesh a user-defined function (UDF) had to be written to instead control the pressures at the outlet to achieve the desired volume fraction.

It was also found that due to the high turbulence of the flow at the entrance region of the RHVT the solution diverged if the full mass flow rate condition was applied to the mass flow inlet boundary. Therefore the UDF was further appended to make provision for incrementally increasing the mass flow rate from 10 % to 100 % over a number of iterations so that a solution can be calculated. Further it was found that the solution is grid dependent which means the mesh had to be refined for the solution to converge. It was found, however, that after a number of refinements the computer on which the simulations were run did not have enough memory to run the numerical simulation any further due to the large number of cells. To overcome this problem the simulation was run on the University computer cluster, but it was found that the mesh could not be refined as precisely for both gradients of velocity and temperature and therefore gave even less accurate results than the first simulation. Due to the fact that the solution did not converge, the results obtained could not be compared to the analytical model, nevertheless a brief comparison between the preliminary numerical results and analytical model is shown in Appendix C.

Although the experimental results showed that the RHVT is a very efficient mass separator a way has to be devised to implement it into the PBMR. The RHVT cannot be inserted in the primary coolant loop as it would cause too much resistance to the flow and therefore it would have to be inserted in parallel. Some of the helium from the primary coolant loop can be tapped off into a smaller parallel loop that contains a RHVT or cascade of RHVTs. The helium would then pass through the RHVTs and the purified helium would then be injected back into the primary coolant loop. The effect of this parallel loop on the helium coolant flow and plant efficiency would have to be investigated further and other possible ways to implement the RHVT into the PBMR should also be explored. Another factor that has to be taken into consideration is the

size of the RHVT, which would have to be rather large to accommodate the very high pressure and velocity of the helium coolant and the structural material used to manufacture the RHVT due to the very high temperatures of the helium flow in the primary loop of the reactor.

It was also considered that the RHVT can also be used in the PBMR merely as a gas cooler or heater, because it requires no external energy source and only requires compressed gas to function, which is already available in the coolant loop of the PBMR. The experimental tests proved that the RHVT also works with helium. This makes it a very lucrative option to be implemented in the RHVT, especially for further heating the helium process gas.

Recommendations for further work are that a RHVT mass separation system should be designed that can be incorporated into the primary loop of the PBMR reactor; also that an in-depth CFD analysis must be done to obtain a better understanding of the detailed temperature separation, flow regime and mass separation inside the RHVT. The idea of implementing the RHVT as a gas heater should also be investigated further because it could be very beneficial for the PBMR project by heating the process gas without consuming any energy.

REFERENCES

AFROX, 2000. *Specification for pure gasses and gas mixtures which are classified as "special gasses"*. Product specification.

Ahlborn, B. and Gordon, J.M., 2000. The Vortex Tube as a Classic Thermodynamic Refrigeration Cycle. *Journal of Applied Physics*, 88(6), pp.3645-53.

Ahlborn, B. and Groves, S., 1997. Secondary Flow in a Vortex Tube. *Fluid Dynamics Research*, 21, pp.73-86.

Akhesmah, S., Pourmahmoud, N. & Sedgi, H., 2008. Numerical Study of the Temperature Separation in the Ranque-Hilsch Vortex Tube. *American Journal of Engineering and Applied Sciences*, 1(3), pp.181 - 187.

Anon., 2008. *Gas Centrifuge Process*. [Online] Available at:
http://www.euronuclear.org/info/encyclopedia/g/gascentrifuge [Accessed 15 July 2008].

ANSYS FLUENT, 2006. *Flow Modelling Software*. [Online] (6.3.26).

ANSYS GAMBIT, 2006. *Flow modelling software*. [Online] (2.4.6).

Arbuzov, V.A., Dubnizhchev, Y.N., Lebedev, A.V., Pravdina, M.K. & Yavorskii, N.I., 1997. Observation of Large Scale Hydrodynamic Structures in a Vortec Tube and the Ranque Effect. *Tech. Phys. Lett.*, 23(12), pp.938-40.

Baker, P.S. and Rathkamp, W.R., 1954. *Investigations on the Ranque-Hilsch (Vortex) Tube*. Technical. Tennessee: Oak Ridge National Laboratory.

Bäumer, R., 1990. *AVR:Experimental High Temperature Reactor;21 Years of Successful Operation for a Future Energy Technology*. Düsseldorf: Association of German Engineers (VDI).

Behera, U., Paul, P.J., Dinesh, K. & Jacob, S., 2007. Numerical Investigations on Flow Behaviour and Energy Separation in Ranque-Hilsch Vortex Tube. *International Journal of Heat and Mass Transfer*, 51(25-26), pp.6077-89.

Bird, R.B., Curtiss, C.F. & Stewart, W.E., 1959. Tangentail Newtonian Flow in Annuli - II. *Chemical Engineering Science*, 11, pp.114 - 117.

Bird, R.B., Stewart, W.E. & Lightfoot, E.N., 2002. *Transport Phenomena*. 2nd ed. New York: Wiley & Sons Inc.

British Standards Institution, 1981. BS 1042: Section 1.1 *Fluid flow in closed conduits*. BSI.

Çengel, Y.A. and Boles, M.A., 2001. *Thermodynamics: An Engineering Approach*. New York: McGraw-Hill.

Cockreill, T., 1995. *Ranque-Hilsch Vortex Tube*. M.S Thesis. Cambridge University.

De Wolf Smyth, H., 1945. *The Electromagnetic Method and Its Limitations*. [Online] Available at: http://www.atomicarchive.com/Docs/SmythReport/smyth_ix-b.shtml [Accessed 15 July 2008].

Deissler, R.G. and Perlmutter, M., 1960. Analysis of the Flow and Energy Separation in a Vortex Tube. *International Journal of Heat and Mass Transfer*, 1, pp.173-91.

Eckert, E.R.G. and Hartnett, J.P., 1957. Experimental Study of the Velocity and Temperature Distribution in a High-Velocity Vortex-Type Flow. *Journal of Heat Transfer*, 79, pp.751-58.

Eiamsa-ard, S. and Promvonge, P., 2007. Numerical Investigation of the Thermal Separation in a Ranque-Hilsch Vortex Tube. *International Journal of Heat and Mass Transfer*, 50, pp.821-32.

Eiamsa-ard, S. and Promvonge, P., 2008. Numerical Simulation of Flow Field and Temperature Separation in a Vortex Tube. *International Communications in Heat and Mass Transfer*, 35, pp.937-47.

Etest, 2008. *Vortex Tubes*. [Online] Available at: http://etest.exair.com/spotcooling/vtpage.php [Accessed 31 July 2009].

FESTO, 2008. *Product Catalogue*. [Online] Available at: http://www.festo.com/pnf/en-us_us/products/catalog [Accessed 15 September 2008].

Figliola, R.S. and Beasley, D.E., 2006. *Theory and Design for Mechanical Measuremetns*. 4th ed. USA: Wiley.

Gao, C.M., Bosschaart, K.J., Zeegers, J.C.H. & de Waele, A.T.A.M., 2005. Experimental Study on a Simple Ranque-Hilsch Vortex Tube. *Cryogenics*, 45, pp.173-83.

Gee, D., 2002. *The Pebble Bed Modular Reactor*. [Online] Available at: http://www.eas.asu.edu/~holbert/eee460/dfg/index.html [Accessed 12 January 2009].

Graphit Krofpmühl AG, 2008. *Graphit Kropfmühl AG*. [Online] Available at: http://www.graphite.de/englisch/index.php [Accessed 12 May 2009].

Hargrove, S., n.d. *Laser Technology follows in Lawrence's footsteps*. [Online] Available at: http://www.llnl.gov/str/Hargrove.html [Accessed 15 July 2008].

Henderson, K.L., Gwynllyw, D.R. & Barenghi, C.F., 2007. Particle Tracking in Taylor-Couette Flow. *European Journal of Mechanics*, 26, pp.738 - 748.

Hilsch, R., 1947. The Use of the Expansion of Gasses in a Centrifugal Field as Cooling Process. *Rev. Sci. Instrum.*, 18(2), pp.108-13.

Hoppe, K.G., Strachan, P.J. & Thiart, G.D., n.d. *Experimental Techniques 414*. Stellenbosch University.

Kap-Jong, R., Jung-soo, K. & In-Su, C., 2004. Experimental Investigation on Dust Separation Characteristics of a Vortex Tube. *JSME International Journal*, 47(1), pp.29 - 36.

Kassner, R. and Knoernschild, E., 1948. *Friction laws and energy transport in circular flow*. Technical Report F-TR-2198ND. Ohio: Wright-Patterson Air Force Base.

Kulkarni, M.R. and Sardesai, C.R., 2002. Enrichment of Methane Concentration via Separation of Gases using Vortex Tubes. *Journal of Energy Engineering*, 128(1), pp.1-12.

Lewellen, W.S., 1964. *Three-Dimensional Viscous Vortices in Incompressible Flow*. PhD Thesis. University of California.

Lewins, J. and Benjan, A., 1999. Vortex Optimization Theory. *Energy Journal*, 24, pp.931-43.

Linderstrom-Lang, C.U., 1964. Gas Separation in the Ranque-Hilsch Vortex Tube. *International Journa of Heat and Mass Transfer*, 7, pp.1195-206.

Linderstrom-Lang, C.U., 1971. The Three-Dimensional Distributions of Tangential Velocity and Total-Temperature in Vortex Tubes. *Journal of Fluid Mechanics*, 45, pp.161-87.

MacLean, H.J. and Ballinger, R.G., 2004. Silver Ion Implantation and Annealing in CVD Silicon Carbide: The Effect of Temperature on Silver Migration. In *2nd International Topical Meeting on High Temperature Reactor Technology*. Beijing, 2004.

Marshall, J., 1977. Effect of Operating Conditions, Physical Size and Fluid Characteristics on the Gas Separation Performance of the Linderstrom-Lang Vortex Tube. *International Journal of Heat and Mass Transfer*, 20, pp.227-31.

Matzner, D., 2004. PBMR Project Status and the Way Ahead. In *2nd International Topical Meeting on High Temperature Reactor Technology*. Beijing, 2004.

Matzner, D., 2004. PBMR project status and the way ahead. In *2nd International Topical Meeting on High Temperature Reactor Technology*. Beijing, 2004.

Maxey, M.R. and Riley, J.J., 1983. Equation of Motion for a Small Rigid Sphere in a Non-Uniform Rotational Flow. *Physics of Fluids*, 26, pp.883 - 889.

Mechanical and Mechatronic Department, 2009. *Laboratory Safety Procedures*.

Mei, R. and Adrian, R.J., 1992. Flow Past a Sphere with an Oscillation in the Free-Stream Velocity and Unsteady Drag at Finite Reynolds Numbers. *Journal of Fluid Mechanics*, (273), pp.323-41.

Meriam, J.L. and Kraige, L.G., 2003. *Engineering mechanics: Dynamics*. New Jersey: John Wiley & Sons, Inc.

Mills, A.F., 1999. *Heat Transfer*. 2nd ed. New Jersey: Prentice Hall.

Morsi, Y.S.M. and Clayton, B.R., 1984. Determination of Principal Charateristics of Turbulent Swirling Flow along Annuli. *International Journal of Heat and Fluid Flow*, 5(4), pp.195 - 203.

Nederlandse Kalibratie Organisatie, 1991. *Direct comparison with primary water manometer type SSM 2*3000*. NKO.

NESCA, 2009. *Flosep*. [Online] Available at: http://www.necsa.co.za/Products-and-Services/Engineering/Flosep-414.aspx [Accessed 12 June 2009].

Nicholls, D.R., 2002. The Pebble Bed Modular Reactor. *South African Journal of Science*, 98.

Oliver, R., 2008. *Numerical Prediction of Primary and Secondary Flows in a Ranque-Hilsch Vortex Tube*. MSc Thesis. Dublin Institute of Technology.

Perry, R.H. and Green, D.W., 1997. *Perry's Chemical Engineer's Handbook*. USA: McGraw - Hill.

Pike, J., 2005. *Enrichment Techniques*. [Online] Available at: http://www.globalsecurity.org/wmd/intro/u-enrichment.htm [Accessed 14 July 2008].

Piralishvili, S.A. and Polyaev, V.M., 1996. Flow and Thermodynamic Characteristics of Energy Separation in a Double-Circuit Vortex Tube- An Experimental Investigation. *Experimental Thermal and Fluid Science*, 12, pp.399-410.

Promvonge, P. and Eiamsa-ard, S., 2005. Investigation on the Vortex Thermal Separation in a Vortex Tube Refrigerator. *ScienceAsia*, 31(3), pp.215-23.

Promvonge, P. and Eiamsa-ard, S., 2008. Review of Ranque-Hilsch Effects in Vortex Tubes. *Renewable and Sustainable Energy Reviews*, 12(7), pp.1822-42.

Ranque, G., 1933. Experiences Sur la detente avec production simultanees dun schappement dair chaud et dun echappement dair froid. *Journal Physique et de Radium*, 7(4), pp.112-15.

Reynolds, A.J., 1961. Energy Flows in a Vortex Tube. *Journal of Applied Mathematical Physics*, 12, p.343.

Shannak, B.A., 2004. Temperature Separation and Friction Losses in a Vortex Tube. *Journal of Heat and Mass Transfer*, 40, pp.779-85.

Singh, P.K., Tatghir, R.G., Gangacharyulu, D. & Grewal, G.S., 2004. An Experimental Performance Evaluation of a Vortex Tube. *IE Journal - MC*, 1, pp.149-50.

Skye, H.M., Nellis, G.F. & Klein, S.A., 2006. Comparison of CFD Analysis to Empirical Data in a Commercial Vortex Tube. *International Journal of Refrigeration*, 29, pp.71-80.

Sohn, C.H., Jung, U.H. & Kim, C.S., 2002. Investigation of the Energy Separation Mechanism in the Vortex Tube. In *12th International Heat Transfer Conference*. Grenoble, 2002.

Stephan, K., Lin, S., Durst, M., Huang, F. & Seher, D., 1984. A Similarity Relation for Energy Separation in a Vortex Tube. *International Journal of Heat and Mass Transfer*, 27, pp.911- 920.

Streamtek, 2009. *What is a Vortex Tube?* [Online] Available at: http://www.streamtek.ca/vortex-tube.html [Accessed 23 July 2009].

Ting-Quan, M.A., Qing-Guo, Z.H.A.O., Fang, Y.E. & Chong-Fang, M.A., 2002. Experimental Investigation on Energy Separation by Vortex Tubes. In *12th International Heat Transfer Conference*. Grenoble, 2002.

Trofimov, V.M., 2000. Physical Effect in Ranque Vortex Tube. *Journal of Experimental and Theoretical Physics*, 72(5), pp.249-52.

U.S Govenment, 2005. *International Energy Annual*. [Online] Available at: http://www.eia.doe.gov/iea [Accessed 8 July 2008].

Van der Merwe, J.J., 2004. Development and Validation of Fission Product Release Models and Software at PBMR. In *2nd International Topical Meeting on High Temperature Reactor Technology*. Beijing, 2004.

Veriteq Instruments, 2008. *Type T Thermocouple Preformance Data*. [Online] Available at: http://www.veriteq.com/thermocouple-data-logger/type-t.htm [Accessed 15 September 2009].

Wereley, S.T. and Lueptow, R.M., 1999. Inertial Particle Motion in a Taylor Couette Rotating Filter. *Physics of Fluids*, 11(2), pp.325-33.

WetAir, 2005. *VORSEP*. [Online] Available at: http://www.wet-air.com/pdfs/vorsep_filters.pdf [Accessed 12 June 2009].

White, F.M., 2003. *Fluid Mechanics*. 5th ed. New York: McGraw - Hill.

World Nuclear Assocaition, 2008. *Safety of Nuclear Power Reactors*. [Online] Available at: http://www.world-nuclear.org/info/inf06.html [Accessed 16 November 2009].

World Nuclear Association, 2009. *Generation IV Nuclear Reactors*. [Online] Available at: Generation IV Nuclear Reactors [Accessed 16 November 2009].

Wu, Y.T., Ding, Y., Ji, Y.B., Ma, C.F. & Ge, M.C., 2006. Experimental Research on a Vortex Tube. In *13th International Heat Transfer Conference*. Sydney, 2006.

Yilmaz, M., Kaya, M., Karagoz, S. & Erdogan, S., 2009. A Review on Design Criteria for Vortex Tubes. *International Journal of Heat and Mass Transfer*, 45(5), pp.613 - 632.

APPENDIX A: ORIFICE FLOW METER DESIGN

As discussed in Chapter 4, the FESTO flow sensors were not compatible with helium, therefore another type of flow sensor had be to designed and built to measure the volumetric flow rate in the experimental apparatus (Figure 11) with helium as the working fluid. It was decided to design an orifice flow meter, due to its simplicity. The volumetric flow rate through the orifice flow sensor is calculated from the measured pressure drop ΔP_{ofs} across the pressure taps (see Appendix B). Figure A1 shows the design of this orifice flow sensor as well as the location of the pressure taps and the orifice plate. The flange pressure tappings are placed 25.4 mm (1") from the upstream and downstream faces of the orifice plate according to British Standards (BS 1042: Section 1.1, 1981). The upstream length of the sensor is $10d_1$ and the downstream length is equal to $5d_1$ according to the guidelines specified by Figliola and Beasley (2006) to overcome entrance effects. The diameter of the orifice sensor is given by d_1 and the orifice diameter by d_o. The value of d_1 was chosen to be 20 mm due to the size of the connecting tubing and the available connectors. This does, however, not comply with British Standards (BS 1042: Section 1.1, 1981) because it is too small.
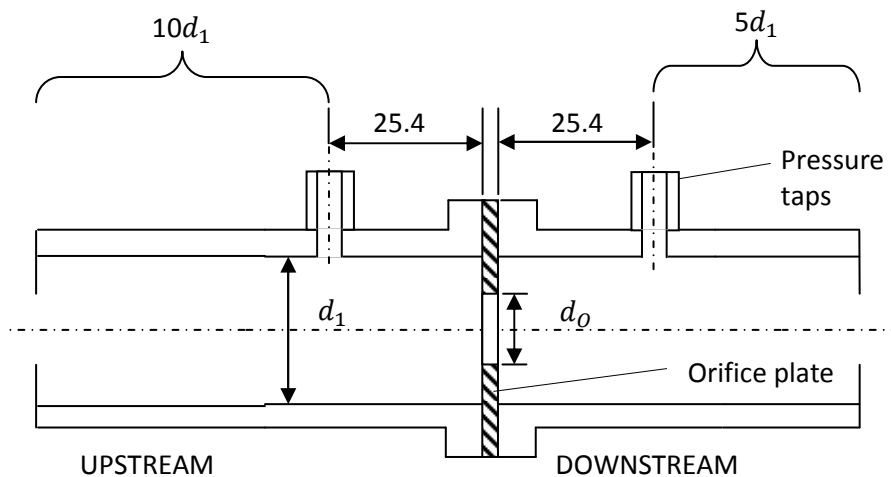
Figure A1: Orifice flow sensor cross-section

The orifice diameter d_o had to be calculated to ensure that there is a measurable pressure drop across the orifice plate for the specified flow rate range. This pressure drop had to be large enough to be detected by the Endress and Hauser pressure sensors. In a British Standard orifice flow sensor the pressure drop across the orifice plate can be calculated using a derivation of Bernoulli's equation for steady incompressible flow (Ma < 0.3). The designed orifice flow sensor, however, does not conform to the British Standards due to its chosen diameter d_1, and therefore the Bernoulli equation cannot be used to calculate the values of the pressure drop ΔP_{ofs} accurately. It was decided, however, to use this equation to calculate the pressure drop ΔP_{ofs} for different values of d_o as a guideline to approximate the size of d_o.

The derivation of the Bernoulli equation used to calculate the pressure drop ΔP_{ofs} across the orifice plate is given by White (2003) as

$$\Delta P_{ofs} = \left(\frac{G}{C_d A_o}\right)^2 \frac{\rho(1 - \beta^4)}{2}$$

A1

where β is the diameter ratio of the orifice to tube diameters as shown in equation A2

$$\beta = \frac{d_o}{d_1}$$

A2

and C_d is the discharge coefficient which is proportional to the Reynolds number Re and the friction factors f_1 and f_2 as shown in equation A3, A4, A5, A6 and A7.

$$C_d = f(\beta) + 91.71\beta^{2.5}Re^{-0.75} + \frac{0.09\beta^4}{1 - \beta^4}f_1 - 0.0337\beta^3 f_2$$

A3

$$Re = \frac{\rho G d_1}{\mu A_o}$$

A4

$$f(\beta) = 0.5959 + 0.0312\beta^{2.1} - 0.184\beta^8$$

A5

$$f_1 = 0.4333 \tag{A6}$$

$$f_2 = \frac{1}{d_{1(inches)}} \tag{A7}$$

The pressure drop across the orifice plate was thus calculated for different β values over the volumetric flow rate range of the small Exair® RHVT (which will be used in the helium experiments) and with the input values as shown in Table A1.

Table A1: Values for orifice flow sensor pressure drop calculations

Variable	Symbol	Value
Orifice flow sensor diameter [mm]	d_1	20
Inlet pressure [kPa]	P_i	300
Inlet temperature [K]	T_i	288
Air viscosity [kg/ms]	μ	3.01467 x 10^{-6}

Using the above given formulas and input values, the pressure drop across the orifice for different volumetric flow rates and diameter ratios β were plotted as shown in Figure A1. From Figure A1 it is seen that the pressure drop across the orifice plate increases with an increase in volumetric flow rate and a decrease in the β value. As stated earlier the pressure drop values indicated by Figure A1 were only used as a guideline to approximate what size the orifice diameter should be to obtain a reasonable pressure drop that could be measured with the Endress and Hauser PMD75 differential pressure sensors. Taking the results from Figure A1 into consideration, it was decided to firstly test the β = 0.4 orifice because it showed pressure drops of between 1 kPa – 10 kPa which is within the range of the Endress and Hauser pressure sensors and is also not as high as to cause a high permanent pressure loss. The orifice flow sensors were calibrated in a calibration unit with the β = 0.4 (8 mm diameter orifice) and found that

the actual found pressure drop across this 8 mm orifice was too small (in the order of < 1 kPa) to get an accurate reading on the pressure sensors. It was therefore decided to also calibrate the β = 0.2 orifice (4 mm diameter orifice) and it was found that the measured pressure drops were acceptable to be measured by the pressure sensors and was therefore used in the flow sensor. The final orifice flow meter manufacturing drawings are given in Addendum I.

The calibration curves for both orifice sizes were obtained by equating the pressure drop measured over the orifice sensor to the volumetric flow rate calculated from the calibration unit and then plotting a trendline through the data points. This procedure as well as the procedure followed to further calibrate the sensors for use in helium is shown in Appendix B.2.2
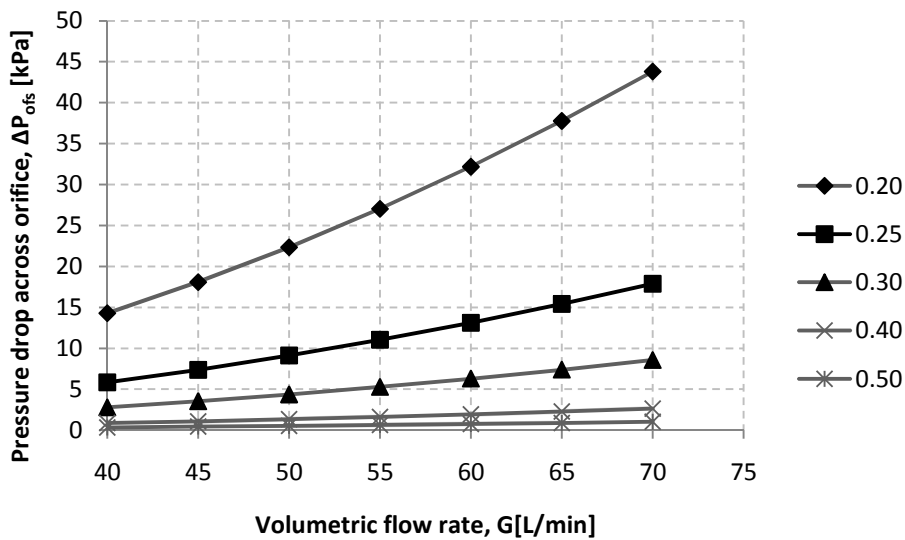
Figure A2: Pressure drop across orifice plate using equation A1

.

APPENDIX B : CALIBRATION OF SENSORS

All sensors are not 100 % accurate; therefore all sensors used in the experimental work had to be calibrated to a laboratory standard.

B.1 FESTO Pressure Sensor calibration

Two FESTO SDE3 pressure sensors (Figure B1) were calibrated using a calibrated 1000 kPa Wika Instruments pressure gauge which has an accuracy of ±0.3 %. They were calibrated statically (in non-moving flow) in both air and helium.

Figure B1: FESTO SDE3 pressure sensor

B.1.1 Calibration in Air

Both pressure sensors were calibrated in air over the pressure range of the experimental work. The pressure sensors were calibrated by setting the Wika pressure gauge to a specific value and then recording the corresponding sensor reading. By plotting the Wika pressure reading to the FESTO pressure reading, two calibration curves (Figure B2) could be drawn for both FESTO pressure sensors A and B with a linear trendline to fit the data,

which gave a coefficient of determination $R^2 = 0.999$. The linear trendline equation, which is the calibration curve, is given as

Pressure sensor A $\qquad P_{A\_corrected} = 0.993 * P_{A\_uncorrected} - 0.539 \qquad$ B1

Pressure sensor B $\qquad P_{B\_corrected} = 0.997 * P_{B\_uncorrected} - 11.53 \qquad$ B2

(a) Sensor A   (b) Sensor B
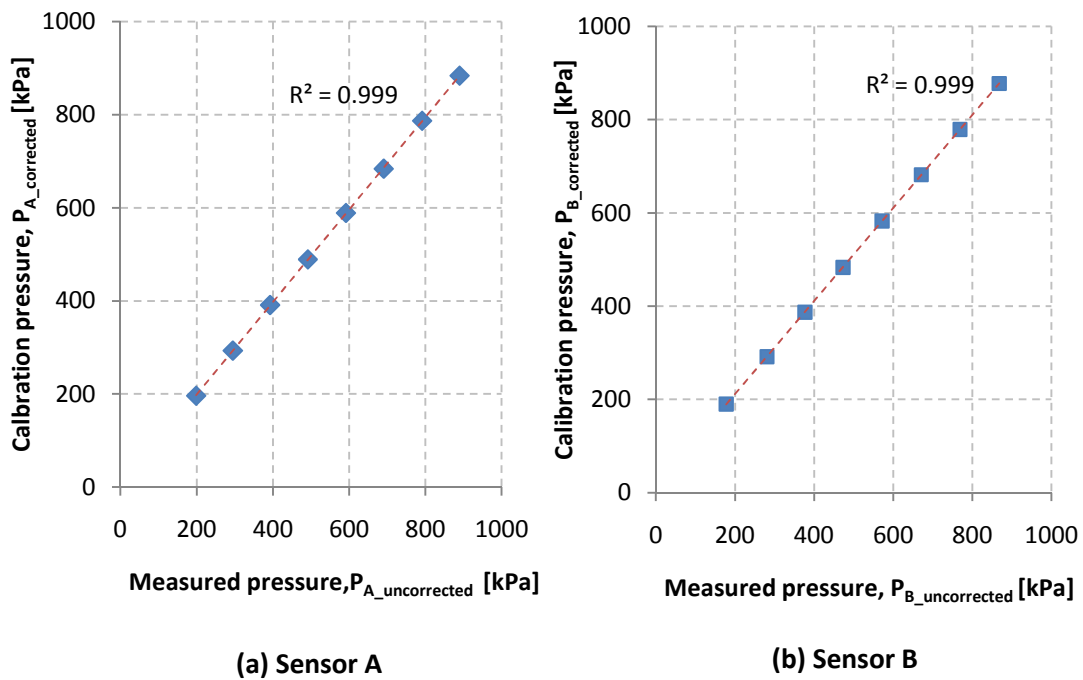
Figure B2: FESTO pressure sensor calibration curves in air

B.1.2 Calibration in Helium

The FESTO pressure sensors were also calibrated in helium using the same Wika calibration pressure gauge used for the air calibration. The same procedure, as done with the air calibration, was followed and the resulting calibration curves are shown in Figure B3 (which are also linear trendlines with $R^2 = 0.999$). The calibration equations for the FESTO pressure sensors were derived from the calibration curves and are

Pressure sensor A $\qquad P_{A\_helium\_corrected} = 0.954 * P_{A\_helium\_uncorrected} + 20.06 \qquad$ B3

Pressure sensor B $\qquad P_{B\_helium\_corrected} = 0.959 * P_{B\_helium\_uncorrected} + 31.88 \qquad$ B4

(a) Sensor A $\qquad\qquad\qquad\qquad\qquad\qquad$ (b) Sensor B
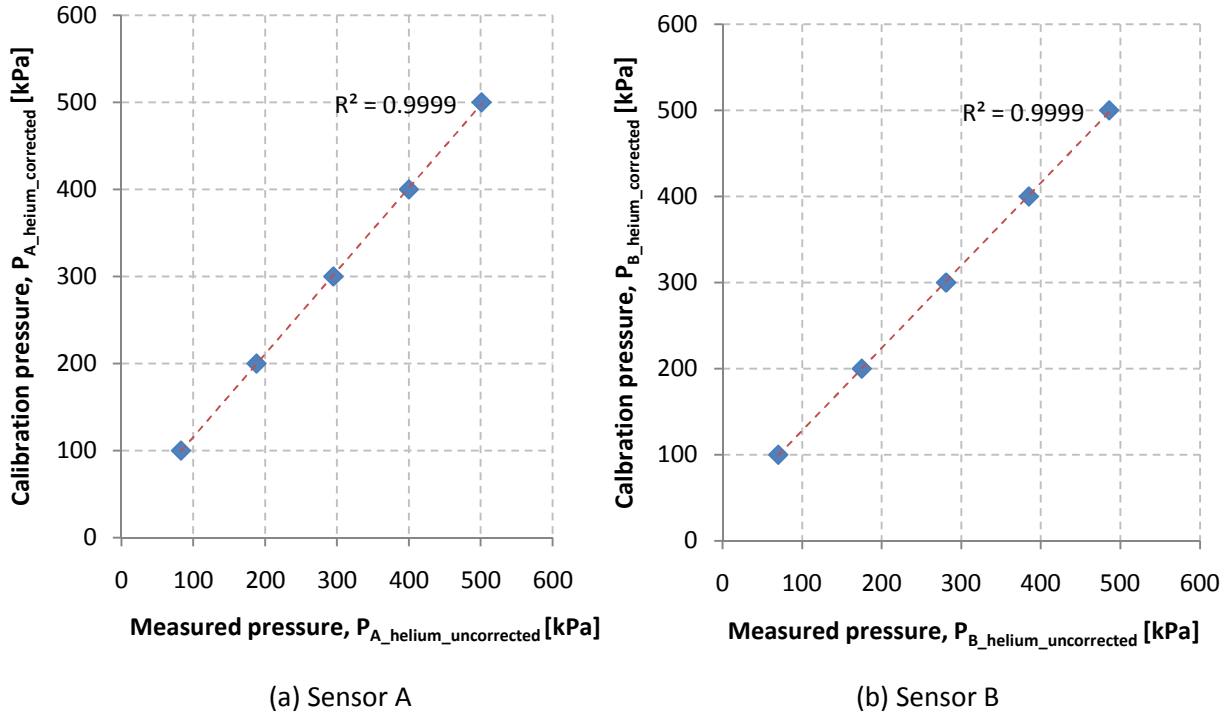
Figure B3: FESTO pressure sensor calibration curves in helium

B.2 Endress and Hauser Pressure Sensor Calibration

An Endress and Hauser PMD75 differential pressure sensor was used to measure the pressure drop across the orifice flow sensor. This measured differential pressure was then used to calculate the volumetric flow rate through the orifice flow sensor. The PMD75 was calibrated by using a Van Essen Betz micromanometer, Type 5000 model. The Betz micromanometer has a range of -10 to 5000 Pa and an accuracy of ±0.2 Pa. The Betz micromanometer is calibrated to the Netherlands Calibration Organization (Nederlandse Kalibratie Organisatie, 1991) standard and is therefore the laboratory standard which the PMD75 sensor must adhere to. The calibration was done by connecting both the micromanometer and the PMD75 in parallel to a single tube. Air

was then blown into this tube and the measured values of the PMD75 were compared to the Betz micromanometer reading. A linear calibration curve was obtained from this data, as seen in Figure B4, with R^2 = 0.996. The calibration curve is given as equation B5.
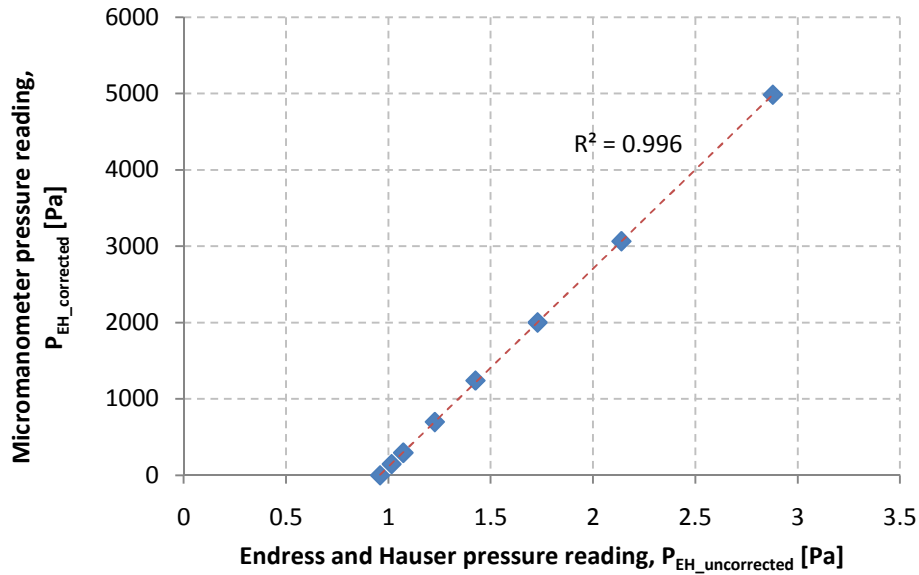
Figure B4: Endress and Hauser pressure sensor calibration curve

$$P_{EH\_corrected} = 2596.04425 * P_{EH\_uncorrected} - 2486.25736 \qquad \text{B5}$$

B.3 Flow Sensor Calibration

FESTO SFE1 and MS6 flow sensors (Figure B5) were used in the experimental work to measure the volumetric flow rate of air; for helium, the designed orifice flow sensors (see Appendix A) were used. Both these types of flow sensors had to be calibrated to a laboratory standard. The flow sensors were calibrated using a Type 55D41/42 calibration unit (British Standards Institution, 1981), shown schematically in Figure B6
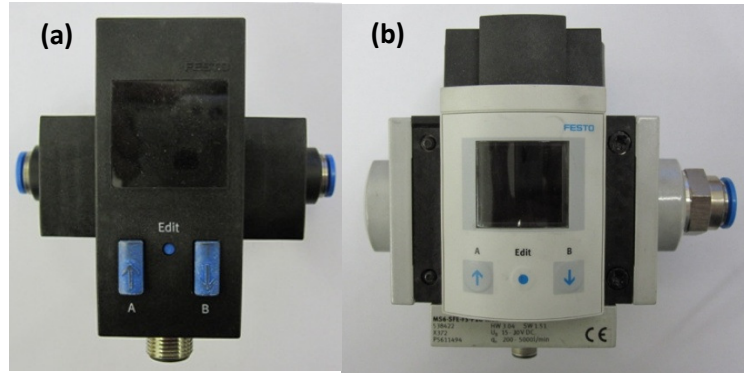
Figure B5: FESTO flow sensors (a) SFE-LF and (b) MS6-SFE
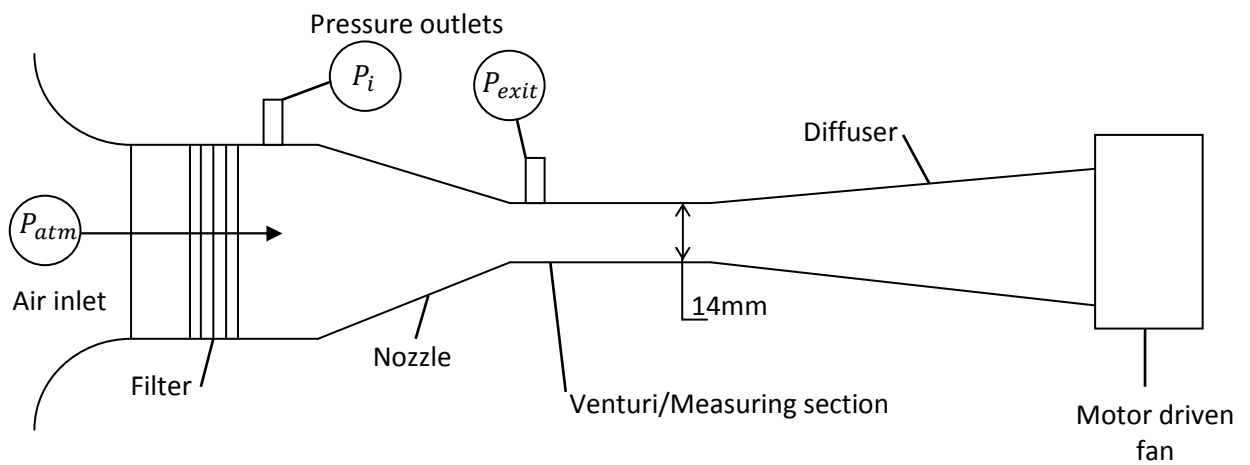
Figure B6: Flow sensor Type 55D41/42 calibration unit

The calibration unit works as follows: Inlet air at atmospheric pressure is drawn into a nozzle via a filter array. The measuring section of the calibration unit is at the throat of the nozzle. The downstream-side of the measuring section (with inside diameter 14 mm) is connected to a motor driven fan via a diffuser. The flow rate through the measuring section is controlled by varying the AC voltage supply to the motor fan with a variable transformer (Hoppe et al., n.d.). The pressure at the inlet of the calibration unit P_i as well as the pressure drop across the nozzle $\Delta P = P_i - P_{exit}$ is measured electronically with the calibrated Endress and Hauser PMD75 pressure transducer. From these pressure readings the velocity through the orifice can be calculated using the following equation, provided in the calibration unit specifications (Hoppe et al., n.d.):

$$V_o{}^2 = \frac{2\mathcal{R}T_{atm}\Delta P}{P_i}\left(1 + \frac{1}{2k}\frac{\Delta P}{P_0}\right) \qquad\qquad \text{B6}$$

According to the calibration unit specification the bracketed term can be set to 1 if the pressure drop across the nozzle is less than 200 mmH$_2$0. The maximum measured pressure drop across the nozzle ΔP was ±1200 Pa (122.4 mmH$_2$0), which is less than 200 mmH$_2$0, therefore equation B6 reduces to

$$V_o = \left(\frac{2\Delta P}{\rho}\right)^{0.5} \qquad\qquad \text{B7}$$

with

$$\rho = \frac{P_i}{\mathcal{R}T_{atm}} \qquad\qquad \text{B8}$$

The volumetric flow rate through the calibration unit can then be calculated by

$$G_{calibration} = V_o A_o \qquad\qquad \text{B9}$$

where A_o is the area of the measuring section and is equal to 12.57 x 10^{-6} m^2.

The flow sensors were calibrated by setting the AC voltage of the motor driven fan of the calibration unit to a specific value and then calculating the corresponding volumetric flow rate with equations B7 and B9 and then comparing the calibration unit reading to the FESTO or orifice flow sensor readings. The calibration results of the FESTO and the orifice flow sensors will now be discussed separately.

B.3.1 FESTO Flow Sensors Calibration

Both the small flow rate (SFE1-LF series) and large flow rate (MS6-SFE series) FESTO sensors were calibrated using the Type 55D41/42 calibration unit. The results are shown below in Figure B7 and Figure B8. From these graphs the calibration equations were determined by plotting a linear trendline through the data points which gave R^2-values of 0.998 for the SFE1 sensors graphs and 0.999 for the MS6 sensors graphs.
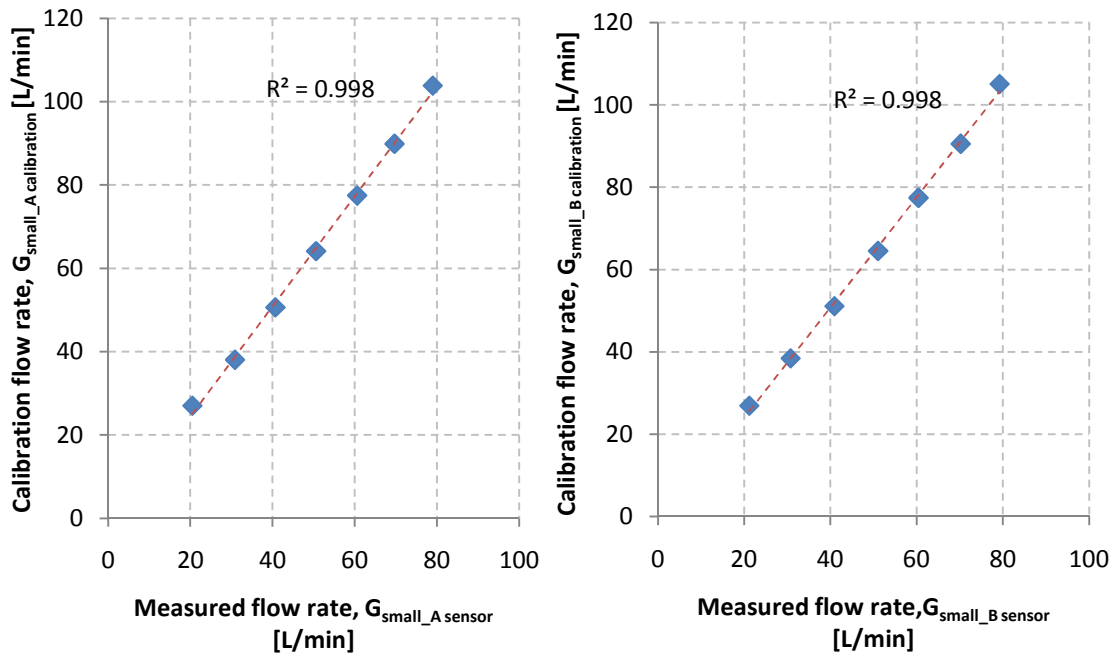
Figure B7: FESTO SFE1 – LF series flow sensors calibration curves
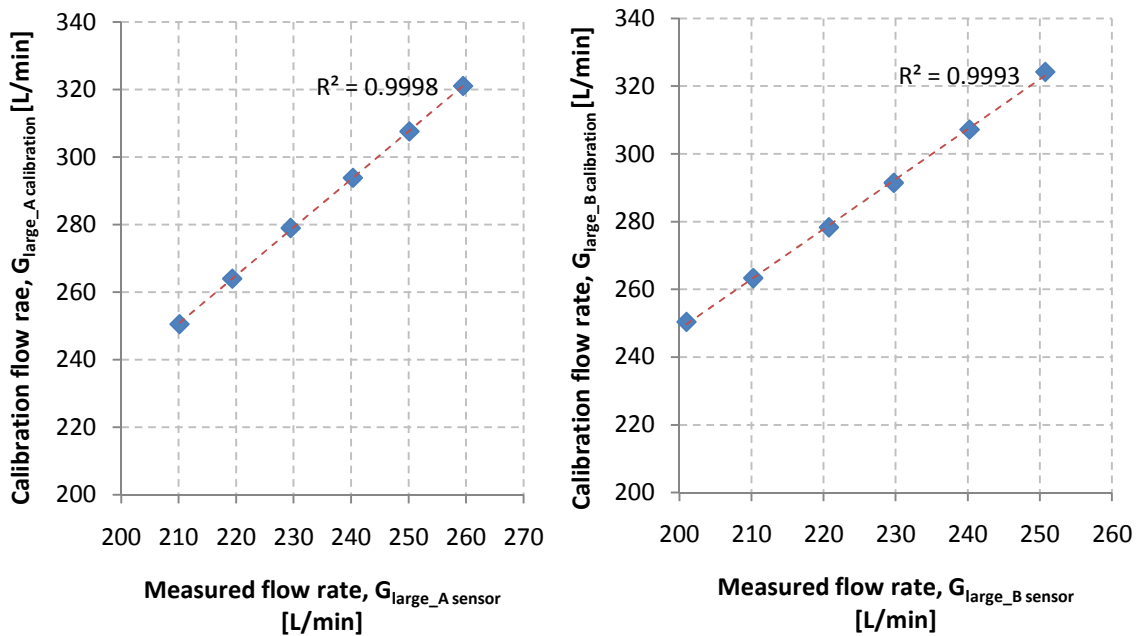
Figure B8: FESTO MS6-SFE flow sensors calibration curves

The calibration equations for all four sensors therefore are:

| SFE1 sensor A | $G_{small\_A\ calibration} = 1.321 \cdot G_{small\_A} - 1.987$ | B10 |

| SFE1 sensor B | $G_{small\_B\ calibration} = 1.337 \cdot G_{small\_B} - 2.762$ | B11 |

| MS6 sensor A | $G_{large\_A\ calibration} = 1.423 \cdot G_{large\_A} - 48.30$ | B12 |

| MS6 sensor B | $G_{large\_B\ calibration} = 1.476 \cdot G_{large\_B} - 47.13$ | B13 |

B.3.2 Orifice Flow Sensor Calibration

The orifice flow sensors were designed to measure the volumetric flow rate in helium. Due to the fact that the orifice diameter of these sensors do not comply with British Standard (BS 1042: Section 1.1, 1981), the general equations used to calculated the volumetric flow rate through the sensor for a given pressure drop across the orifice plate (see Appendix A) cannot be used and the sensor therefore had to be calibrated. First the orifice sensors were calibrated in air because the Type 55D41/42 calibration unit can only be used with air as working fluid. The same calibration procedure was followed as was done with the calibration of the FESTO sensors. The resulting calibration curve (Figure B9) was then constructed for both orifice flow sensors with a $\beta = 0.2$ orifice plate. The calibration equation was plotted as a power curve trendline with a R^2-value of 0.996 and is given by equation B14 as:

$$G_{calibration} = 0.815 \Delta P_{ofs}{}^{0.5}$$

B14
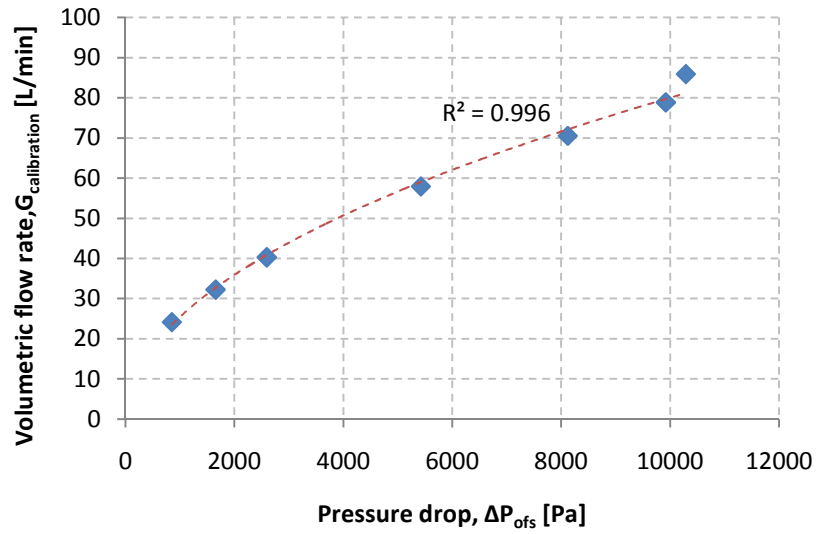
Figure B9: Orifice flow sensors calibration curve

To be able to use the orifice plate sensor in helium, this calibration equation had to be adjusted so that it can also be used with fluids other than air. To do this the calibration equation was compared to the general equation (equation B15) for an orifice plate flow sensor from White (2003) as

$$G = kA_o \sqrt{\frac{2\Delta P_{ofs}}{\rho}} \qquad\qquad \text{B15}$$

Equating equations B14 and B15 yields

$$G = 0.815\sqrt{\Delta P_{ofs}} = KA_o \sqrt{\frac{2\Delta P_{ofs}}{\rho}} \qquad\qquad \text{B16}$$

The area of the orifice plate A_o stays constant, thus the right hand side of the equation can be simplified to

$$G = 0.815\sqrt{\Delta P_{ofs}} = K \sqrt{\frac{\Delta P_{ofs}}{\rho}} \qquad\qquad \text{B17}$$

The constant K can now be calculated by substituting the density ρ with calculated density of air $\rho_{air} = \frac{P_i}{\mathcal{R}T_{atm}} = \frac{90}{0.287 \cdot 288} \approx 1.1$ kg/m^3 into equation B17.

$$K = 0.815\sqrt{\rho_{air}} = 0.815\sqrt{1.1} = 0.874 \qquad\qquad \text{B18}$$

Substituting the value of K into the right hand side of equation B17, a general equation to calculate the volumetric flow rate through the orifice flow sensor is obtained:

$$G_{helium} = 0.874\sqrt{\frac{\Delta P_{ofs}}{\rho_{helium}}} \qquad\qquad \text{B19}$$

By substituting the relevant density of the working fluid into equation B19, this equation can be used for any fluid. To calculate the volumetric flow rate through the orifice flow sensor, the density of the helium in the experiment would have to be calculated at the inlet of the sensor, and substituted into equation B19. The density of the helium can be calculated by using the ideal gas law.

B.3 Thermocouple Calibration

Three thermocouples were used in the experimental work: one for measuring the inlet air/helium temperature of the RHVT T_i and the other two for measuring the hot T_h and cold T_c outlet air/helium temperatures respectively. These T-type thermocouples had to be calibrated. The calibration was done by measuring a known temperature with the thermocouples (such as the boiling temperature of water) and then comparing these measured values to the known value. All three thermocouples were first calibrated in ambient air. The ambient air temperature T_{amb} was measured with a calibrated thermometer. Secondly the thermocouples were calibrated in boiling water which has a known temperature T_{boil} of 99.97 °C at P_{atm} = 101.325 kPa (Çengel and Boles, 2001). Table B1 shows the measured thermocouple temperatures and the known temperatures for both ambient air and boiling water. The difference between the measured thermocouple values and the known temperature ΔT is then calculated.

From Table B1 it is shown that the temperature difference between the measured thermocouple values and the actual known values is less than 1°C in ambient air and approximately equal to 1°C in boiling water. This temperature difference is insignificant

for the measurement purposes of the experimental work and therefore no adjustment to the measured thermocouple values was deemed necessary.

Table B1: Thermocouple calibration in ambient air and boiling water

Ambient temperature			
T_{amb} [°]	T_i [°]	T_h [°]	T_c [°]
18.80	18.87	18.29	18.36
$\varDelta T$	0.07	0.51	0.44
Boiling water			
T_{boil} [°]	T_i [°]	T_h [°]	T_c [°]
99.97	98.97	98.78	99.01
$\varDelta T$	1.00	1.19	0.96

APPENDIX C: COMPUTATIONAL FLUID DYNAMICS

Computational fluid dynamics (CFD) is a branch of fluid mechanics that uses numerical methods to solve and analyse problems that involve fluid flow. CFD works by solving the governing equations of continuity, momentum and energy numerically over a computational domain of interest with specified boundary conditions and initial values. The process of performing a CFD simulation consists of the following stages:

- Determining/creating the computational domain and mesh
- Defining the boundary conditions and physical parameters of the flow
- Simulation of the flow by solving the governing equations
- Post-processing of the results

These components will now be discussed in detail.

C.1 Computational Domain and Mesh

The computational domain chosen for this CFD simulation was the internal flow volume of the small Exair® RHVT. The main features of the RHVT flow domain that have to be modelled are the inlet nozzles, vortex generator entrance region, inner tube and hot and cold outlets. The size and geometry of the vortex generator entrance region, inner tube and cold outlet were determined by measurement with a Vernier calliper. The six inlet nozzles through which air enters the main flow domain of the RHVT, forms part of the vortex generator of the Exair® RHVT (see Figure C1), and creates the vortex flow within the inner tube of the RHVT. These nozzle sizes and geometry were first measured with a digital Vernier calliper under a microscope. This did not give accurate enough results due to the small size of the nozzles. It was therefore decided to photograph the vortex generator and then determine the geometry using Computer Aided Design (CAD) techniques. Figure C1 (a) shows a photograph of the small RHVT vortex generator taken at a perpendicular angle to the surface and Figure C1 (b) shows the CAD drawing drawn over the profile of the vortex generator photograph. In Figure C1 (b) it can be seen that the CAD profile drawing shows that the inlet nozzles have a somewhat converging/diverging nozzle profile. Although not all the nozzles of the vortex generator

have the same geometry, they are all essentially a rectangular slot with a nozzle width of that shown in Figure C1 (b). To determine the exact size of the nozzles, the scale of the profile drawing in CAD had to be determined. This was done by measuring the outside, inner and cold orifice diameters of the vortex generator with a Vernier and then comparing these diameters to the same measured CAD dimensions. By comparing the measured diameters with the CAD dimensions, an average ratio could be determined between the actual geometric values and the CAD dimensions, which was then applied to the nozzle CAD dimensions to determine its actual measurements as given in Table C1.
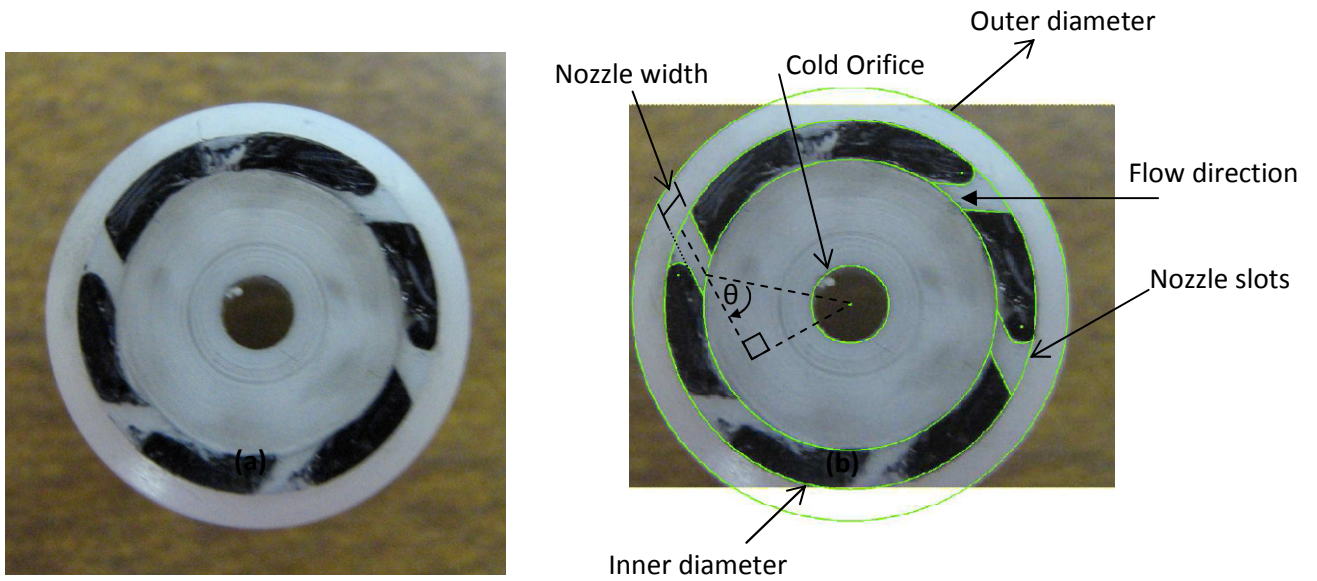
Figure C1: (a) Photograph of small RHVT vortex generator, (b) CAD drawing in green on vortex generator photograph

Table C1: Geometric measurements of vortex generator inlet nozzle

Measurement	Symbol	Value
Nozzle width [mm]	l_n	0.77
Nozzle height [mm]	h_n	0.2
Nozzle total inlet area [mm^2]	A_n	0.154
Nozzle inlet angle [°]	θ_n	52

The nozzle angle was also measured in CAD between the centreline of the nozzle and the intersection of the centreline with the circle radius at the estimated outlet of the nozzle, and was found to be 52°. The geometry of the hot outlet could not be determined with a Vernier calliper or the CAD photograph method due to its very small size and that it is obstructed by the flow control device. The size of the hot outlet therefore had to be approximated in the computational domain as 0.3 mm.

It was decided to simulate a two - dimensional axisymmetrical computational domain as it would require less computational power than a three - dimensional model. The two - dimensional computational domain (Figure C2) consists of a radial inlet slot (which has the same flow area as all 6 inlet nozzles combined) from which air enters perpendicular to the slot inlet; the vortex generator entrance region, which is the flow area through the vortex generator inner hole and the diverging tube of the vortex generator cap (as shown in Figure C3); the inner tube and the hot and cold outlets. The exact dimensions of the computational domain are given in Addendum I.
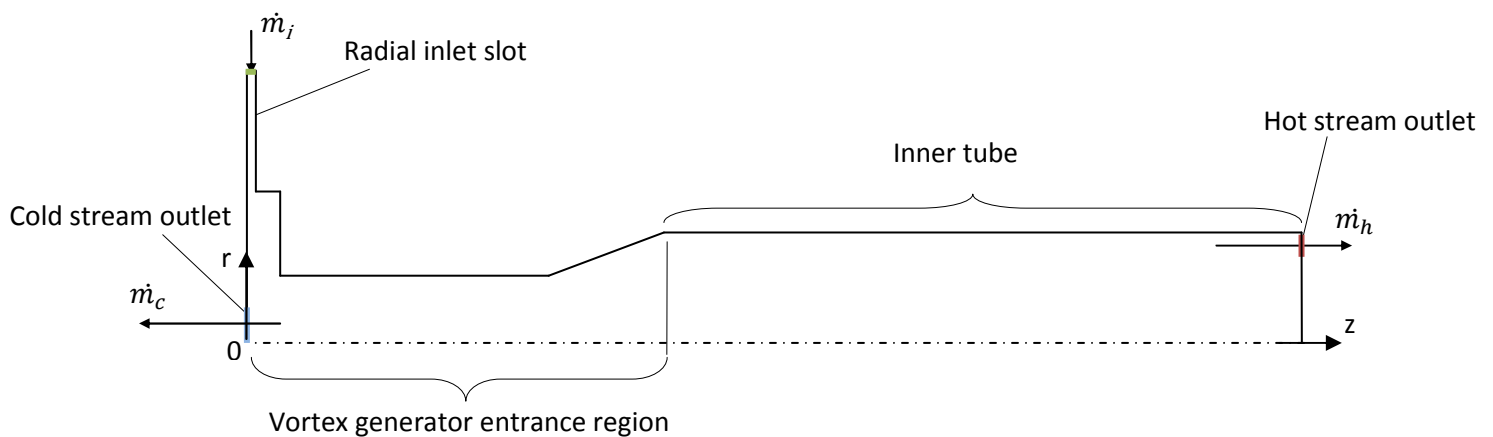
Figure C2: Computational domain (not to scale)
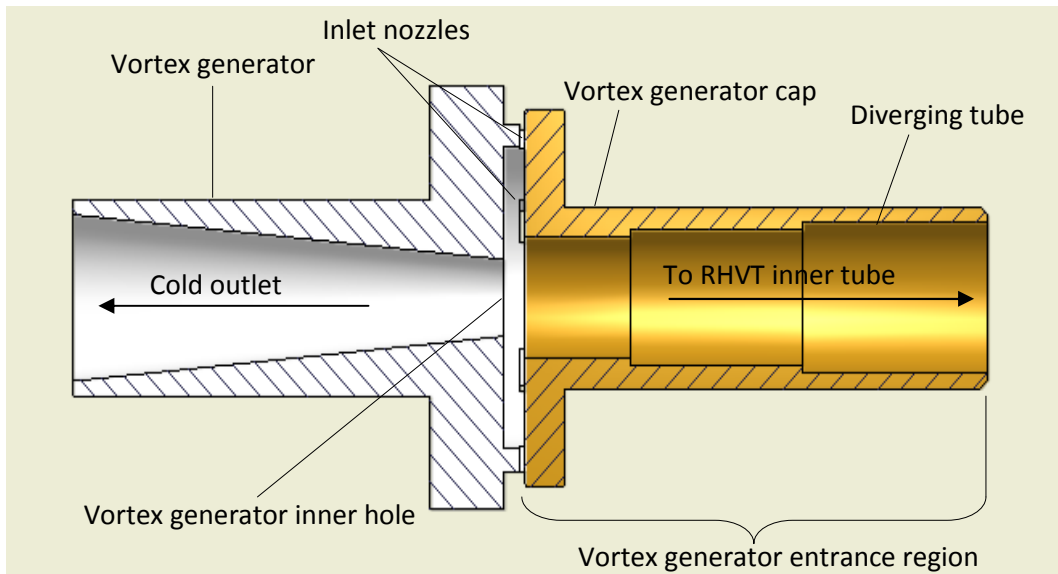
Figure C3: Cross-section of vortex generator entrance region consisting of the vortex generator and vortex generator cap

The computational mesh was then generated by using GAMBIT (ANSYS GAMBIT, 2006) software as follows:

⇢ Construct the outer edges in accordance with the computational domain dimensions, consisting out of 12 edges as shown in Figure C4.
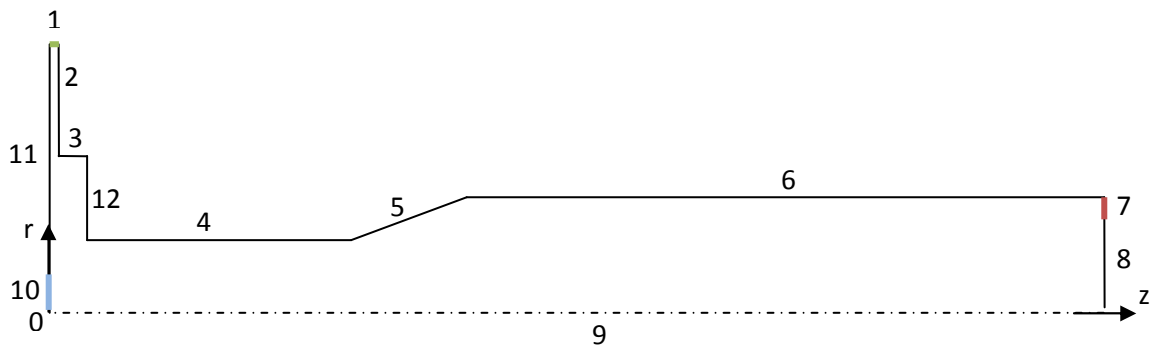
Figure C4: Mesh outer edges

⇢ Next construct 7 vertices as shown in Figure C5 at the following coordinates:

Table C2: Internal vertices coordinates

Vertex	z-coordinate [mm]	r-coordinate [mm]
a	0	3
b	1.075	4.5
c	0	1.2
d	1.075	2
e	1.075	0
f	10.5	0
g	10.5	2
h	17.5	0
i	17.5	3.175
j	93	0
k	93	3.175
l	94	3.175
m	95	2.5
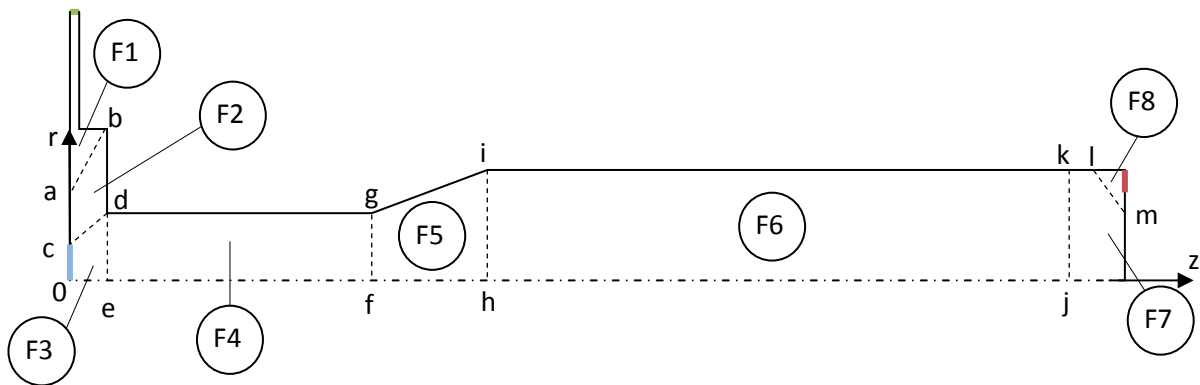
Figure C5: Mesh internal layout

⇢ Connect the constructed vertices as shown in Figure C5.

⇢ Create 8 faces, F1 – F8 as shown in Figure C5.

⇢ Mesh edge 1 with a "Successive ratio" of 1 and an "Interval count" of 10.

⇢ Mesh edge 2 with a "Successive ratio" of 1.01 (closer spacing towards outside) and an "Interval count" of 120.

⇢ Mesh edge 3 with a "Successive ratio" of 1 and an "Interval count" of 80.

- Mesh internal edge from vertex a – b with a "Successive ratio" of 1 and an "Interval count" of 100.
- Mesh edge 11 from vertex a to edge 1 with a "Successive ratio" of 0.99 and an "Interval count" of 200.
- Mesh face 1 (F1) using the "Tri Pave" option.
- Mesh edge 4 with a "Successive ratio" of 1 and an "Interval count" of 200.
- Mesh internal edge from vertex c - d with a "Successive ratio" of 1 and an "Interval count" of 200.
- Mesh edge 11 from vertex a - c with a "Successive ratio" of 1 and an "Interval count" of 100.
- Mesh face 2 (F2) using the "Tri Pave" option.
- Mesh edge 10 with a "Successive ratio" of 1 and an "Interval count" of 100.
- Mesh internal edge from vertex d – e with a "Successive ratio" of 1 and an "Interval count" of 100.
- Mesh edge 9 from vertex e to edge 10 with a "Successive ratio" of 1 and an "Interval count" of 100.
- Mesh face 3 (F3) using the "Tri Pave" option.
- Mesh rest of edge 4 and edge 9 from vertex e - f with a "Successive ratio" of 1.01 and an "Interval count" of 100.
- Mesh internal edge from vertex f - g from "Successive ratio" of 1 and an "Interval count" of 30.
- Mesh face 4 (F4) using the "Tri Pave" option.
- Mesh edge 5 and edge 9 from vertex f – h with a "Successive ratio" of 1 and an "Interval count" of 80.
- Mesh internal edge from vertex edge h - i with a "Successive ratio" of 1 and an "Interval count" of 50.
- Mesh face 5 (F5) using the "Tri Pave" option.
- Mesh edge 6 and edge 9 from vertex h – j with a double-sided "Successive ratio" of 1.01 (closer spacing towards outside) and an "Interval count" of 400.
- Mesh internal edge from vertex j – k with a "Successive ratio" of 1 and an "Interval count" of 80.

- → Mesh face 6 (F6) using the "Tri Pave" option.
- → Mesh edge 9 from vertex j to edge 8 with a "Successive ratio" of 1 and an "Interval count" of 50
- → Mesh edge 8 from vertex m to edge 9 with a "Successive ratio" of 1.02 and an "Interval count" of 80
- → Mesh internal edge from vertex l – m with a "Successive ratio" of 1 and an "Interval count" of 60
- → Mesh edge 6 from vertex k – l with a "Successive ratio" of 0.98 and an "Interval count" of 40
- → Mesh face 7 (F7) using the "Tri Pave" option
- → Mesh edge 6 from vertex l to edge 7 with a "Successive ratio" of 0.99 and an "Interval count" of 50
- → Mesh edge 7 with a "Successive ratio" of 1 and an "Interval count" of 15
- → Mesh edge 8 from vertex m to edge 7 with a "Successive ratio" of 1.01 and an "Interval count" of 15
- → Mesh face 8 (F8) using the "Tri Pave" option
- → Specify the boundaries as:

    Edge 9:   Axis

    Edge 1:   Mass flow inlet

    Edge 7:   Pressure outlet (HOT)

    Edge 10:   Pressure outlet (COLD)

    All internal edges: Interior

C.2 Boundary Conditions and Physical Flow Parameters

The four boundary conditions of the mesh boundaries, as shown in the last bullet above, have to be specified by assigning them specific values. The mass flow inlet boundary condition specifies the mass flow rate, inlet pressure and direction vectors of the flow rate at the inlet of the radial inlet slot. Since the radial inlet slot is an approximation of all 6 inlet nozzles, the flow conditions of the nozzles were measured in the small Exair® RHVT. At the inlet of the small Exair® RHVT compressed air enters a supply tube and then flows into the inlet nozzles (as shown in Figure C1)

The through-flow area of these nozzles is much smaller than that of the supply tube and therefore choking occurs at the nozzles. Since choking occurs, the maximum possible mass flow rate that can go through the radial slot in the CFD mesh has to be calculated. This maximum mass flow rate, neglecting friction, was calculated using basic gas dynamics and with the assumption that the air in the nozzles is at sonic conditions. According to White (2003)

$$\dot{m}_{max} = \frac{0.6847 P_0 A^*}{\sqrt{\mathcal{R} T_0}}$$

C1

where the stagnation conditions, assuming negligible velocity in the supply tube are $P_0 = 570$ kPa (gauge) $= 671.325$ kPa (abs) and $T_0 = 294$ K in air with properties $k \approx 1.4$ and $\mathcal{R} \approx 287$ J/kg·K. A^* is the maximum through-flow area and is the total nozzle area of all six nozzles which is equal to $6 \times A_s = 0.924 \times 10^{-6}$ mm^2

Substituting these values into equation C1, the maximum mass flow rate is calculated as

$$\dot{m}_{max} = \frac{0.6847 P_0 A^*}{\sqrt{\mathcal{R} T_0}} = \frac{0.6847 \times 671325 \times 0.924 \times 10^{-6}}{\sqrt{287 \times 294}} = 0.00146 \text{ kg/s}$$

The maximum mass flow rate, calculated using equation C1, together with the stagnation pressure P_0 will be used as the mass flow rate inlet conditions for the CFD simulation. The direction vectors of the mass flow rate also need to be specified. At the mass flow inlet in the computational mesh, flow enters normal to the slot outlet. In the Exair® RHVT the flow enters at an angle of 52 ° due to the inclination of the nozzles. Therefore the mass flow rate $\dot{m}_i$ has to be specified in terms of its radial $\dot{m}_r$ and tangential $\dot{m}_\theta$ components, see Figure C6. The CFD simulation calculates these components for a specified direction vector. The tangential $\vec{\theta}$ and radial $\vec{r}$ unit vectors are therefore required and are calculated as $\vec{r} = \cos\theta$ and $\vec{\theta} = \sin\theta$. The resulting mass flow inlet boundary conditions for the numerical simulation are given in Table C3.
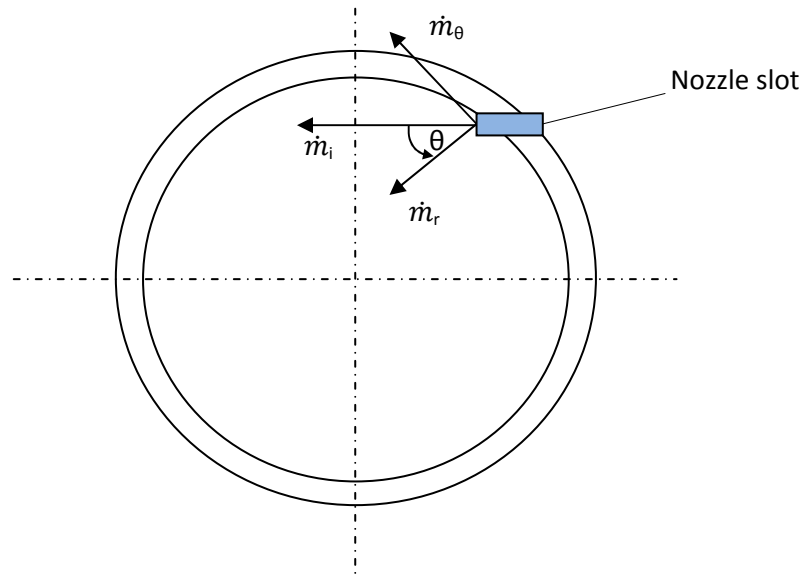
Figure C6: Radial and Tangential components of mass flow rate vector

Table C3: Mass flow inlet boundary conditions used in the CFD simulation

Variables	Symbol	Value
Mass flow rate [kg/s]	$\dot{m}_{max}$	0.00146
Gauge pressure [Pa]	P_0	570000
Radial direction vector	$\vec{r}$	-0.615
Tangential direction vector	$\vec{\theta}$	0.788

The hot and cold outlets are specified as "Pressure outlet" boundary conditions. The pressure at these outlets is varied by a User Defined Function (UDF) which was written by Prof. Thiart to control the volume fraction of the RHVT computational domain. Usually the volume fraction is controlled by the area ratio between the hot and cold outlets (set by the flow control device) but since the area of the hot outlet could not be measured accurately, the UDF had to be used to control the volume fraction. The UDF therefore changes the volume fraction of the flow to a set value by adjusting the pressures at the hot and cold outlets. The UDF furthermore calculates the maximum mass flow rate (using the same formulas given above) for a given stagnation pressure, stagnation temperature and fluid conditions. The UDF also prevents divergence of the solution during the initial iterations of the numerical simulation by starting the

simulation with only 10 % of the maximum mass flow rate and then incrementally increasing the mass flow rate over a specified number of iterations until the maximum flow rate is reached. The UDF was written in C - code and is shown in Addendum II.

The physical flow in the RHVT is compressible and turbulent (Akhesmah et al., 2008). The compressibility of the flow is set in the solver, as shown in section C.3. To account for turbulence in the RHVT a suitable turbulence model has to be selected. Firstly experimental results of a flow domain similar to that of the RHVT had to be found in literature. This flow domain was then modelled numerically with different turbulence models and the turbulence model that best fit the experimental results was then the most suitable model to use in the RHVT simulation. In 1984 Morsi and Clayton did experiments to determine the principle characteristics of turbulent swirling flow in an annulus. Their experimental setup consisted of two concentric stationary cylinders of equal length with a vortex generator at the inlet to provide swirling flow through the annulus between these two cylinders (as shown in Figure C7). The inner cylinder had an outer diameter of 56 mm and the outer cylinder had an inner diameter of 109 mm. The length of the cylinders along which the tests were conducted was 938 mm. The vortex was generated by a set of forty guide vanes placed symmetrically around the entrance of the cylinders.
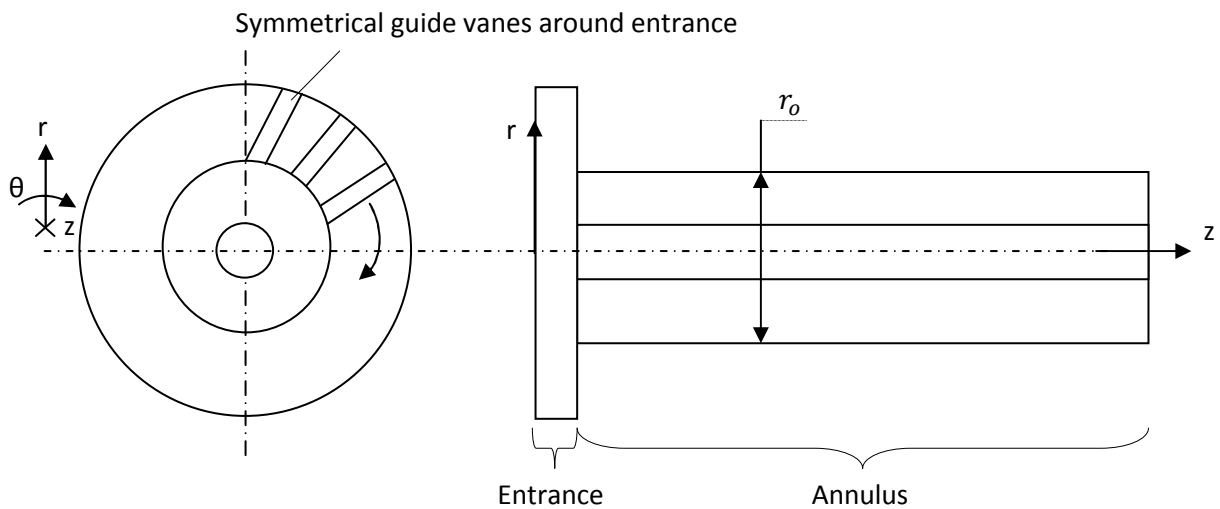
Figure C7: Morsi and Clayton (1984) experimental annular flow domain

In Morsi and Clayton's experiments the axial and swirl velocity profiles at the inlet as well as at different axial stations along the annulus were measured. The locations of these axial measurement stations are shown in Table C4.

Table C4: Morsi and Clayton's axial measurement stations locations

Station	1	2	3	4	5	6
Axial distance [mm]	0	69	127	185	243	301

In the CFD simulation only the annulus domain (see Figure C7) was modelled as an axisymmetrical two - dimensional model and the vortex flow generated at the entrance was simulated as a velocity profile at the entrance side of the annulus. This domain was then simulated using four turbulence models:

1. Laminar
2. k-ε model
3. Reynolds stress model
4. k-ε RNG (Renormalization group) model with Non-equilibrium wall effects

The numerical results for each turbulence model were then compared to the experimental data from Morsi and Clayton (1984), and are shown in Figure C8 and Figure C9. Figure C8 shows the resulting numerical axial velocity profiles at the different measuring stations (1- 6) along the normalized radius $= {^r}/{_{r_o}}$, where r_o is the radius of the outer cylinder, as well as the experimental results from Morsi and Clayton (1984), and Figure C9 shows the swirl velocity. From these graphs it can be seen that the k-ε RNG model with Non-equilibrium wall effects compares the best to the experimental results and was thus used in the RHVT CFD simulation.
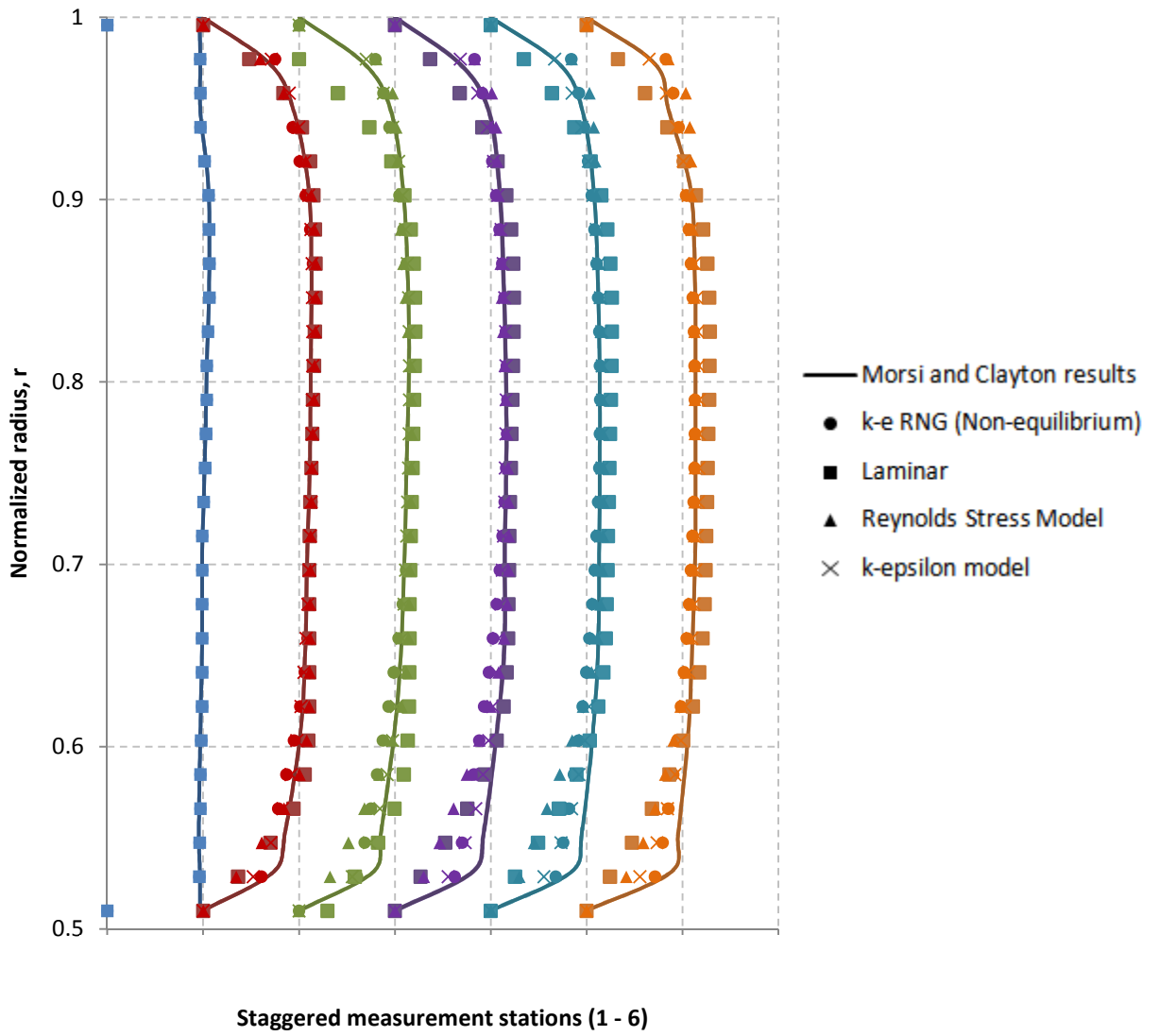
Figure C8: Numerical axial velocity profiles for different turbulence models compared to the experimental results of Morsi and Clayton (1984)
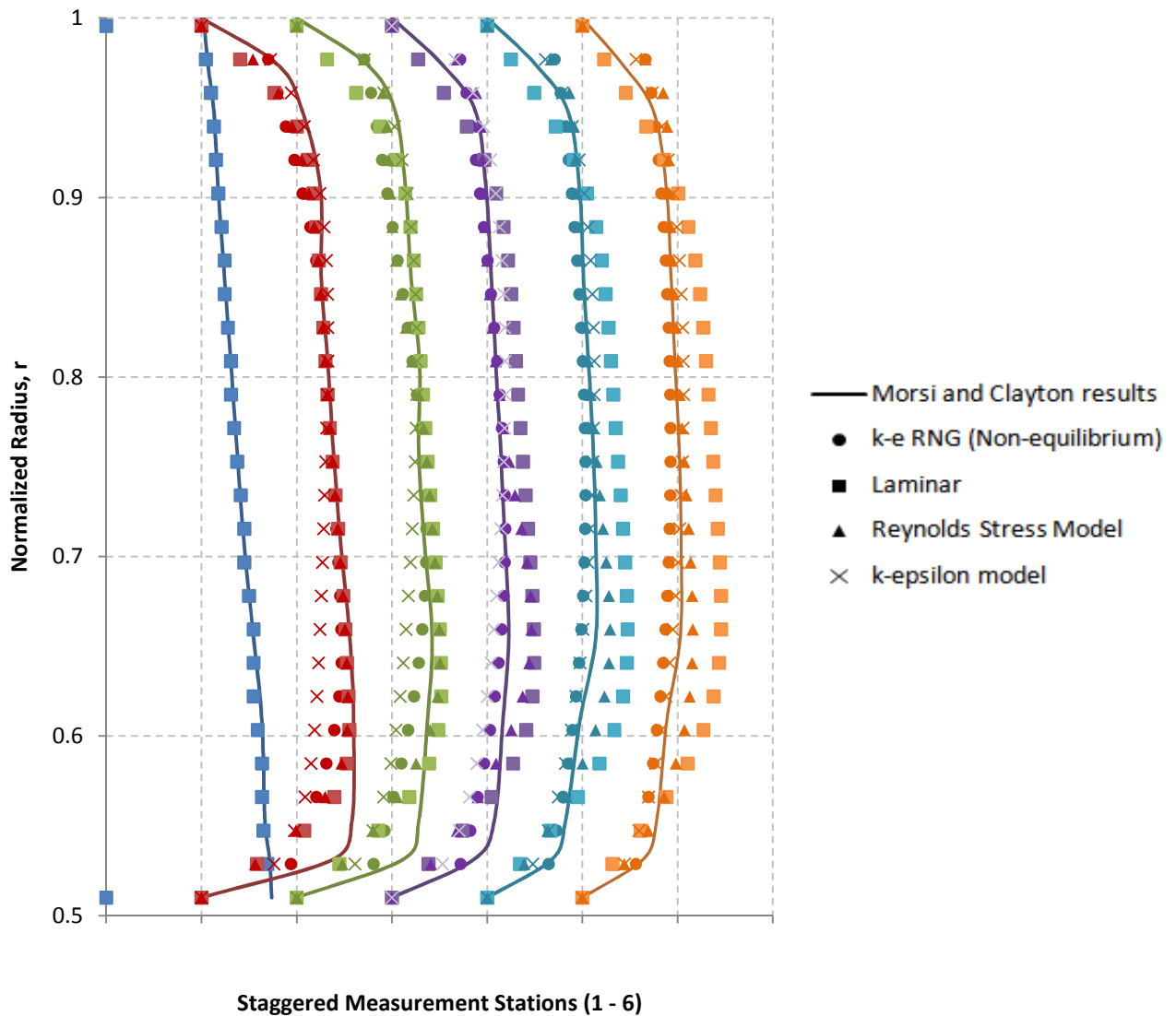
Figure C9: Numerical swirl velocity profiles for different turbulence models compared to the experimental results of Morsi and Clayton (1984)

C.3 Flow Simulation

The two - dimensional mesh is loaded into the CFD solver FLUENT using the two - dimensional double precision "2ddp" mode. FLUENT (ANSYS FLUENT, 2006) is a general-purpose CFD code based on the finite volume method on a collocated grid. The physical parameters and boundary conditions are set as follows:

⇢ Scale imported mesh to meters.

⇢ Solver set to "Green-Gauss Node-Based" and "Axisymmetric Swirl".

- ⇥ Material properties for air amended to "ideal-gas" for density to model compressibility effects.
- ⇥ Enable "Energy Equation".
- ⇥ Viscous model set to "k-epsilon" with "RNG", "Swirl Dominated Flow" and "Non-Equilibrium Wall Functions" activated. Also activate "Viscous Heating".
- ⇥ Operating pressure set to 101 325 Pa.
- ⇥ Boundary conditions set as follows:
  - ○ Hot and Cold pressure outlet set to "PexitHot" and "PexitCold" respectively from UDF and "Backflow Direction Specification Method" set to "From Neighbouring Cell" and Turbulence "Specification Method" set to an "Intensity and Viscosity Ratio" of 1 % and 10 % respectively.
  - ○ Mass flow inlet boundary condition set to "MassFluxInlet" and "Supersonic/Initial Gauge Pressure" set to "Pinlet" (from UDF). "Direction Specification" set to "Direction Vector" with components: Radial = $\vec{r}$, Tangential = $\vec{\theta}$. Also set Turbulence "Specification Method" to an "Intensity and Viscosity Ratio" of 1 % and 10 % respectively.
- ⇥ Monitor convergence levels for residuals of all equations set to 1 x 10^{-10}.
- ⇥ Solver controls set as follows:
  - ○ Discretization method set to "PRESTO" for continuity and "Second Order Upwind" for the remaining equations.
  - ○ Pressure-Velocity coupling set to SIMPLEC with the under-relaxation factors set to the values shown in Table C5.

Table C5: Under-relaxation factors

Pressure	0.1
Density	0.1
Body forces	0.1
Momentum	0.1
Swirl velocity	0.1
Turbulent kinetic energy	0.1
Turbulent dissipation rate	0.1

Turbulent viscosity	0.1
Energy	0.1

⇥ Execute UDF with "ResetRestartFile" command.

⇥ Initialize solution.

⇥ Iterate for number of iterations specified in UDF.

The governing equations are solved iteratively to satisfy the specified boundary conditions of the CFD computational domain. For each iteration, an error, or residual is reported as a measure of the overall conservation of the governing equations. For this simulation the residuals are set to 1×10^{-10} which means that the solution will converge (or the governing equation will be conserved) when the error is equal or less than 1×10^{-10}. The first simulation was run for 5200 iterations (until the mass flow reached its maximum value), after which the solution did not converge. How close the final CFD solution is to the exact solution is determined by a number of factors, including the size of the mesh control volumes and the size of the final residuals. After 5200 iterations the residuals were still high (1×10^{-3}), which showed that further iterations were needed to get the exact solution. The next simulation was run for up to a total of 6000 iterations and showed almost no decrease in the residuals. Due to the long computing time required for this simulation and the lack of reduction of the residual values, it was decided to also refine the computational mesh. The mesh was refined by "gradients" of static temperature and velocity magnitude in the FLUENT solver by computing the gradients in static temperature and velocity magnitude and then refining the mesh to 10 % of the gradients' current value.

The simulation was then run until the residuals converged to a steady value. The mesh refinement continued for a total of 95000 iterations after which the computer was not able to refine the mesh any further and neither obtain a steady value of convergence. Since the available computer could not continue the simulation, it is proposed that a better computer or computer cluster might be used in future to obtain more accurate results.

C.4 Post-Processing of Results

In this section the post-processing of the preliminary CFD numerical results will be discussed and compared to the analytical analysis. Post-processing of the data obtained in the numerical simulation is done to present the data interactively at the hand of contour plots (visualization of scalar variables such as temperature), vector plots (visualization of the direction and magnitude of the flow) or xy-plots (to determine the profiles of certain variables at certain locations within the flow domain). This section will discuss the temperature separation and mass separation post - processing results separately.

C.4.1 Temperature Separation

The goal of this numerical simulation is to qualitatively compare the numerical results to the analytical results and to see whether the proposed analytical temperature separation mechanisms are valid. To best compare these numerical results to the analytical model it was decided to use xy-plots. The numerical rotational velocity and radial pressure profiles were plotted at five measuring stations that were created as radial "Lines/Rakes" along the z-axis of the computational mesh, as illustrated in Figure C10. The measuring stations are at specific z/L locations 0.1, 0.3, 0.4, 0.5, 0.7 and 0.8 where z is the z-coordinate and L is the length of the flow domain.
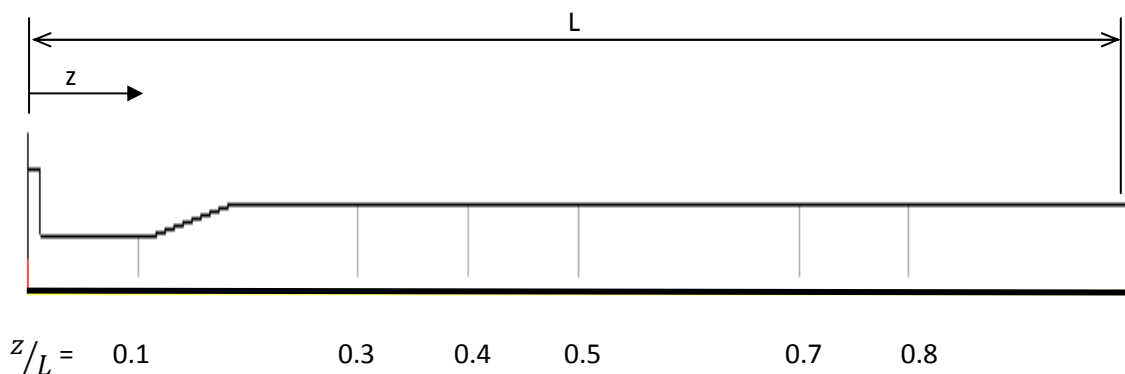
Figure C10: Measurement stations shown on the computational mesh

Firstly the numerical rotational velocity components were plotted along the radius of the computational domain at the various measuring stations together with the

analytically calculated rotational velocity for b = 0.5 in Figure C11. Figure C11 shows that the numerical rotational velocity magnitude decreases along the z-axis of the RHVT and it also shows that the velocity decreases drastically near the wall of the RHVT. In comparison to the analytically calculated rotational velocity profile, it is seen that the magnitude of the rotational velocity at $z/_L$ = 0.1 is similar to the analytical model except near the wall, where the analytical model velocity increases while the numerical model velocity decreases rapidly. This decrease in velocity in the numerical model could be due to very high shear stresses at the wall, which is not modelled accurately in the analytical solution.
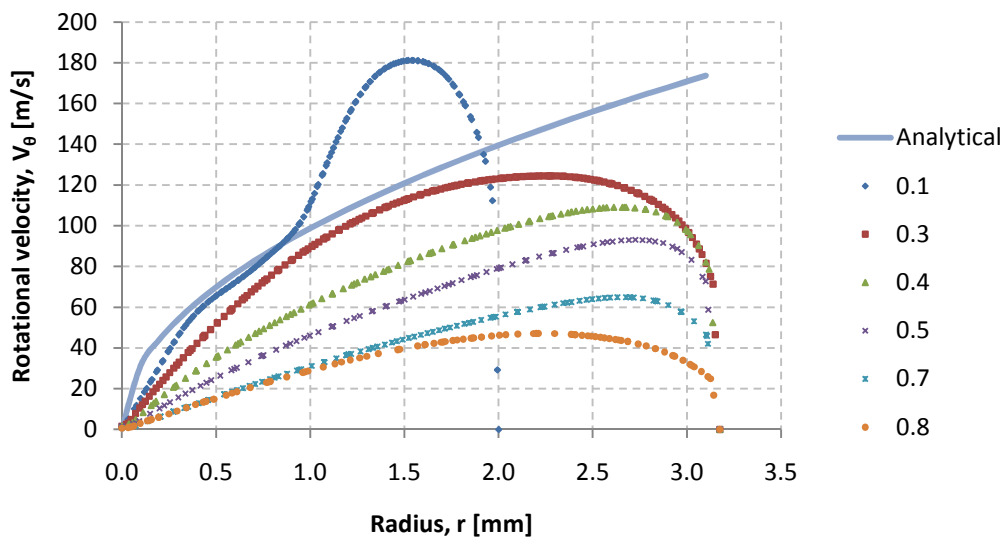
Figure C11: Rotational velocity profiles

The numerically calculated radial pressure profiles are considered next and are shown in Figure C12. The numerical pressure profiles show that the pressure in the RHVT is below atmospheric pressure and thus forms a vacuum. Figure C12 also shows that the pressure at the centre of the flow domain is lower than the pressure at the inner tube wall. Referring to Figure 23 it is seen that the magnitude of the pressure profile, for b = 0.5, is much higher than the numerical solution values. This difference is due to the made assumption that the air in the centre of the RHVT is at atmospheric pressure. From the numerical results it is shown that this assumption in incorrect. The pressure difference between the centre and the wall of the flow domain of the analytical solution is in the

order of 300 kPa whereas the numerical solution shows a pressure difference of only about 17 kPa. Although these values do not correlate, both pressure profiles do show an increase in pressure from the centre to the inner wall of the flow.
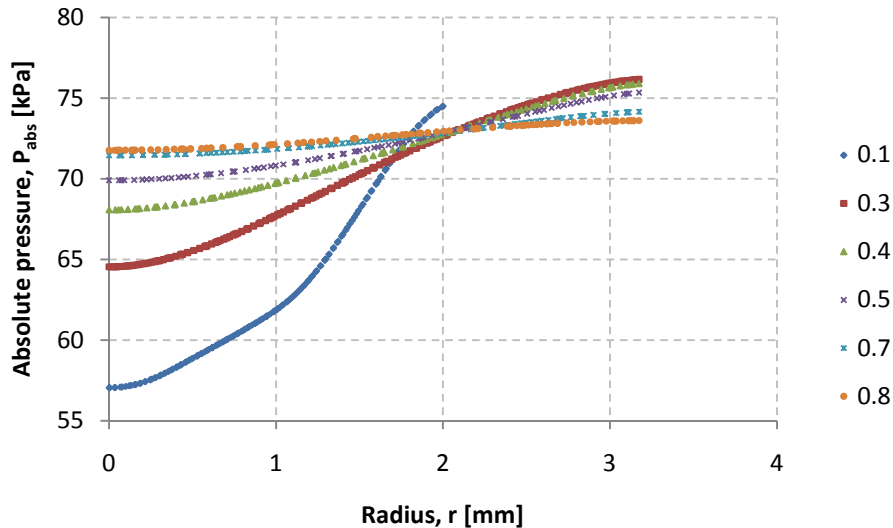
Figure C12: Absolute pressure profiles

To further compare the preliminary numerical results with the analytical results, the three control volumes (as shown in Figure 19) are considered in the CFD computational mesh as shown in Figure C13. Figure C13 is a contour plot showing the contours of static temperature in the computational mesh. Referring to control volume 1 in Figure C13, it is seen that the air temperature exhausting out of the radial inlet slot is at a much lower temperature (143 K) than the inlet air (294 K). This decrease in temperature across the inlet nozzles was also observed in the analytical analysis, although the calculated temperature at the nozzle outlet was at a higher temperature of 245 K. Considering control volume 2, it is shown on Figure C13 that the cold air entering the flow domain from the inlet slot increases drastically in temperature from the nozzle inlet to just before the cold outlet, at which point it decreases again. This temperature profile does not compare to the proposed analytical model for this control volume and it can be presumed that this difference is due to either the analytical model not being able to predict the temperature distribution accurately due to the high turbulence in this flow region, or that the turbulence model chosen for this numerical simulation is inaccurate.

In control volume 3 of Figure C13, it is shown that the air temperature near the wall is much higher than the air temperature in the centre of the flow domain. This temperature distribution together with the decrease in the numerically calculated rotational velocity near the wall shows that heating of the inlet air could possibly occur due to frictional heating near the inner wall of the RHVT as proposed by the analytical model.
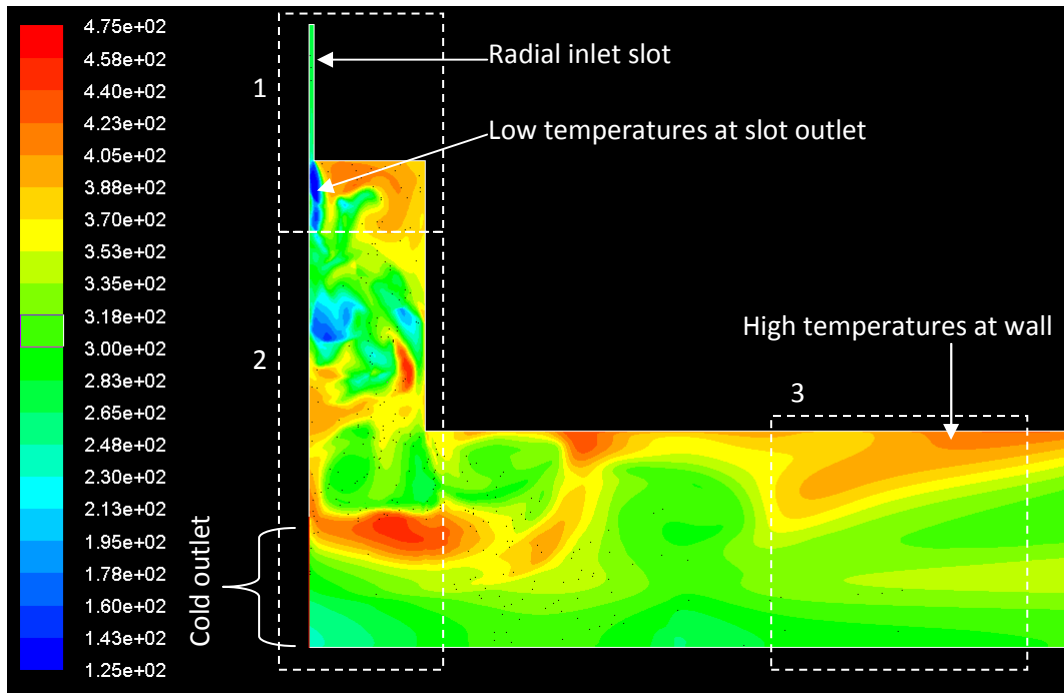
Figure C13: Contours of static temperature [K] shown on the CFD computational mesh showing control volumes 1, 2 and 3 from Figure 18.

Through this comparison of the numerical results to the analytical results, it is confirmed that the inlet air does cool down drastically as it enters the inner tube of the RHVT through the inlet nozzles. It also shows that the shear forces at the wall are large enough to cause a significant decrease in the rotational velocity, and that heating of the inlet air occurs near the wall. It is therefore reasonable to assume that this heating is due to frictional heating. The mechanism of cooling of the inlet air is however not confirmed. Due to the fact that the numerical simulation did not show cooling at the outlet, it does not compare to the experimental and analytical findings and can therefore not be interpreted as accurate. The reason for the numerical simulation's inaccuracy in this

regard can be attributed to the chosen turbulence model or that the numerical solution did not converge. To accurately compare the numerical results of this flow region to the proposed analytical solution, more work will have to be done on the CFD model.

Although some of the analytical results compared to the numerical results, further CFD simulations would have to be done to verify the proposed analytical solutions for the temperature separation mechanism.

C.4.2 Mass Separation

The particle paths of three graphite particles of diameter d_p = 0.5 μm, 0.7 μm and 1 μm were tracked analytically in the r-θ plane of the RHVT flow in section 5.2.2. In the analytical model the particles had an initial position of s_r = 0.00635 mm and an initial rotational velocity of $V_{f,\theta}$ = 78.57 m/s. The graphite particle paths were also numerically simulated (using CFD) by injecting 20 graphite particles at different axial locations into the computational domain at r = 0.000635 mm. The resulting particle paths for graphite particles with diameters 0.5 μm, 0.7 μm and 1 μm are shown in Figure C14.

From Figure C14 it is shown that the particles tend to move radially outwards towards the wall of the RHVT domain and that the particles further along the axial axis tend to move towards the hot outlet whereas the particles closer to the inlet tends to move towards the cold outlet. From Figure C14 it is shown that more particles tend to move towards the hot outlet than the cold outlet, which is consistent with the experimental results. It is also shown that the heavier particles, with larger diameters, tend to move more outward (as seen in Figure C4 (c) than the lighter particles with smaller diameters (see Figure C14(a)), which correlates with the calculated analytical results shown in Figures 32 and 33 in the main text.

(a) d_p = 0.5 μm

(b) d_p = 0.75 μm

(c) d_p = 1 μm
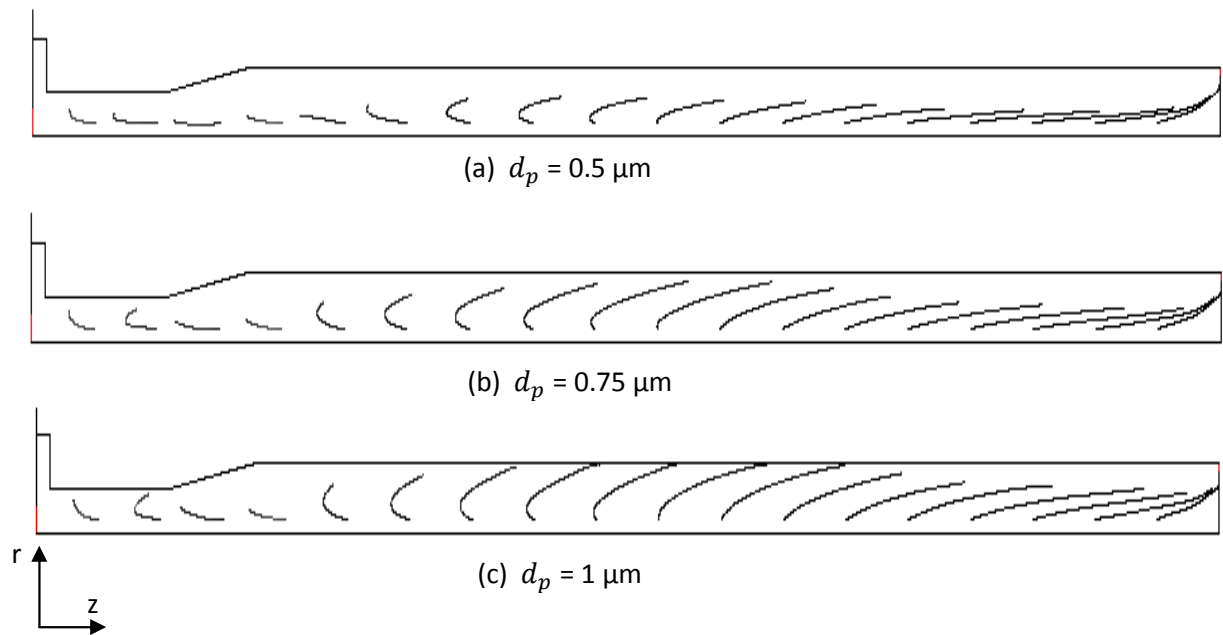
Figure C14: Numerically simulated graphite particle paths for different axial positions along the computational domain with an initial position of r = 0.000635 mm and particle diameters (a) d_p = 0.5 μm , (b) d_p = 0.75 μm and (c) d_p = 1 μm

C.4.3 Further CFD Results

In this section further xy-plots are given for some important parameters such as axial velocity, radial velocity and static temperature. From Figure C16 (a) it is seen that the radial velocity at z/L = 0.1 is much higher in magnitude that at the other measuring station further down the cylindrical tube. Also the radial velocity at z/L = 0.1 is in the positive r-direction whereas the other measuring station velocities are in the negative r-direction. This means that at z/L = 0.1 the air is moving from the centre of the flow to the wall (expanding outwards), whereas the air at the other measurement station moves from the wall towards the centre, although at a very low velocity.

(a)

(b)
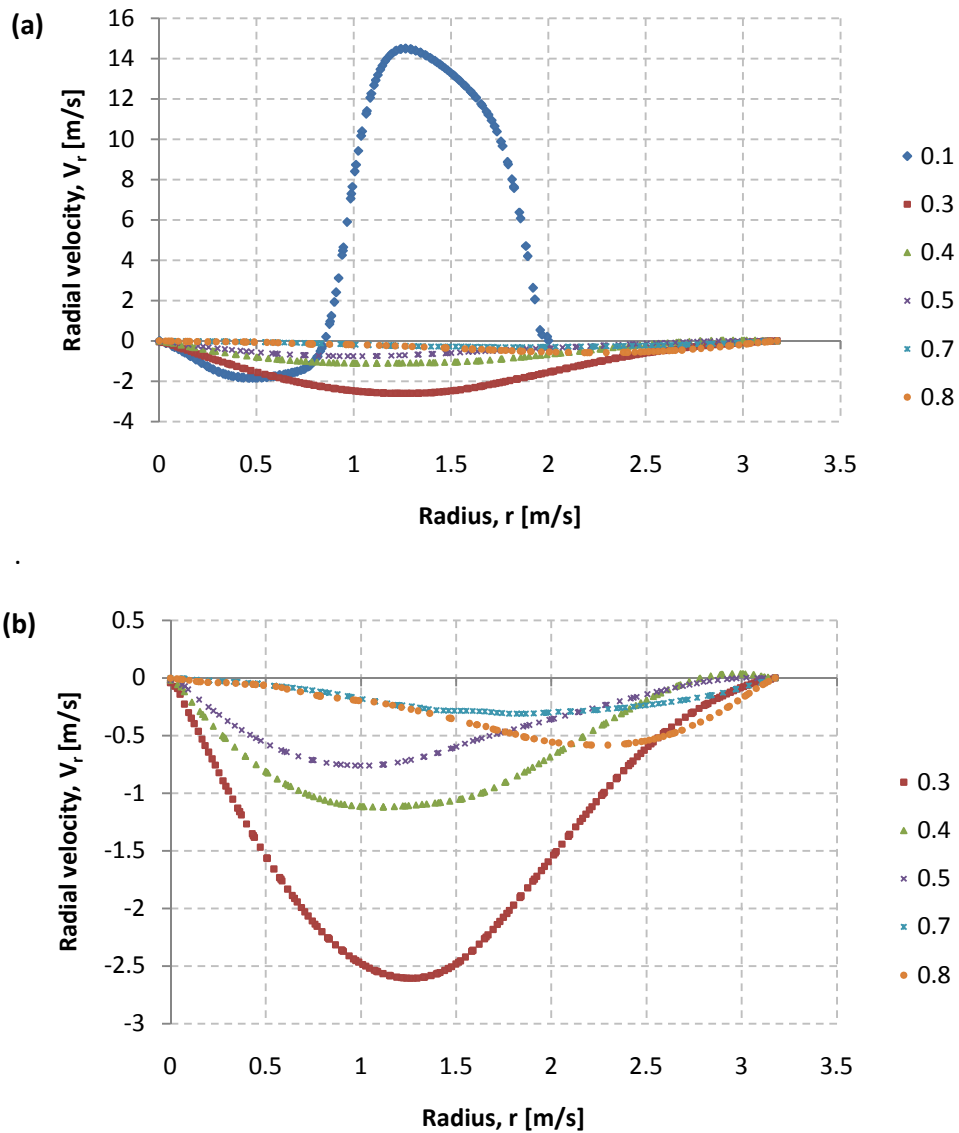
Figure C15: Radial velocity profiles (a) at all measuring stations, (b) at measuring stations

$$^{z}/_{L} = 0.3 - 0.8$$

The axial velocity profiles give an indication of the two vortex streams that exist within the RHVT. The negative axial velocity values indicate the counter vortex stream that flows in the centre of the flow domain from the hot outlet to the cold outlet. From Figure C16 it is shown that the counter stream exists near the cold outlet and that the negative axial velocity decreases as the flow moves further down the flow domain towards the hot outlet. At $^{z}/_{L}$ = 0.7 and 0.8 there is only flow in the positive axial direction which means the there is no counter flow near the hot outlet.
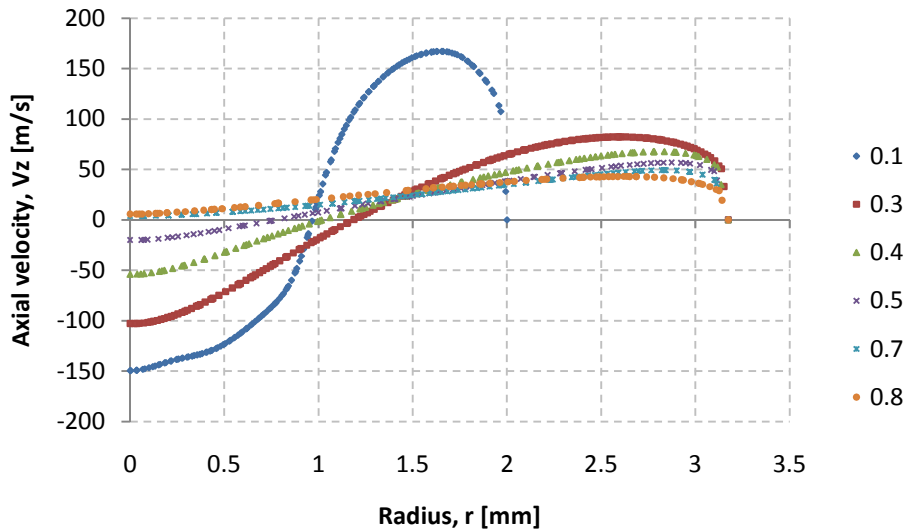
Figure C16: Axial velocity profiles
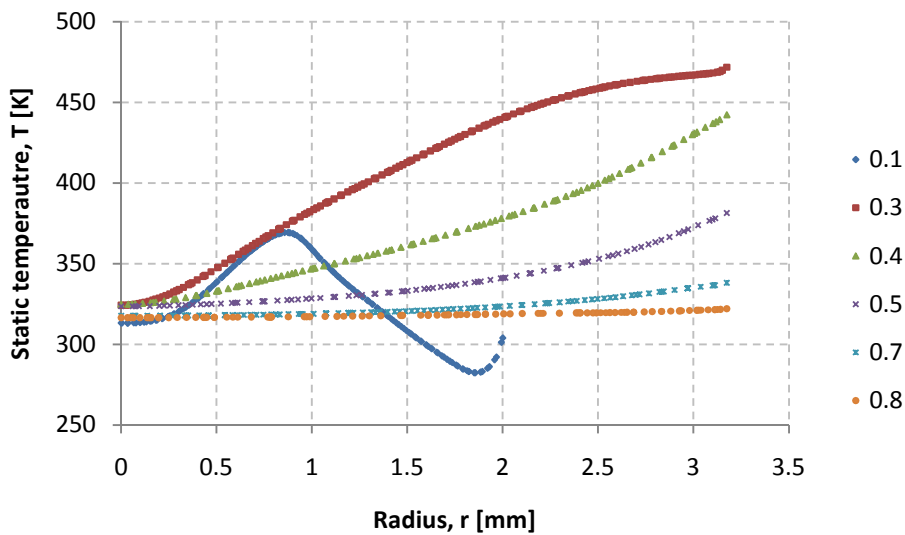
Figure C17: Static temperature profiles

The static temperature profiles in Figure C17 show an increase in temperature along the radius of the RHVT which is consistent with the observed temperature separation phenomenon; however it shows no cooling of the air below the inlet temperature of 294 K. This inconsistency could be due to the fact that the CFD solution did not converge and further modelling might be required to accurately determine the temperature profiles.

APPENDIX D: RHVT VOLUME FRACTION AND TEMPERATURE MEASUREMENT

D.1 Volume Fraction Measurement

The volume fraction is one of the variables (as identified in section 4.1) that can have a significant influence on the dust separation efficiency of the RHVT as well as the temperature separation. It is an independent variable which has to be set to a specific value at the beginning of an experiment. Volume fraction μ_c is defined as the ratio of the cold air (at cold outlet) volumetric flow rate G_c to the inlet volumetric flow rate G_i and can be expressed as follows:

$$\mu_c = \frac{G_c}{G_i} \qquad\qquad\qquad \text{D1}$$

$$\mu_c = f(valve\ position) \qquad\qquad\qquad \text{D2}$$

The volume fraction of the RVHT is set by adjusting the flow control device at the hot outlet. The flow control device is a screw type device that, when turned, either increases or decreases the annular hot outlet area. If the hot outlet annular area increases, more air will flow through the hot outlet and the volume fraction will decrease. When the hot outlet annular area decreases the volume fraction increases. Therefore the volume fraction is a function of the position of the screw type device which is specified as how much the valve was turned from the fully closed position in degrees (equation D2).

To determine the correlation between the volume fraction and the flow control device position, the inlet volumetric flow rate as well as the hot outlet volumetric flow rate was measured for a specific hot valve position using the FESTO flow sensors for air and the orifice flow sensors for helium. The volumetric flow rate of the cold outlet can consequently be calculated by taking the law of mass conservation into account

$$G_c = G_i - G_h$$

The flow control device's position was measured with a 360° protractor attached to the hot end of the RHVT. Measurements were then taken at a certain flow control device angle for different inlet volumetric flow rates for both air and helium. After initial tests were conducted it was determined that the volume fraction for both air and helium are the same for a specified flow control device position. The tests showed that the volume fraction changes only slightly for different inlet volumetric flow rates, but this change was in the order of 0.01 and was thus considered insignificant. The volume fraction could therefore be determined for any volumetric flow rate given a specific flow control device position, as shown in Table D1 for the two Exair® RHVT devices that were tested.

Table D1: Volume fraction for different hot valve position

SMALL RHVT		MEDIUM RHVT	
μ_c	valve position [°]	μ_c	valve position [°]
1	0	1	0
0.842	45	0.92	90
0.732	90	0.895	130
0.672	100	0.858	180
0.561	130	0.818	230
0.484	150	0.777	270
0.36	180	0.709	360
0.284	230	0.54	900
0.159	270	0.529	1440
0.018	360	0.526	1800
-0.93	450	0.505	no valve

A calibration curve was set up to find the relation between the flow control device position and the volume fraction μ_c as shown in Figure D1. The calibration equation for the small RHVT is a 2nd order polynomial trendline with a R^2-value of 0.995 and the

calibration equation of the medium RHVT is a 3rd order polynomial with R^2 = 0.998. These equations are given as equation D4 for the small RHVT and equation D5 for the medium RHVT.
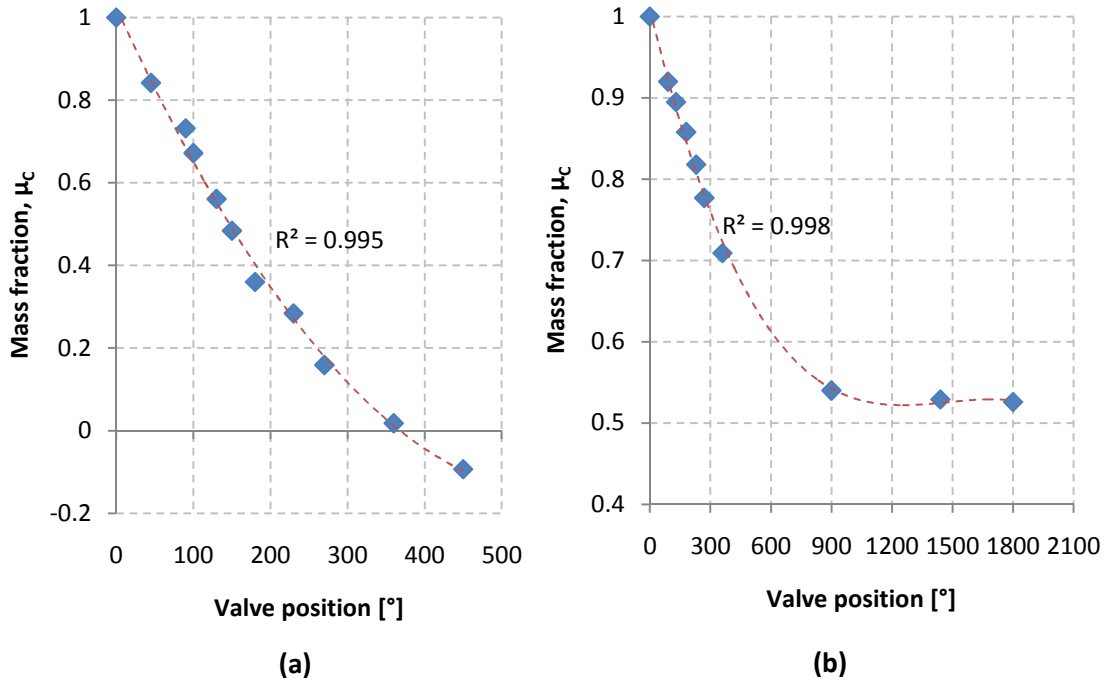
Figure D1: Volume fraction calibration curve a) small Exair® RHVT b) medium Exair® RHVT

$$\mu_C = 3.555 \times 10^{-6} valve\ position^2 - 4.092 \times 10^{-3} valve\ position + 1.0244$$

D4

$$\mu_C = -1.6285 \times 10^{-10} valve\ position^3 + 7.1846 \times 10^{-7} valve\ position^2 - 1.0344 \times 10^{-3} + 1.01$$

D5

D.2 Temperature Measurement

As discussed in Chapter 5, the temperature of both the hot and the cold outlet air is dependent on the volume fraction set by the flow control device of the RHVT. The temperature differences (temperature increase at the hot outlet and temperature decrease at the cold outlet) for certain inlet pressures and different volume fractions are

given by the RHVT manufacturer Exair® in Table D2. These values show the approximate maximum temperature drop (or rise) from inlet air temperature that can be achieved given the inlet pressure and volume fraction for a large RHVT. As can be seen from Table D2, both the temperature drop of the cold outlet air and the temperature rise of the hot outlet air increases with increasing inlet pressure. It is also shown that the temperature drop of the cold outlet air increases as the volume fraction decreases, while the rise in temperature of the hot outlet air decreases and vice versa.

Table D2: Maximum achievable outlet temperature differences due to varying inlet pressures and cold volume fractions (Etest, 2008)

Inlet Pressure	Cold Volume Fraction						
Bar	0.2	0.3	0.4	0.5	0.6	0.7	0.8
4	56.9	54.7	50.9	46.1	40	32.9	25.1
	13.2	21.9	32.4	43.9	57.1	72.5	91.2
5	61.6	59	54.8	49.4	43	35.4	26.9
	13.7	23.3	34.2	46.5	60.9	77.2	97.1
6	65.4	62.7	58.2	52.7	45.6	37.0	28.6
	14.1	24.3	35.8	48.6	63.9	81.0	102.1

Numbers in the shaded area give the temperature drop of cold air in °C
Numbers in the un-shaded area give temperature rise of hot air in °C

Table D2 shows only the maximum achievable temperature differences, therefore it was decided to also measure the temperature differences in both the small and medium Exair® RHVT's under the experimental work inlet conditions with T-type thermocouples. The temperature of the ambient air, inlet air and the air at the hot and cold outlets were measured for different volume fractions. These temperatures were also measured using helium. The inlet pressure and volumetric flow rate were kept constant at 603 kPa and 77 L/min for the small RHVT and at 443 kPa and 280 L/min for the medium RHVT in air and at 311 kPa and 40 L/min for the small RHVT and at 201 kPa and 120 L/min for the medium RHVT in helium. The temperatures were logged using a Schlümberger data

logger (SI 35951C IMP) for a period of 5 minutes per test and the average values of the inlet and outlet temperatures were then calculated from the logged data. Table D3 shows these average measured values as well as the calculated temperature differences between the outlet air/helium and the inlet air/helium for the hot and cold outlets for different volume fractions μ_c and the corresponding flow control device positions in degrees for both the medium and small RHVT.

Table D3 and Table D4 shows that the cold outlet temperature drop increases with a decrease in volume fraction for both helium and air. The rise in temperature at the hot outlet, however, seems to increase to a maximum value at $\mu_c = 0.7$ and then decreases slightly as μ_c nears 1 in air, but not for helium. It is also shown that the decrease in the cold outlet temperature is much greater than the increase in the hot outlet temperature in air, while the opposite is true for helium. The temperature differences for the medium RHVT is also much higher than that of the small RHVT in both air and helium. This could be due to the higher inlet volumetric flow rate of the medium RHVT and not the inlet pressure because the inlet pressure of the medium RHVT is lower than that of the small RHVT.

Table D3: Experimental average measured temperature differences in air

μ_c	μ_c [°]	T_{amb}	T_i	T_h	T_c	$T_{increase}$	$T_{decrease}$
AIR							
Medium RHVT							
0.92	90	18.70	17.09	44.32	4.56	25.62	14.14
0.78	270	16.20	16.01	47.04	-1.26	30.84	17.46
0.54	900	18.70	17.19	23.90	-23.69	5.20	42.39
Small RHVT							
μ_c	μ_c [°]	T_{amb}	T_i	T_h	T_c	$T_{increase}$	$T_{decrease}$
0.84	45	18.70	18.21	27.43	8.08	8.73	10.62
0.73	90	18.60	17.67	37.97	3.89	19.37	14.71
0.36	180	18.70	18.09	25.75	-4.79	7.05	23.49
0.16	270	18.70	18.27	18.71	-3.33	0.01	22.03

Table D4: Experimental average measured temperature differences in helium

HELIUM							
Medium RHVT							
μ_c	μ_c [°]	T_{amb}	T_i	T_h	T_c	$T_{increase}$	$T_{decrease}$
0.92	90	18.8	15.77	59.91	12.35	44.15	3.42
0.78	270	18.8	20.52	59.73	-0.40	39.21	20.92
0.54	900	18.8	18.90	24.07	-15.39	5.17	34.29
Small RHVT							
μ_c	μ_c [°]	T_{amb}	T_i	T_h	T_c	$T_{increase}$	$T_{decrease}$
0.84	45	16.5	16.6	38.2	12.2	21.60	4.40
0.73	90	16.2	16.01	31.58	3.29	15.58	12.72
0.36	180	16.5	16.7	28.2	-5.9	11.50	22.60
0.16	270	16.5	16.8	21.3	-7.4	4.50	24.20

APPENDIX E: EXPERIMENTAL RESULTS AND REGRESSION DATA

The raw data of the experimental measurements are given in Appendix E.1. For each set of experiments the input parameters such as volumetric flow rate G, volume fraction μ_c and duration of the experiment t is given together with the resulting measured mass of the graphite injected m_i and the masses collected in the hot and cold dust collectors. The experimental data that was used in the regression analysis is then given in section E.2.

E.1 Experimental Results

The experimentally measured raw data is shown in Tables E1 to E4. From these measured experimental results the dust separation efficiency was calculated using equation 2 (see Chapter 4). The experimental work was divided into five sets: experiments done with the small RHVT in air, experiments done with the medium RHVT in air, experiments done in helium and experiments done with the finer graphite dust. For each set of experiments, the volume fraction and volumetric flow rate were varied. These raw data sets were then statistically analysed to determine systematic and random errors. For each data set the average $\bar{x}$ was calculated and then the standard deviation σ was calculated to determine the random and systematic errors. The data points with high standard deviations σ (shaded values) were discarded and the final dust separation efficiency was determined by calculating the average of the remaining data points, which is shown at the bottom of the efficiency columns in Tables E1 to E4. The ensuing processed results are thus:

Table E1: Small RHVT experiment results using air

VARYING VOLUME FRACTION										
Test nr	G [L/min]	μ_c	t [min]	m_i [mg]	m_h [mg]	m_c [mg]	η [%]	$\bar{x}$	σ^2	σ
1	77	0.73	45	103.2	84.4	6	93.4		0.933	0.966
2	77	0.73	45	145.3	124.2	14.8	89.4		24.76	4.976
3	77	0.73	45	197.8	160.8	1.7	99.0		21.39	4.625
4	77	0.73	45	114.7	100.2	4.1	96.1		3.029	1.740
5	77	0.73	45	157.7	133.3	12.2	91.6		7.363	2.713
6	77	0.73	45	128.7	100	3.5	96.6		5.243	2.290
Average				141.2	117.2	7.1	94.4	110	10.45	3.233
Test nr	G [L/min]	μ_c	t [min]	m_i [mg]	m_h [mg]	m_c [mg]	η [%]	$\bar{x}$	σ^2	σ
1	77	0.36	45	75.6	128.6	10.4	92.5		0.014	0.118
2	77	0.36	45	103.7	88.9	3.9	95.8		11.54	3.398
3	77	0.36	45	88	73.2	8.1	90.0		5.583	2.363
4	77	0.36	45	122.6	110.2	6.7	94.3		3.492	1.869
5	77	0.36	45	82.4	68.8	8.6	88.9		12.32	3.511
6	77	0.36	45	253.2	186.5	15.8	92.2		0.044	0.210
7	77	0.36	45	240.8	181.3	11.6	94.0		2.518	1.587
8	77	0.36	45	115.5	93.8	8.7	91.5		0.788	0.888
Average				135.2	116.4	9.2	92.4	92.4	4.539	2.130
Test nr	G [L/min]	μ_c	t [min]	m_i [mg]	m_h [mg]	m_c [mg]	η [%]	$\bar{x}$	σ^2	σ
1	77	0.16	45	166.5	137.2	19.7	87.4		4.678	2.163
2	77	0.16	45	108.9	91.7	10.4	89.8		0.043	0.207
3	77	0.16	45	107.00	88.9	9.8	90.1		0.215	0.464
4	77	0.16	45	131.6	113.1	14.4	88.7		0.812	0.901
5	77	0.16	45	165.7	105.8	9.2	92.0		5.727	2.393
Average				135.9	107.3	12.7	89.5	89.6	1.434	1.198

VARYING VOLUME FLOW RATE										
Test nr	G [L/min]	μ_c	t [min]	m_i [mg]	m_h [mg]	m_c [mg]	η [%]	$\bar{x}'$	σ^2	σ
1	64	0.73	45	48.1	35.8	27.7	56.4		739.6	27.20
2	64	0.73	45	251.4	182.5	14.6	92.6		81.33	9.02
3	64	0.73	45	69.10	57.8	9.5	85.9		5.34	2.31
4	64	0.73	45	75.5	57.4	8.1	87.6		16.48	4.06
5	64	0.73	45	33.1	29.4	11.3	72.2		128.5	11.34
6	64	0.73	45	95.2	83.2	14.8	84.9		1.75	1.32
7	64	0.73	45	149.4	101.9	13	88.7		26.13	5.11
8	64	0.73	45	154.3	130.1	18.7	87.4		14.89	3.86
9	64	0.73	45	126.5	88.3	6	93.6		101.2	10.06
10	64	0.73	45	85.7	64.6	10.2	86.4		7.78	2.79
Average				108.8	83.1	13.4	86.4	83.6	112.3	10.60
Test nr	G [L/min]	μ_c	t [min]	m_i [mg]	m_h [mg]	m_c [mg]	η [%]	$\bar{x}$	σ^2	σ
1	90	0.73	45	219.6	195	18.8	91.2		71.91	8.480
2	90	0.73	45	206.5	188.4	6.6	96.6		192.8	13.88
3	90	0.73	45	46	40.5	26.6	60.4		500.3	22.36
Average				157.4	141.3	17.3	93.9	82.7	255.0	15.97

Table E2: Medium RHVT experiment results using air

VARYING VOLUME FRACTION										
Test nr	G [L/min]	μ_c	t [min]	m_i [mg]	m_h [mg]	m_c [mg]	η [%]	$\bar{x}$	σ^2	σ
1	279	0.77	20	722.8	690.4	98.5	87.5		3.58	1.89
2	279	0.77	20	910	870	79.3	91.6		5.02	2.24
3	279	0.77	20	1094	1054.6	155.1	87.2		4.96	2.23
4	279	0.77	20	423.6	344.8	30.4	91.9		6.20	2.49
5	279	0.77	20	725.7	719.4	167.5	81.1		68.77	8.29
6	279	0.77	20	540.9	523.8	15.7	97.1		59.03	7.68
Average				736.2	700.5	91.1	89.6	89.4	24.59	4.96

Test nr	G [L/min]	μ_c	t [min]	m_i [mg]	m_h [mg]	m_c [mg]	η [%]	$\bar{x}$	σ^2	σ
1	279	0.54	20	797.6	780.2	318.4	71.0		291.0	17.0
2	279	0.54	20	690.9	615.2	12	98.1		100.2	10.0
3	279	0.54	20	1009.6	904.9	336.7	72.9		230.8	15.2
4	279	0.54	20	691.4	701.4	51.3	93.2		26.09	5.11
5	279	0.54	20	688.8	641.8	55.5	92.0		15.71	3.96
6	279	0.54	20	628	617.5	38.2	94.2		37.18	6.10
7	279	0.54	20	748.3	740	37.7	95.2		50.06	7.08
Average				750.7	714.4	121.4	93.6	88.1	125.1	11.1
Test nr	G [L/min]	μ_c	t [min]	m_i [mg]	m_h [mg]	m_c [mg]	η [%]	$\bar{x}$	σ^2	σ
1	279	0.92	20	703	673.7	31.1	95.6		0.84	0.91
2	279	0.92	20	416	399.7	16.3	96.1		0.18	0.42
3	279	0.92	20	400.8	383.3	18.4	95.4		1.17	1.08
4	279	0.92	20	611.9	585.5	10.9	98.2		2.79	1.67
5	279	0.92	20	608.3	569.2	16.1	97.2		0.56	0.75
Average				548.0	522.3	20.5	96.5	96.5	9.82	3.13
VARYING VOLUME FLOW RATE										
Test nr	G [L/min]	μ_c	t [min]	m_i [mg]	m_h [mg]	m_c [mg]	η [%]	$\bar{x}$	σ^2	σ
1	251	0.77	20	548.3	544.5	28	95.1		0.57	0.76
2	251	0.77	20	370	370.7	39.5	90.4		15.85	3.98
3	251	0.77	20	349.20	354	26.3	93.1		1.61	1.27
4	251	0.77	20	536.5	573.7	42.2	93.1		1.45	1.20
5	251	0.77	20	420.5	410.4	13.7	96.8		5.84	2.42
6	251	0.77	20	543.3	526.5	14.6	97.3		8.70	2.95
7	251	0.77	20	441	438	24.6	94.7		0.11	0.33
Average				458.4	459.7	27.0	94.0	94.4	3.41	1.85
Test nr	G [L/min]	μ_c	t [min]	m_i [mg]	m_h [mg]	m_c [mg]	η [%]	$\bar{x}$	σ^2	σ
1	307	0.77	20	432.1	435.1	43	91.0		1.66	1.29
2	307	0.77	20	547.1	548.3	35.8	93.9		2.49	1.58
3	307	0.77	20	506.8	511.8	52.1	90.8		2.35	1.53

4	307	0.77	20	534.5	546.2	60.9	90.0		5.40	2.32
5	307	0.77	20	412.3	420.5	31.6	93.0		0.51	0.72
6	307	0.77	20	357.1	346.6	17.7	95.1		8.11	2.85
Average				465.0	468.1	40.2	92.2	92.3	2.05	1.43

Table E3: Helium experiment results using the small RHVT

VARYING VOLUME FRACTION										
Test nr	G [L/min]	μ_c	t [min]	m_i [mg]	m_h [mg]	m_c [mg]	η [%]	$\bar{x}$	σ^2	σ
1	40	0.73	30	2.6	16.4	14.0	53.9		902	30.0
2	40	0.73	30	277.5	173.6	24.2	87.8		14	3.77
3	40	0.73	30	826.6	648.9	65.9	90.8		46	6.79
4	40	0.73	30	185.7	151.8	10.9	93.3		86	9.31
5	40	0.73	30	304.4	194.1	12.0	94.2		103	10.1
Average				319.4	237.0	25.4	91.5	84	192.2	13.8
Test nr	G [L/min]	μ_c	t [min]	m_i [mg]	m_h [mg]	m_c [mg]	η [%]	$\bar{x}$	σ^2	σ
1	40	0.36	30	41.6	24.7	1.9	92.9		78.55	8.86
2	40	0.36	30	188.0	161.1	9.7	94.3		106.6	10.3
3	40	0.36	30	111.2	72.3	5.9	92.5		71.59	8.46
4	40	0.36	30	299.1	243.9	20.1	92.4		70.43	8.39
5	40	0.36	30	432.1	366.8	33.9	91.5		56.93	7.55
Average				214.4	173.8	14.3	92.3	93	64.02	8.00

Table E4: Fine graphite dust experiment results

FINE DUST HELIUM										
Test nr	G [L/min]	μ_c	t [min]	m_i [mg]	m_h [mg]	m_c [mg]	η [%]	$\bar{x}$	σ^2	σ
1	40	0.73	30	123.1	76.9	13.8	84.8		0.12	0.35
2	40	0.73	30	80.1	69	14.6	82.5		6.76	2.60
3	40	0.73	30	114	88.7	12.8	87.4		5.08	2.25
4	40	0.73	30	86.5	62.4	10.3	85.8		0.49	0.70
Average				100.9	74.3	12.9	85.1	85	2.07	1.44

FINE DUST AIR SMALL										
Test nr	G [L/min]	μ_c	t [min]	m_i [mg]	m_h [mg]	m_c [mg]	η [%]	$\bar{x}$	σ^2	σ
1	77	0.73	40	294.3	275.1	30.1	90.1		25.02	5.00
2	77	0.73	40	267.3	243.5	14.4	94.4		86.13	9.28
3	77	0.73	40	110	108	36.3	74.8		105.9	10.2
4	77	0.73	40	133.1	126.9	11	92.0		47.44	6.89
5	77	0.73	40	121.7	102.6	18.9	84.4		0.48	0.69
Average				185.3	171.2	22.1	88.9	87	44.16	6.65
FINE DUST AIR MEDIUM										
Test nr	G [L/min]	μ_c	t [min]	m_i [mg]	m_h [mg]	m_c [mg]	η [%]	$\bar{x}$	σ^2	σ
1	280	0.78	20	454.8	433.4	3.8	99.1		11.41	3.38
2	280	0.78	20	322.1	294.8	4.2	98.6		8.08	2.84
3	280	0.78	20	561.6	539.5	19.7	96.5		0.53	0.72
4	280	0.78	20	391.5	384.5	35.3	91.6		17.31	4.16
5	280	0.78	20	588.8	561.8	42.5	93.0		7.76	2.79
Average				463.8	442.8	21.1	96.0	96	7.52	2.74

E.2 Regression Data

Table E5 shows the data points used for the regression analysis. This table shows the independent variables values as well as the dust separation efficiency for each set of independent variables. The results and interpretation of these results is given in section 4.4.

Table E5: Regression data

Efficiency	Volume flow rate	Volume fraction	Material	Geometry	Dust grade
y	**x1**	**x2**	**x3**	**x4**	**x5**
93.4	77	0.73	0.286	1.33E-01	6.00E-06
96.1	77	0.73	0.286	1.33E-01	6.00E-06
91.6	77	0.73	0.286	1.33E-01	6.00E-06
96.6	77	0.73	0.286	1.33E-01	6.00E-06
92.5	77	0.36	0.286	1.33E-01	6.00E-06
90	77	0.36	0.286	1.33E-01	6.00E-06
94.3	77	0.36	0.286	1.33E-01	6.00E-06
92.2	77	0.36	0.286	1.33E-01	6.00E-06
94	77	0.36	0.286	1.33E-01	6.00E-06
91.5	77	0.36	0.286	1.33E-01	6.00E-06
89.8	77	0.16	0.286	1.33E-01	6.00E-06
90.1	77	0.16	0.286	1.33E-01	6.00E-06
88.7	77	0.16	0.286	1.33E-01	6.00E-06
85.9	64	0.73	0.286	1.33E-01	6.00E-06
87.6	64	0.73	0.286	1.33E-01	6.00E-06
84.9	64	0.73	0.286	1.33E-01	6.00E-06
87.4	64	0.73	0.286	1.33E-01	6.00E-06
86.4	64	0.73	0.286	1.33E-01	6.00E-06
91.2	90	0.73	0.286	1.33E-01	6.00E-06
96.6	90	0.73	0.286	1.33E-01	6.00E-06
87.5	280	0.78	0.286	1.63E-01	6.00E-06
91.6	280	0.78	0.286	1.63E-01	6.00E-06
87.2	280	0.78	0.286	1.63E-01	6.00E-06
91.9	280	0.78	0.286	1.63E-01	6.00E-06
93.2	280	0.54	0.286	1.63E-01	6.00E-06
92	280	0.54	0.286	1.63E-01	6.00E-06
94.2	280	0.54	0.286	1.63E-01	6.00E-06
95.2	280	0.54	0.286	1.63E-01	6.00E-06
95.6	280	0.92	0.286	1.63E-01	6.00E-06

96.1	280	0.92	0.286	1.63E-01	6.00E-06
95.4	280	0.92	0.286	1.63E-01	6.00E-06
97.2	280	0.92	0.286	1.63E-01	6.00E-06
91	290	0.78	0.286	1.63E-01	6.00E-06
93.9	290	0.78	0.286	1.63E-01	6.00E-06
90.8	290	0.78	0.286	1.63E-01	6.00E-06
93	290	0.78	0.286	1.63E-01	6.00E-06
95.1	250	0.78	0.286	1.63E-01	6.00E-06
93.1	250	0.78	0.286	1.63E-01	6.00E-06
93.1	250	0.78	0.286	1.63E-01	6.00E-06
94.7	250	0.78	0.286	1.33E-01	6.00E-06
87.8	40	0.73	0.403	1.33E-01	6.00E-06
90.8	40	0.73	0.403	1.33E-01	6.00E-06
93.3	40	0.73	0.403	1.33E-01	6.00E-06
94.2	40	0.73	0.403	1.33E-01	6.00E-06
92.9	40	0.36	0.403	1.33E-01	6.00E-06
92.5	40	0.36	0.403	1.33E-01	6.00E-06
92.4	40	0.36	0.403	1.33E-01	6.00E-06
91.5	40	0.36	0.403	1.33E-01	6.00E-06
84.8	40	0.73	0.403	1.33E-01	1.50E-06
82.5	40	0.73	0.403	1.33E-01	1.50E-06
87.4	40	0.73	0.403	1.33E-01	1.50E-06
85.8	40	0.73	0.403	1.33E-01	1.50E-06
90.1	77	0.73	0.286	1.33E-01	1.50E-06
92	77	0.73	0.286	1.33E-01	1.50E-06
84.4	77	0.73	0.286	1.33E-01	1.50E-06
98.6	280	0.78	0.286	1.63E-01	1.50E-06
96.5	280	0.78	0.286	1.63E-01	1.50E-06
93	280	0.78	0.286	1.63E-01	1.50E-06